



PONTIFICIA UNIVERSIDAD CATOLICA DE CHILE
SCHOOL OF ENGINEERING

**STRUCTURAL AND FUNCTIONAL CHARACTERIZATION
AND ENGINEERING OF ANTARCTIC ENZYMES AS
POTENTIAL BIOCATALYSTS FOR POLYETHYLENE
TEREPHTHALATE (PET) DEGRADATION**

PAULA BLÁZQUEZ SÁNCHEZ

Thesis submitted to the Office of Graduate Studies in partial fulfillment of the
requirements for the Degree of Doctor in Engineering Sciences

Advisor:

CÉSAR ANTONIO RAMÍREZ SARMIENTO

Santiago de Chile, January 2023

© 2022, Paula Blázquez Sánchez



PONTIFICIA UNIVERSIDAD CATOLICA DE CHILE
SCHOOL OF ENGINEERING

**STRUCTURAL AND FUNCTIONAL CHARACTERIZATION
AND ENGINEERING OF ANTARCTIC ENZYMES AS
POTENTIAL BIOCATALYSTS FOR POLYETHYLENE
TEREPHTHALATE (PET) DEGRADATION**

PAULA BLÁZQUEZ SÁNCHEZ

Members of the Committee:

CÉSAR RAMÍREZ

Cesar Ramirez

LORETO VALENZUELA

Loreto Valenzuela

EDUARDO AGOSIN

Eduardo Agosin

RICARDO CABRERA

Ricardo Cabrera

WOLFGANG ZIMMERMANN

Wolfgang Zimmermann

GUSTAVO LAGOS

Gustavo Lagos

Thesis submitted to the Office of Graduate Studies in partial fulfillment of
the requirements for the Degree of Doctor in Engineering Sciences.

Santiago de Chile, January 2023

To my parents, Carlos and Lola.

Resumen

El tereftalato de polietileno (PET) se ha convertido en uno de los principales residuos plásticos producidos a nivel mundial. En los últimos años se han descubierto microorganismos que poseen enzimas capaces de degradar el PET amorfo. La mayoría de estas enzimas son termófilas y presentan actividades óptimas de reacción entre los 60 °C y 70 °C, cerca de la temperatura de transición vítrea del PET. Posteriormente se descubrió una hidrolasa de poliéster en la bacteria mesófila *Ideonella sakaiensis* capaz de hidrolizar parcialmente el PET a 40 °C.

En este trabajo, demostramos que hidrolasas de poliéster de las bacterias antárticas *Moraxella* sp. cepa TA144 (Mors1) y *Oleispira antarctica* cepa RB-8 (OaCut), descubiertas por técnicas bioinformáticas, hidrolizan el poliéster alifático policaprolactona y el poliéster aromático PET a una temperatura de 25 °C. Mors1 produce una reducción de peso de láminas de PET en el rango de las hidrolasas descritas previamente, constituyéndose así como la primera hidrolasa de PET psicrófila. El modelo estructural de Mors1 muestra que la composición de aminoácidos en el centro activo es similar al de sus homólogas termófilas y mesófilas. Además, el análisis metagenómico de muestras antárticas demostró que miembros de la familia Moraxellaceae portan genes que codifican otras potenciales hidrolasas de PET psicrófilas. Para mejorar la actividad de Mors1, se sustituyó un bucle altamente flexible del centro activo por el bucle equivalente de la enzima termófila LCC, lo que dio como resultado un aumento de 20 °C en la temperatura óptima de la actividad, así como un aumento de la actividad hidrolítica de PET de 4.8 veces. Simulaciones de dinámica molecular mostraron una ligera reducción en la flexibilidad en el centro activo de la enzima mutante, lo que sugiere que la actividad a temperaturas más altas se debe a una estabilización local del sitio activo. Estos resultados describen las primeras enzimas degradadoras de PET caracterizadas en organismos adaptados al frío y dan ideas sobre la relación entre la flexibilidad estructural, temperatura y actividad hidrolítica de PET de estas enzimas.

Abstract

Polyethylene terephthalate (PET) has become one of the main plastic wastes produced worldwide. In recent years, several microorganisms have been described to possess enzymes that hydrolyze amorphous PET. Most of these enzymes are thermophilic and exhibit optimal activity at reaction temperatures between 60 °C and 70 °C, near the glass transition temperature of PET. However, later, a polyester hydrolase from the mesophilic bacterium *Ideonella sakaiensis* has been shown to partially hydrolyze PET at 40 °C.

In this work, we demonstrate that bioinformatically discovered polyester hydrolases from the Antarctic bacteria *Moraxella* sp. strain TA144 (Mors1) and *Oleispira antarctica* strain RB-8 (OaCut) hydrolyze the aliphatic polyester polycaprolactone as well as the aromatic polyester PET at 25 °C. Mors1 produces a reduction in PET film weight in the range of previously described hydrolases, thus constituting the first psychrophilic PET-degrading enzyme. Comparative modeling of Mors1 showed that the amino acid composition of its active site resembled both thermophilic and mesophilic PET hydrolases. In addition, bioinformatic analysis of Antarctic metagenomic samples demonstrates that members of the Moraxellaceae family carry candidate genes encoding other putative psychrophilic PET hydrolases.

To enhance the activity of Mors1, we replaced a highly flexible loop in its active center with the equivalent loop of the thermophilic enzyme LCC, resulting in an increase of 20 °C in the optimum temperature of activity of Mors1, as well as an increase of 4.8-fold in PET hydrolysis. Molecular dynamics simulations showed slightly reduced flexibility in the active center of the mutant enzyme, suggesting that the activity at higher temperatures is due to a local stabilization of the active site. These findings describe the first PET-degrading enzymes from cold-adapted organisms and provide insight into the relationship between structural flexibility, temperature, and PET hydrolytic activity in these enzymes.

Keywords: Polyethylene terephthalate (PET) | polyester hydrolases | plastic biodegradation | *Oleispira antarctica* | *Moraxella* sp. | Antarctica | psychrophilic enzymes

Acknowledgments

I would like to thank all the people who have accompanied me during these last years, have made the difficult road easier, and who have made me feel at home despite being thousands of kilometers away. Thank you from the bottom of my heart.

I would first like to thank my supervisor, César, for giving me the opportunity to embark on this exciting project that we started from scratch in 2017, which has taken shape and evolved over the years. Although it has not been easy and there have been moments of frustration, I think we have achieved nearly everything we set out to do. Thank you for your extraordinary scientific advice, from which I have learned so much over the years.

I would also like to thank my colleagues in Chile, especially Felipe, who became a dear friend. His patience, his willingness, and his mentorship in everything related to computational biology was invaluable. Thanks also to Pablo, Maira and the rest of the PB³ members, from whom I have learned everything related to protein production, engineering, and molecular biology, for sharing their scientific knowledge, and for always being there to help. Thanks to the members of the IIBM, particularly Daniela, for her support from the beginning and for her friendship, as well as my colleagues Andrea, Fran and Rocío. A special mention also goes to Dr. Andreas Schüller from the Department of Biological Sciences, in whose group of Molecular Design I learned molecular phylogenetics and docking techniques, which were enormously useful for my research. Thank you, it was a pleasure to be your student.

In 2018 I had the opportunity to travel to the United States for a two-month internship at Ohio State University in Dr. Marcos Sotomayor's lab, working on the crystallization of the Antarctic enzyme *OaCut*. It was an exceptional scientific experience where I learned crystallographic techniques and had the opportunity to remotely use the Advanced Photon Source from the Argonne National Laboratory. Thanks to Dr. Sotomayor for sharing so much of his time, for teaching me, and for always being willing to help

me. Special thanks to Dr. Pedro de la Torre who helped me tirelessly during all that time, searching for crystallization conditions for an enzyme that resisted crystallization. Also, for reassuring me during stressful moments, and welcoming me with a smile every day. Thank you *parce*.

In 2019, I also had the chance to do another research stay at the University of Leipzig, in the laboratory of Dr. Wolfgang Zimmermann, a reference in the field of PET degradation with enzymes. Thanks to this, I learnt all the techniques related to PET and other plastics degradation and was eventually able to specialize in this topic – sharing the laboratory with the authors of the papers I read. This experience undoubtedly marked a before and after in my scientific career. Thanks as well to Dr. Christian Sonnendecker, one of the best colleagues and supervisors anyone could have. Not only an excellent scientific mind, but also a wonderful person. Finally, thanks also to Dr. Jörg Matysik, for making it possible to return to Leipzig to continue the work in his laboratory.

Outside the scientific world, I must thank all the people who have constantly been there for me, whether in person or on the other end of the phone, both in times of joy and sorrow. Thanks to my chosen family: Tina, Ra, Meg, Julia, Divi and all the rest of the group. My long-time friends, with whom I have grown and evolved together. Maturing together. It has become the longest relationship of my life. *La Tierruca, mi casa*, where I have been able to return whenever I needed to. A special mention to Andy who has visited me in almost every place I have lived, even at the end of the world. Also, to the *bilbaínos*, Carmen, Txan and all the others, with whom I shared one of the happiest times of my life.

Thank you to all the people I have met along the way; it has been many years, many countries, and many cities. I still have not had time to process it all. Thanks to Joaquín, my soul brother. For the overflowing love and affection, for being my home in Chile. Meeting you has been the most special thing that has happened to me in these years. Thanks to Santa Mónica, to that house where we shared all those moments. Thanks to Lars, to Leo, to Eze... to that wooden table in the kitchen where we shared so many beers. To Jaquie, the soul of that house that has stayed with us forever. Thanks to Clement, Andréa and Francis, my

first friends in Chile. And thanks to Javier and those memories of Valparaíso that made me come back. I also cannot forget Violette and Dug, who welcomed me in Ohio as soon as I arrived, included me in all their plans and took me on trips. It was really what I needed at that time.

And then Leipzig... what can I say? This wonderful city that I came to by chance and now feels like home. Maddalen, my mathematical physicist, who explained the laws of the universe to me over so many breakfasts. My great friend and family – it hurts me to see you go but I know you will never leave. Thanks also to the Vermut Club, for all the support, for all those meals at Mensa. Finally, thanks to my most recent friends, Fabi and Verena, two of the most incredible people I have been lucky enough to meet. My *bamboleo* housemates who have started to become a family. Thank you for welcoming me in this way, it has been better than I could have ever imagined.

I would be remiss if I did not acknowledge my family, the Blázquez's and the Sánchez's, my aunts, my uncles, and my cousins, for their love and support. A special hug to my uncle Jorge, the person who has been most interested in my scientific work – for downloading my articles and translating them, for the time we have spent talking about science and deep down, for making me feel so valuable. To my aunt Marisa, simply for making me feel so loved. And of course, to my grandmother, whom I never forget, who always told me to go back to live in Spain, closer, closer. All this is also for you, *Yaya*.

Most importantly, a heartfelt thank you to the people to whom I dedicate this thesis: my mother, and my father. For their unconditional love, so unconditional, that I have believed myself capable of anything. For giving me wings, but more importantly, for giving me roots.

And lastly, thanks to all the women who preceded me, who paved the way, who never stayed silent, who made it possible for women to have a place in science and other fields that did not belong to us. It is an honor to continue the journey.

Thank you. *Danke. Gracias.*

Funding bodies

Several institutions have provided financial support to carry out this research: Firstly, the Chilean National Agency of Research and Development (ANID) (Doctoral Grant 21191979). Secondly, Pontificia Universidad Católica de Chile (PUC) with the grant “Ayudante Becario”. In third place, the Chilean Antarctic Institute (INACH) with the Regular Grant RG_47_16, INACH and Doctoral Grant DG_11_18, and the International Cooperation Program ANID-FAPESP 2019/13259-9 between ANID and São Paulo Research Foundation (FAPESP). The two internships abroad in USA and Germany were funded by PUC and ANID respectively. Finally, this thesis was partially supported by the supercomputing infrastructure of the NLHPC (ECM-02).

List of abbreviations

ABD-F	7-fluoro-2,1,3-benzoxadiazole-4-sulfonamide
BHET	bis (hydroxy- ethyl) terephthalate
BSA	Bovine serum albumin
Ce	Enzyme concentration
CM	Chimeric Mors1
CTAB	Cetyltrimethylammoniumbromid
DB	Disulfide bridge
DMT	Dimethyl terephthalate
<i>E. coli</i>	<i>Escherichia coli</i>
EG	Ethylene glycol
EMT	1,2- ethylene-mono-terephthalate-mono(2-hydroxyethyl terephthalate)
ES	Enzyme-substrate complex
FADS	Fluorescence activated droplet sorting in microfluidics
FDBz	Fluorescein dibenzoate
GHG	Greenhouse gases
HD	delta hydrogen
HDPE	High-density polyethylene
HEMT	1-(2- hydroxyethyl) 4-methyl terephthalate
HEPES	4-(2-hydroxyethyl)-1-piperazineethanesulfonic acid
HG	Gamma hydrogen

HOTH	Hydroxylphthalic acid
HPLC	High performing liquid chromatography
IPTG	Isopropyl β -D-1-thiogalactopyranoside
LDPE	Low density polyethylene
MD	Molecular dynamics
MES	2-(N-morpholino) ethanesulfonic acid
MHET	Mono(2-hydroxyethyl) terephthalate
MPD	2-Methyl-2,4-pentanediol
MSA	Multiple sequence alignment
MT	Million tons
NanoDSF	Nano differential scanning fluorimetry
NE	Epsilon nitrogen
NSP	No signal peptide
OD	Delta oxygen
PBAT	Poly (butylene adipate co-terephthalate)
PCL	Poly- ϵ -caprolactone
PCR	Polymerase chain reaction
PcW-PET	Pulverized commercial PET
PE	Polyethylene
PEA	Poly(ethylene adipate)
PEG	Poly(ethylene glycol)
PEG 500 MME	Poly(ethylene glycol) methyl ether 500
PET	Polyethylene terephthalate

PHAs	Polyhydroxyalkanoate
PHB	Poly(β -hydroxybutyrate)
PLA	Poly(lactic acid)
PP	Polypropylene
PS	Polystyrene
PUR	Polyurethane
PVC	Poly(vinyl chloride)
REU	Rosetta Energy Units
RMSD	Root mean-square deviation
RMSF	Root mean-square fluctuation
SDS-PAGE	Sodium dodecyl sulfate -polyacrylamide gel electrophoresis
T ₅₀	Thermal inactivation temperature
T _g	Glass transition temperature
T _m	Melting temperature
TMA	Trimesic acid
TPA	Terephthalic acid
TRIS	Tris(hydroxymethyl) aminomethane
WT	Wild type

List of publications

This thesis contains original research in Chapters II and III.

Chapter II and III.I are adapted from the following article:

Blázquez-Sánchez P, Engelberger F, Cifuentes-Anticevic J, Sonnendecker C, Griñén A, Reyes J, Díez B, Guixé V, Richter PK, Zimmermann W, Ramírez-Sarmiento CA (2021) Antarctic polyester hydrolases degrade aliphatic and aromatic polyesters at moderate temperatures. *Appl Environ Microbiol* 1–36 . <https://doi.org/10.1128/aem.01842-21>

Chapter II and III.III are adapted from the following article:

Sonnendecker C, Oeser J, Richter PK, Hille P, Zhao Z, Fischer C, Lippold H, **Blázquez-Sánchez P**, Engelberger F, Ramírez-Sarmiento CA, Oeser T, Lihanova Y, Frank R, Jahnke H-G, Billig S, Abel B, Sträter N, Matysik J, Zimmermann W (2021) Low Carbon Footprint Recycling of Post-Consumer PET Plastic with a Metagenomic Polyester Hydrolase. *ChemSusChem* 1–11. <https://doi.org/10.1002/cssc.202101062>

During the development of this thesis, an additional article outside its scope was also published:

Matute T, Nuñez I, Rivera M, Reyes J, **Blázquez-Sánchez P**, Arce A, Brown AJ, Gandini C, Molloy J, Ramírez-Sarmiento CA, Federici F (2021) Homebrew reagents for low-cost RT-LAMP. *J Biomol Tech* 32:114–120. <https://doi.org/10.7171/jbt.21-3203-006>

This article is a result of the prioritization of the laboratory in which this thesis was developed to contribute to the combat of the COVID-19 pandemic.

Table of contents

Resumen.....	i
Abstract.....	ii
Acknowledgments.....	iii
Funding bodies.....	vi
List of abbreviations	vii
List of publications	x
List of Figures.....	xv
List of Tables	xviii

CHAPTER I. THEORETICAL FRAMEWORK

Introduction.....	1
▪ Polymers	1
▪ Production, usage, and impact of synthetic polymers.....	5
▪ PET production and recycling	12
▪ Biocatalysis as a solution to plastic pollution	15
▪ Discovering PET-degrading enzymes.....	17
▪ Characterization and engineering of PET hydrolases	21
▪ Classification of PET-degrading enzymes.....	30
▪ Methods for measuring enzymatic PET hydrolase activity	31
▪ Cold-adapted enzymes as potential PET biocatalysts.....	33
▪ Experimental and computational methods to assess the structural flexibility of cold-adapted enzymes.	38

▪ Experimental and computational methods to assess the interactions between an enzyme and its substrate.....	40
Hypothesis and objectives.....	45
▪ Hypothesis	46
▪ General objective	46
▪ Specific objectives	46
 CHAPTER II. METHODOLOGY	
▪ Bioinformatic identification of OaCut and Mors1	47
▪ Protein expression and purification.....	47
▪ Cloning and mutagenesis	48
▪ Sodium dodecyl sulfate -polyacrylamide gel electrophoresis (SDS-PAGE)	49
▪ Thermal stability of OaCut and Mors1	49
▪ X-ray Crystallography	50
▪ PCL nanoparticle suspension preparation.....	50
▪ PCL plate clearing assays	50
▪ Determination of optimum reaction temperature and buffer conditions for PCL hydrolysis by Mors1	51
▪ Kinetic model for polymer nanoparticle hydrolysis and determination of the kinetic constants of Mors1	52
▪ Turbidimetric quantification of PCL hydrolysis activity of Mors1 variants.....	56
▪ PCL degradation with crude extract.....	56
▪ MHET inhibition assay	57
▪ Hydrolysis of amorphous PET films by Mors1, OaCut, and <i>IsPETase</i>	57
▪ Scanning electron microscopy of PET films.....	58
▪ Fluorescent dye labeling of free cysteines in Mors1	58

- Comparative modelling of Mors1 58
- Molecular dynamics simulations 60
- Identification of potential PET hydrolases in Antarctic coastal metagenomes..... 62
- Abundance and taxonomic affiliation of potential metagenomic PET hydrolases 62
- Molecular docking 63

CHAPTER III. RESULTS

- III.I Structural and functional characterization of Antarctic hydrolases OaCut and Mors1 64
 - Mors1 and OaCut can be expressed in *E. coli* in a non-soluble form..... 64
 - Mors1 and OaCut degrade PCL at moderate temperatures..... 65
 - Crystallographic structures of Mors1 and OaCut were not obtained..... 67
 - Mors1 presents higher hydrolysis rates with phosphate buffers and high salt concentrations 67
 - Kinetic parameters of PCL hydrolysis by Mors1 are similar to *IsPETase*..... 69
 - Mors1 hydrolyzes amorphous PET films at moderate temperatures 70
 - Mors1 is not inhibited by MHET..... 72
 - The active site of Mors1 presents features from mesophilic and thermophilic PET-hydrolyzing cutinases..... 73
 - Flexibility as a hallmark of temperature adaptation..... 76
 - Identification of polyester hydrolases from Antarctic marine environments..... 77
- III.II Improvement of the hydrolytic activity of Mors1 via protein engineering 80
 - Single point variants of Mors1 did not improve hydrolytic activity 80
 - Thermostability of single-point variants remains unchanged 83
 - Chimeric Mors1 has an improved PET hydrolytic activity 85
 - PCL degradation with crude extract..... 88
 - MD simulations of the loop swapping variant 90

III.III Characterization of the thermophilic PHL7 enzyme binding residues	92
CHAPTER IV. DISSCUSION AND CONCLUSIONS	
▪ Discussion.....	96
▪ Conclusions.....	106
References.....	109
Supplementary figures	124
Supplementary tables	133

List of Figures

Figure 1. Polymer structure.....	3
Figure 2. Global plastic production and waste per year.....	6
Figure 3. Fate of plastics produced from 1950 to 2015	7
Figure 4. Interactions between plastic and climate	10
Figure 5. Contribution to net GHG emissions by different strategies in plastic production and waste management	12
Figure 6. Chemical structure of the most common used synthetic plastics.	13
Figure 7. Synthesis reactions for PET.....	14
Figure 8. Products obtained from PET hydrolysis by polyester hydrolases.	18
Figure 9. Structure and active site of an α/β hydrolase.....	19
Figure 10. Catalytic mechanism of α/β hydrolases.....	20
Figure 11. PET degradation assays by PHL7 and LCC.....	23
Figure 12. Active site of <i>IsPETase</i> in apo-form with the three different conformations of W185	25
Figure 13. Active site of <i>IsPETase</i> and <i>IsPETase</i> ^{R280A} in complex with 2-HE(MHET) ₄	26
Figure 14. Enzymatic depolymerization of PET by <i>IsPETase</i> , LCC and their variants	28
Figure 15. Structures of WT <i>IsPETase</i> and FAST-PETase	29
Figure 16. The addition of anionic surfactants to the PET surface increases the absorption of <i>IsPETase</i> to the PET film.....	30
Figure 17. Key residues involving in PET catalysis and classification of enzymes based on their aminoacidic composition	31
Figure 18. Diagram of energy for the enzymatic catalysis from substrates (S) to products (P) according to the transition state theory	36

Figure 19. Temperatures of activity and unfolding of mesophilic and psychrophilic enzymes.....	37
Figure 20. Hydrolysis rate of a polymer film as a function of the enzyme concentration	54
Figure 21. SDS-PAGE of recombinant truncated OaCut (27.8 kDa), <i>IsPETase</i> (28.6 kDa) and Mors1 (28.6 kDa) after purification by affinity and size exclusion chromatography	65
Figure 22. Hydrolysis of PCL by Mors1 and OaCut	66
Figure 23. Effect of NaCl and buffer on the hydrolysis of PCL nanoparticles by Mors1.....	68
Figure 24. Initial PCL hydrolysis rates by Mors1 (blue) and <i>IsPETase</i> (green) at varying enzyme concentrations	70
Figure 25. Enzymatic degradation of amorphous PET films.	71
Figure 26. HPLC elution profile of TPA and MHET detected in the supernatant of reaction mixtures of Mors1 and <i>IsPETase</i> with amorphous PET films	72
Figure 27. Optical density at 600nm of a PCL nanoparticle suspension during time incubated with Mors1 and MHET	73
Figure 28. Comparison of the sequence and structure of Mors1, OaCut, <i>IsPETase</i> , <i>TfCut2</i> , and LCC ...	74
Figure 29. Local structural dynamics of Mors1	76
Figure 30. Sequence variability of potential polyester hydrolases from Antarctic metagenomes	78
Figure 31. Variants of Mors1 and their activity on PCL and PET	82
Figure 32. T_m values of Mors1 and variants.....	84
Figure 33. Activity of CM ^{C266A} on PET compared to Mors1	87
Figure 34. PCL degradation with crude extracts.....	89
Figure 35. Average backbone RMSF of Mors1 and CM ^{A266C}	92
Figure 39. Comparison of the crystal structures of PHL7 and LCC and docking experiments	96
Figure 40. Predicted per-residue binding energy contributions for TPA (A) and MHET (B) in PHL7 and LCC.....	97

Supplementary Figure 1. Homology models of Mors1 generated using Rosetta3.....	124
Supplementary Figure 2. SDS-PAGE with fluorescent labelling of free cysteines in Mors1 and BSA	125
Supplementary Figure 3. RMSD time plots for all MD simulations	126
Supplementary Figure 4. First derivative of the ratio of the fluorescence measured at 350 and 330 nm from 20 °C to 90 °C of the variants of Mors1.....	127
Supplementary Figure 5. First derivative of the ratio of the fluorescence measured at 350 and 330 nm from 20 °C to 90 °C of the variants of Mors1.....	128
Supplementary Figure 6. Homology models of CM ^{A266C} generated using Rosetta3.....	129
Supplementary Figure 7. Superimposition of a representative structure of EMT, MHET and TPA clusters with the solved structure of <i>IsPETase</i> in complex with HEMT and p-nitrophenol for PHL7 and LCC.....	130
Supplementary Figure 8. Radial dendrogram of the hierarchical clustering distance matrix of the 100 lowest binding energy complexes of LCC and PHL7 and their corresponding ligands (EMT, MHET and TPA).....	131
Supplementary Figure 9. Lowest RMSD pose of the 0.25% best interface binding energy complexes.	132

List of Tables

Table 1. Onset temperature for denaturation and melting temperature (T_m) of Mors1, OaCut and <i>IsPETase</i> determined with nanoDSF	67
Table 2. Kinetic parameters of PCL hydrolysis by Mors1, <i>IsPETase</i> , Tcur1278 and Tcur0990	70
Table 3. Melting temperatures of Mors1, CM and CM ^{A266C}	88
Supplementary Table 1. DNA and protein sequences for OaCut, Mors1 and CM in their truncated version and without the signal peptide.....	133
Supplementary Table 2. DNA sequence of primers used. R: reverse primer. F: forward primer	135
Supplementary Table 3. PCR steps for mutagenesis.....	137
Supplementary Table 4. Crystals obtained under different conditions (buffer, salt, and polymers) for OaCut and its variants	138
Supplementary Table 5. Rosetta energy of the 10 selected models of Chimeric Mors1 (CM ^{A266C}) after relaxation.....	142
Supplementary Table 6. Structural evaluation of Mors1 models in comparison to the crystal structure of <i>IsPETase</i> (PDB 6EQE, chain A).....	143
Supplementary Table 7. S-H: Distance between γ hydrogen of S160 and ϵ nitrogen of H237. D-H: Distance between δ oxygen of D206 and δ hydrogen of H237.....	144
Supplementary Table 8. Sequences homologous to Mors1 identified in Low and High <i>Chla</i> Antarctic marine metagenomes.....	145
Supplementary Table 9. Best-hit BLASTP of the candidate enzymes identified in Chile Bay metagenomes.....	146
Supplementary Table 10. Number of enzyme-ligand complexes in each cluster obtained from a hierarchical clustering distance matrix.....	147

CHAPTER I.

THEORETICAL FRAMEWORK

Introduction

Polymers

Polymers are molecules composed of subunits linked by covalent bonds of natural or artificial origin. Natural polymers are widely distributed in nature: cellulose, starch, hyaluronic acid, collagen, gelatin, or albumin are some examples (Doppalapudi et al. 2014). Natural polymers are composed of a series of repetitive subunits, such as amino acids or sugars, whose synthesis is regulated by cells. Their composition and structure vary depending on the cell species, tissue type or cellular age (Pawelec et al. 2019).

Synthetic polymers, on the contrary, are man-made polymers derived from fossil fuels produced through different types of chemical reactions. Many of them are simple hydrocarbons that are transformed into polymers by adding one monomer after another to form long chains, such as polyethylene, nylon, polyester, Teflon, and epoxy. Their main advantage over natural polymers is that they offer an infinite spectrum of mechanical properties that natural polymers often lack. Since their synthesis can be modulated, different sizes, degrees of crystallinity and cross-linking can be obtained, making them versatile and suitable for countless applications (Pawelec et al. 2019).

Physical properties of polymers

Polymers composed of only one type of monomer are homopolymers, whereas if they contain a mixture of different monomers, they are called copolymers. The degree of polymerization is related to the number of subunits that constitute the polymer. The higher the degree of polymerization, the higher the molecular mass of the polymer. The molecular weight of a polymer is calculated as a distribution of the lengths of the polymer chains (Calhoun 2016). When the distribution of size, mass or shape between the chains is homogeneous, the mixture is called monodisperse, as is generally the case for natural polymers. Otherwise, when the distribution is heterogeneous, the blend is polydisperse, which is typical of synthetic polymers (Balani et al. 2015).

The chains that compose a polymer can be linked by Van der Waals attractions or by hydrogen bonds if amide and carbonyl groups are present (**Figure 1 A**). Bonding between adjacent chains causes a reduction in mobility that makes the polymer more resistant to tensile stresses and increases its melting point (Crawford and Quinn 2017). Depending on the spatial arrangement of the polymer chains, polymers can be crystalline or amorphous, although both regions are typically present in polymers. The crystalline regions are arranged in lamellar structures that are embedded in the amorphous regions (**Figure 1 B**), and a high degree of crystallinity is related to a high melting temperature and low impact strength (Balani et al. 2015). The size of the polymer chains and the strong interactions between them make the polymers difficult to dissolve. Only strong solvents can break these interactions and penetrate between them. When this adsorption occurs, the polymer increases in volume and becomes viscous. Amorphous polymers are more prone to dissolve, as the solvent can more easily penetrate the chains (Balani et al. 2015; Crawford and Quinn 2017).

Mechanical properties of polymers

Polymers exhibit mechanical properties that are determined by their molecular structure. One of the most important is strength, which is the stress required to break the material. It can be tensile, when the polymer is stretched, compressive, torsional, impact and flexural (referring to bending) (Balani et al. 2015). In general, a polymer is more resistant to deformation when it has a high molecular weight, a high degree of crystallinity and a high level of cross-linking due to reduced inter-chain mobility. The “Percent Elongation Break” measures the percentage increase in length that a polymer can reach before cracking. Similarly, Young's Modulus is a measure of the elasticity of the polymer as the ratio of the applied stress to the deformation of the material in the elastic region. Elastomers, for example, have a low Young's modulus, while stiff materials have a high Young's modulus. The amount of energy that a material can absorb until fracture is what is known as toughness (Galeski 2003).

Thermal properties of polymers

With increasing temperature, the polymer chains become more mobile, and the polymers undergo a change from a glassy state, which is known as amorphous solid, to a rubbery state. The temperature at which this process occurs is the glass transition temperature (T_g) and it only affects the amorphous regions. As the glassy state is not in equilibrium, the transition temperature of a polymer can vary depending on the rate of heating and cooling, the molecular weight of the polymer, the intermolecular forces, the chain stiffness, the level of cross-linking between the chains, and the presence of pendant groups in the chains (Balani et al. 2015). The melting temperature (T_m), on the other hand, is a state function and only applies to crystalline regions. It is the temperature at which the transition between the crystalline phase and the amorphous phase occurs (Crawford and Quinn 2017). T_m depends on the lamellar thickness of the crystal and the increase in lamella thickness is dependent on the crystallization time and temperature. The rate of lamella growth depends proportionally on the logarithm of the crystallization time of the samples (Weeks 1963).

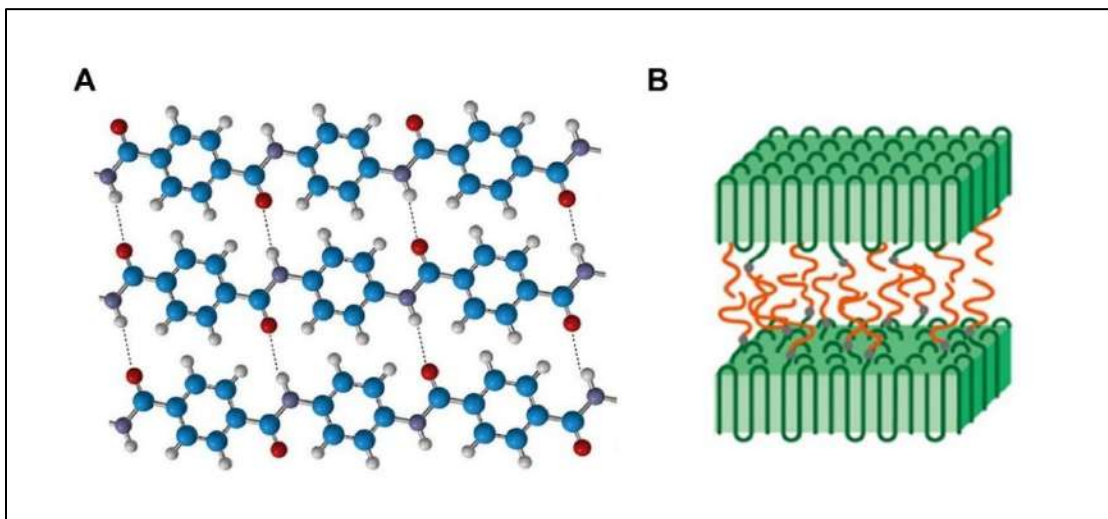


Figure 1. Polymer structure. A) Polymeric chains bonded by hydrogen bonds. Hydrogen bonding of Poly (azanediyli-1,4-phenyleneazanediyli-terephthaloyl), known by its trade name as Kevlar[®], one of the synthetic polymers with a higher tensile strength used for the fabrication of bulletproof vests. Hydrogen bonds are represented as dotted lines. Blue balls represent carbon atoms, red balls, oxygen atoms and purple balls, nitrogen atoms (Ouellette and Rawn

2015). **B)** Schematic model of a semicrystalline polymer. Crystalline regions are represented as lamella in green and the amorphous domains, in orange, are placed in between (Nakagawa et al. 2015).

Classification

Based on their physical properties, polymers can be classified in three major groups: elastomers, plastics, and fibers. Elastomers are amorphous polymers that can return to their initial shape when deformed. They consist of carbon-carbon double bonds separated by intermediate units containing two sp^3 -hybridized carbon atoms. Depending on the groups attached to the sp^3 hybridized carbon atoms and the geometry of the chains around the double bond, the polymer will be less or more flexible (Ouellette and Rawn 2015).

Plastics, on the other hand, are polymers that harden upon cooling. They can be classified as follows:

1. *Thermoplastics*

The peculiarity of thermoplastics is that they can melt and solidify on cooling. When a thermoplastic is heated, chains move as a result of increased kinetic energy; if the energy is sufficient to cause the chains to separate by breaking the intermolecular forces, the polymer melts (Ouellette and Rawn 2015). By cooling the polymer, the intermolecular forces between the polymer chain can be restored and the polymer regains its molecular structure (Gad 2014). Examples of common thermoplastics are polyethylene (PE), polypropylene (PP), polyvinyl chloride (PVC), polyethylene terephthalate (PET) and polystyrene (PS) (Streit-bianchi et al. 2020).

2. *Thermosets*

Thermosets are those that form covalent bonds between polymer chains. They do not usually melt when heated but undergo decomposition and cannot recombine again after cooling. Their chains are cross-linked differently from thermoplastics (Ouellette and Rawn 2015). Examples of thermosets are polyurethanes (PUR).

3. *Semisynthetic polymers*

These polymers have a natural origin but have been modified by eliminating or adding parts or by cross-linking. Examples include methylcellulose and cellulose acetate (Streit-bianchi et al. 2020).

4. *Hydrogels*

Hydrogels consist of networks of hydrophilic chains that do not dissolve in water. Depending on the degree of cross-linking they can incorporate a variable number of water molecules. They can be synthetic or natural and are commonly used for contact lenses, wound dressings, or drug delivery. Some examples are cellulose and polyethylene glycol (Gad 2014).

Finally, fibers are plastic filaments with a length greater than 500 nm with strong intermolecular forces that allow them to resist tensile strength (Ouellette and Rawn 2015).

Production, usage, and impact of synthetic polymers

The use of plastics has increased exponentially in recent decades. Plastics have become indispensable in modern society for food packaging, clothing, automobiles, housing, medicine, etc. The reason for the massive use of plastics is their valuable properties, such as durability, malleability, and transparency, at a low economic cost. The annual world production of plastics is estimated at 368 million tons, with a growth rate of 3.8 per year (Wei and Zimmermann 2017a). Packaging is the industrial sector that produces most of the plastic worldwide, with an estimated production of 146 million tons only in 2015, followed by construction and textiles (Geyer et al. 2017).

The most abundant types of plastic produced are PE, PP, PVC, PET, PUR, and PS. These seven groups of plastics correspond to 92% of all plastics ever made. Moreover, the most common fiber polymers are made from polyester, polyamide, and acrylic (PP&A), with polyester, which is mostly PET, accounting for 70% of all PP&A fiber composition (Geyer et al. 2017).

Many of these plastics are used in the packaging industry. Most common applications of high-density polyethylene (HDPE) are liquid containers such as bottles of milk, detergent, and cleaning products. Low density polyethylene (LDPE) is mostly used for bags, food packaging and plastic film. PP, on the other

hand is very versatile and can be applied for packaging of corrosive substances like bleaches or detergent and to medical components and pieces in vehicles and machinery, among others. PET is mainly used for beverage bottles and clothing fibers (Streit-bianchi et al. 2020).

The high production of plastics together with the low cost of production generates vast quantities of waste every year that is causing unprecedented environmental damage. While the largest amounts of plastic waste generated annually come from PE and PP, the ratio between waste generation and production is higher for PET, for which 97% of the material produced is disposed of as waste (**Figure 2**) (Geyer et al. 2017), given its single-use or short-lifetime utilization by consumers.

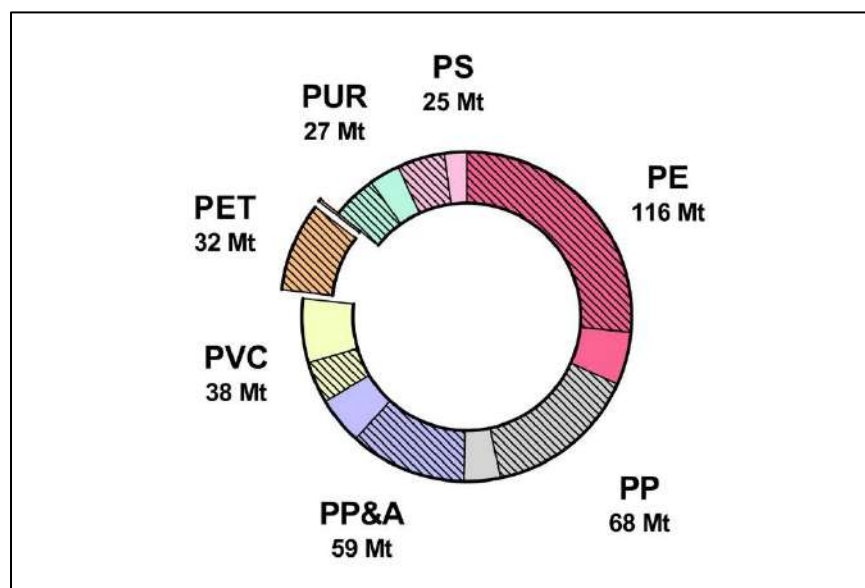


Figure 2. Global plastic production and waste per year. Most common plastics produced each year in the world in million tons (MT). The striped regions represent the fraction of each plastic that becomes waste. Almost all PET produced each year is disposed of as waste. Data extracted from Geyer et al. 2017.

Only 30% of all the plastic produced since mass production began in 1950 are still in use. The remaining 70% is mostly in landfills (55%), and only a small part has been incinerated (8%) or recycled (6%). Of this recycled plastic, only 20% is still in use (**Figure 3**). The highest rates of plastic recycling worldwide are

from Europe (30%) and China (25%), while the rates of incineration from these same countries are 40% and 30% respectively (Geyer et al. 2017). Unfortunately, poor management and mismanagement of plastic waste has led to its accumulation in the environment, to the extent that 4.8 to 12.7 million tons of plastic waste enter the sea each year (Jambeck et al. 2015), conforming 90% of the oceanic solid waste (Oliveira et al. 2020) and is forecast to be more than 100–250 MT by 2025 (Peng et al. 2018).

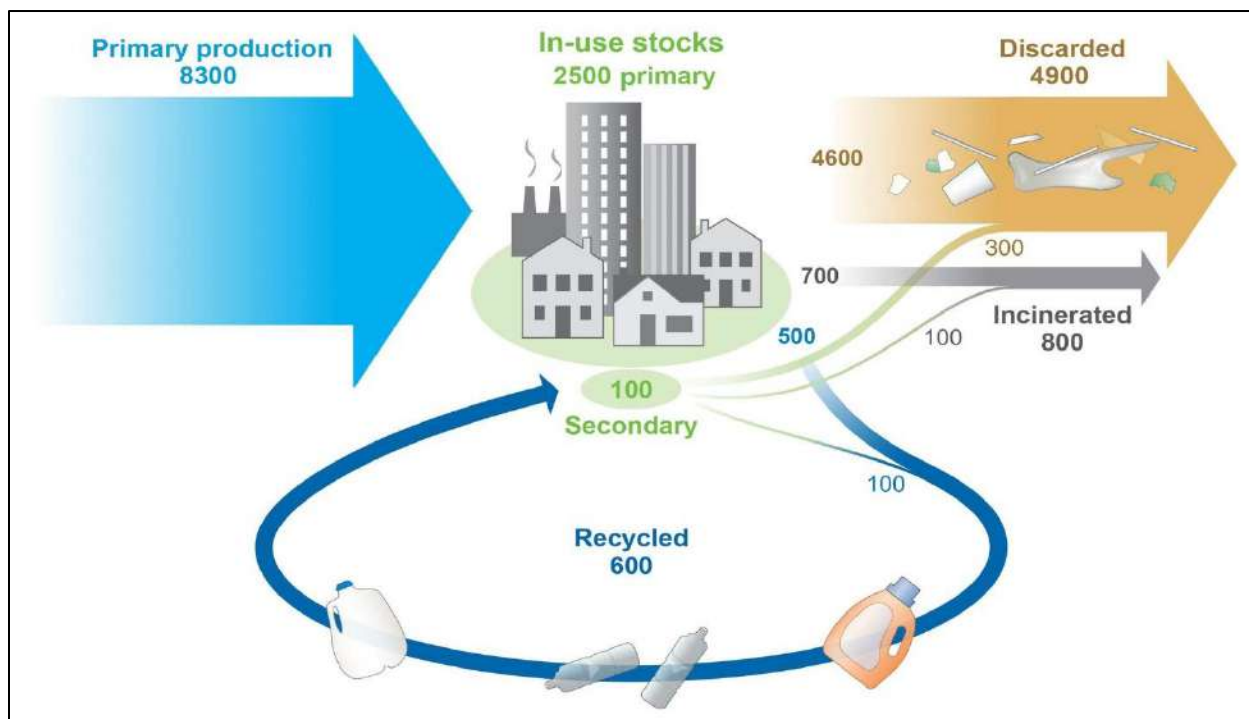


Figure 3. Fate of plastics produced from 1950 to 2015. Estimated plastic production since 1950 when the massive production started is of 8.300 MT. From this, just 30% are still in use while 55% have been discarded, 8% have been incinerated and only 6% have been recycled. Of this recycled plastic, 20% has been recycled a second time while the remaining 80% has been incinerated or landfilled (Geyer et al. 2017).

The presence of plastics in the marine environments has become a serious threat to marine organisms that often become entangled in fishing nets, boxes, and ropes, causing serious harm especially to turtles, fish, birds, and marine mammals. An emerging environmental and health problem arises with the breakage of

these plastics into small particles by abiotic factors, such as UV radiation, which generate the so-called microplastics and nanoplastics. These particles have an estimated lifetime of hundreds of years and have been found in every possible environment and location: in the deep oceans, Arctic snow, Antarctic ice, seafood, table salt, air, or drinking water (Lim 2021). The sources of microplastics are varied, from microbeads from personal care items to fragments released by the erosion of plastic waste to plastics torn from car tires and fibers from clothing. All these particles are ingested and inhaled continuously by animals and humans. The limited research available to date estimates that humans ingest from dozens to more than 100,000 microplastics and nanoplastics per year (Lim 2021). The threat of microplastics is not only the particle itself, but also that they often carry dangerous substances such as plasticizers, stabilizers and pigments that can interfere with the endocrine system. The dangerousness depends on how fast the plastic particles travel through the body and the speed at which these components are released from the plastic (Lim 2021). Studies on mice fed with large amounts of microplastics showed inflammation in their small intestine (Li et al. 2020). Moreover, mice exposed to microplastics had lower sperm counts (Jin et al. 2021) and fewer and smaller offspring (Park et al. 2020) compared to control groups. Regarding the accumulation in tissues, one study revealed that microplastics of about 5 μm in diameter could remain in the intestines or reach the liver, so a person could accumulate several thousand microplastic particles in the body over a lifetime (Mohamed Nor et al. 2021). As for how microplastics affect marine organisms, it has been observed that the presence of plastic particles alters the growth and reproduction of zooplankton. The reason would be that zooplankton would consume less food and therefore less nutrients when ingesting these particles. According to current evidence, this does not seem to be due to a toxicity effect (Botterell et al. 2019). In addition to the effects on living organisms, microplastics act as dispersers of hydrophobic contaminants throughout the seas and oceans. It has been shown that the concentration of hydrophobic contaminants in PP plastic pellets in seawater was up to 10^5 - 10^6 times higher than in the surrounding seawater (Mato et al. 2001). However, the greatest threat is represented by nanoplastics, which are small enough to penetrate tissues or even cells. Although the research on this subject is very reduced, one study revealed the presence

of plastic nanoparticles in almost all the organs of the fetuses of female rats exposed to these particles (Fournier et al. 2020).

Plastic is not only a source of pollution but also a source of greenhouse gases (GHG) (**Figure 4**). It is estimated that in 2019, production and incineration of plastics released 850 million tons of GHG into the atmosphere which equals to the emissions of 189 five-hundred-megawatt coal power plants (Hamilton et al. 2019). When referring to plastic production emissions, it means the extraction of fossil fuels, refining and transport. During the extraction of fossil fuels, emissions are caused by methane release, drilling for oil gas, and clearing forests for the construction of pipelines and wells. The downstream refining is considered one of the most polluting industrial processes. The cracking of alkanes into olefins (i.e., the process by which saturated hydrocarbons break down into unsaturated hydrocarbon to create the plastic resins) and the polymerization and plastification of these olefins produce huge amounts of GHG. Only the cracking to produce PE in 2015 generated as much CO₂ emissions as 45 million vehicles plants (Hamilton et al. 2019).

Other stage in the life cycle of plastics that causes GHG is their transport to landfills as well as the sorting and handling of waste (**Figure 4**). Landfilling is the main method of handling plastic waste, but it cannot be considered as a long-term method of plastics management, as one of the main detrimental effects of landfilling in the environment is the leaching of heavy metals from plastics into groundwater (Teuten et al. 2009).

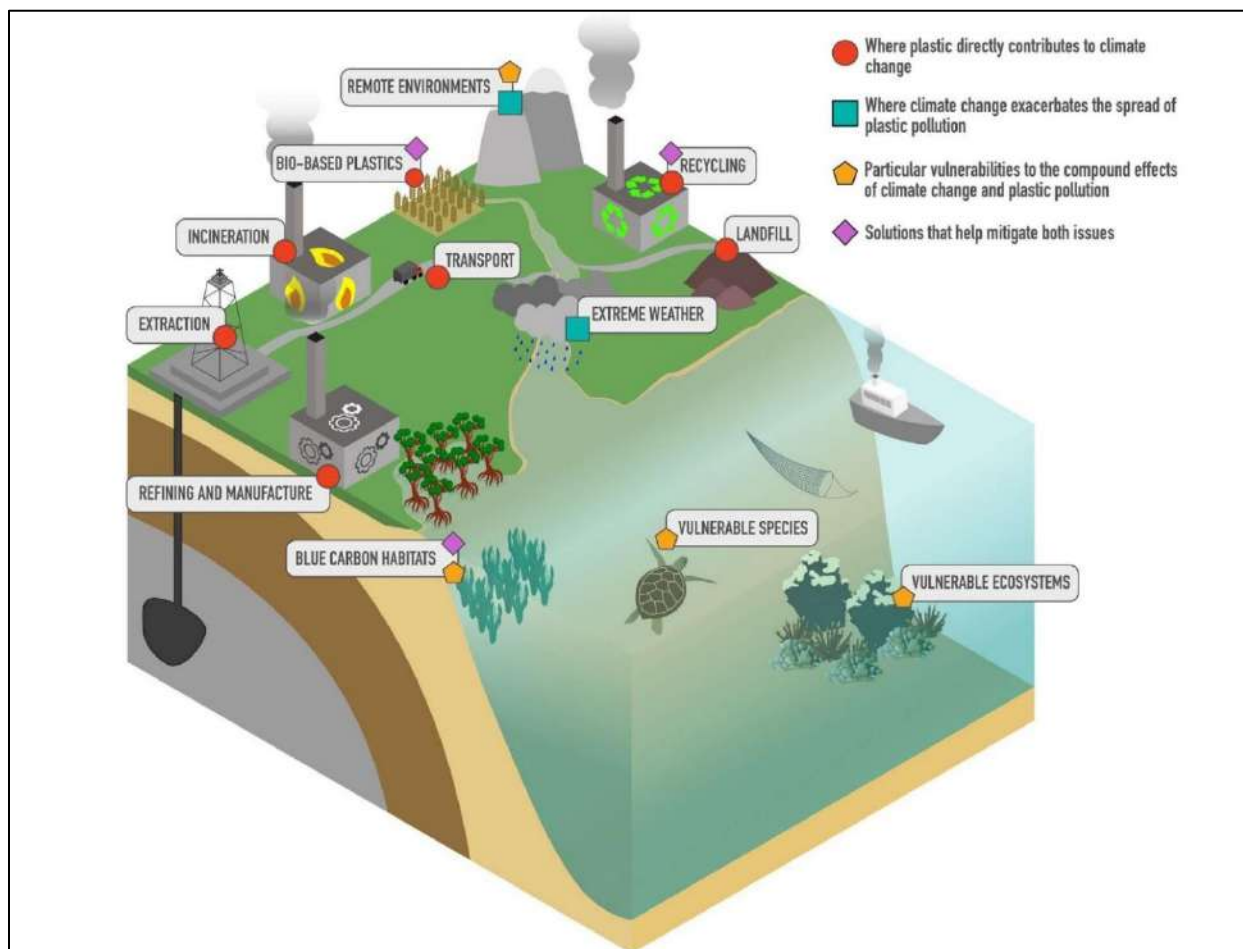


Figure 4. Interactions between plastic and climate. Plastic contributes to climate change through greenhouse gas emissions in its extraction, refining, transport, landfilling and recycling. At the same time, climate change cause extreme weather events that spread the plastic to vulnerable and remote environments (Ford et al. 2022).

Other way to dispose of plastics is through incineration, which basically involves breaking down and oxidizing the plastic using heat at temperatures around 230 °C in the presence of oxygen (Hamilton et al. 2019). Although the energy produced by incineration is reused by some industries, it comes at a great cost in pollution due to the release of air pollutants, ash, gases, and wastewater. It has been estimated that burning 1 MT of plastic produces 0.9 MT of CO₂ emissions, even considering the energy produced in the process.

GHG emissions attributed to plastic packaging incineration per year are 16 million tons. In the US, GHG emissions due to plastic incineration equal 1.26 million vehicles driven in a year (Hamilton et al. 2019).

In recent years, the so-called “bioplastics” have been proposed as an alternative to fossil-based plastic consumption. These are plastics that partially or completely derive from natural feedstocks, avoiding the use of fossil fuels such that their impact to global warming is considerably lower. They are typically made from sugar cane, corn, cassava, or sugar beet, and they have the same mechanical properties as traditional plastics. Examples are plant-derived PET, polylactic acid (PLA) and polyhydroxyalkanoate (PHAs). However, the processes of farming, distillation and dehydration that are required to their production have greater negative effects in terms of ozone depletion, smog, soil acidification, eutrophication, carcinogenesis and ecotoxicity than traditional plastics (Hottle et al. 2013). Also, there is a belief that these bio-based plastics are compostable but most of them are not, therefore they accumulate in the environment in the same way as the fossil fuels-based polymers do (Narancic et al. 2018).

Reusing plastics through recycling reduces the ecological cost in terms of GHG emissions three times more than *de novo* synthesis of the materials (**Figure 5**). With improved recycling techniques, this difference in emissions between recycling and production is expected to be almost 50 times greater. Recycling 1 MT of plastic avoids the release of 1.4 MT of GHGs, which means that recycling has a direct impact on reducing climate change. The main technical problems that recycling faces are the material sorting, removal of colorants, additives, and fillers, as well as consumer contamination. In addition, the low yield rates of current recycling techniques pose a challenge for this strategy to gain popularity. Another constraint, this time economic, is that virgin plastic is extremely cheap to manufacture, which reduces the value of recycled plastics and hinders the growth of this market (Hamilton et al. 2019).

In conclusion, phasing out plastic production linked to recycling are the most two effective strategies to end plastic pollution and reduce the CO₂ emissions (**Figure 5**). Reducing plastic production should be about replacing traditional plastic packaging with reusable alternatives, but not about replacing plastic with other

single-use materials, as this would perpetuate a linear, throwaway economy rather than a closed-loop system of production and consumption in which energy can be continuously recovered. Economically, the discarding of single-use plastics, which accounts to 95% of the plastics produced, generates an economic loss of 80-120 billion USD each year in the United States (Taniguchi et al. 2019). Recycling all plastics produced annually could save approximately 176 billion USD (Rahimi and García 2017).

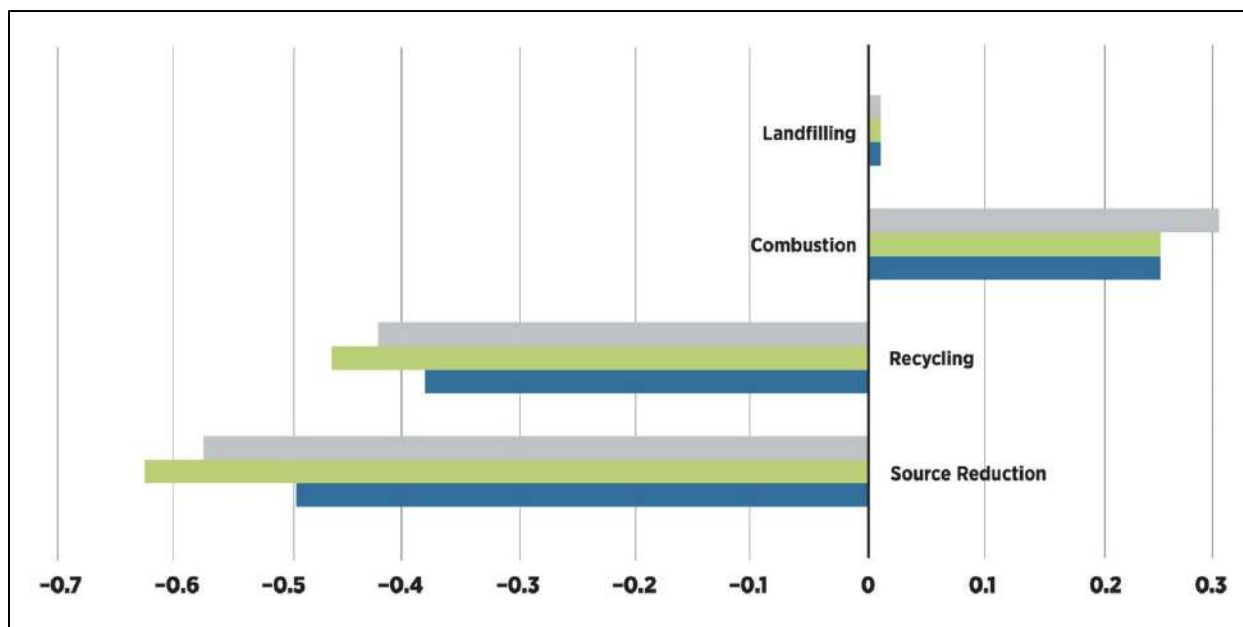


Figure 5. Contribution to net GHG emissions by different strategies in plastic production and waste management. GHG emissions in MT CO₂ equivalents per ton of plastic. For PET (grey), LDPE (green) and HDPE (blue). Source reduction and recycling decrease GHG emissions while combustion and landfilling increase them. Data source: U.S. EPA (2006). Image: (Hamilton et al. 2019).

PET production and recycling

PET is a thermoplastic composed of long carbon chains with aromatic rings (**Figure 6**), primarily used in the beverage packaging industry. The global PET market is expected to reach USD 38 billion by 2023 (Satsangi 2017). PET is synthesized by two ways: esterification of terephthalic acid (TPA) and ethylene

glycol (EG) with water as a byproduct or transesterification of dimethyl terephthalate (DMT) by methanol as a byproduct (Ravindranath and Mashelkar 1986). These two reactions form bis(hydroxy- ethyl) terephthalate (BHET) which is then condensed to form PET (**Figure 7**). Due to the industrial production of highly purified TPA esterification is the most common process nowadays (Park and Kim 2014).

Although strategies for PET waste management and recycling exist, currently only a fraction of PET waste is recycled (Garcia and Robertson 2017). Regarding the methods for the chemical recycling of PET, the most popular are methanolysis and glycolysis. In methanolysis, the ester bonds are broken by methanol with the resulting products DMT and EG. This process is carried out under pressures of 2-4 MPa and temperatures of 120-280 °C using zinc acetate often as a catalyst (Paszun and Spychaj 1997; Mishra and Goje 2003).

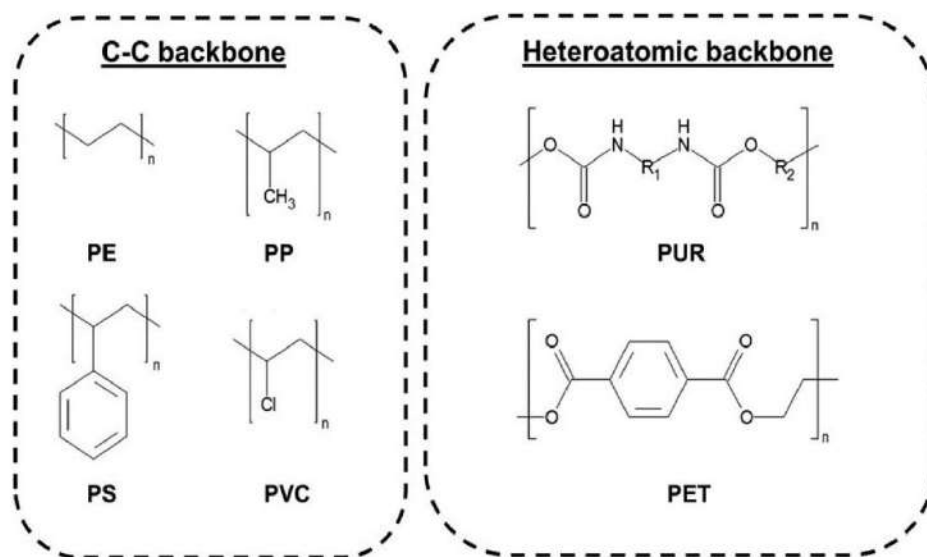


Figure 6. Chemical structure of the most common used synthetic plastics (Wei and Zimmermann 2017b).

The second most used chemical process for the industrial recycling of PET is glycolysis. This process, carried out in a temperature range of 180-250 °C, consists of breaking the ester bonds of PET with EG, obtaining the resulting BHET and EG. Since EG is also the catalyst for the reaction, the depolymerization rate is proportional to the square of the EG concentration (Chen et al. 1991).

Although these recycling techniques produce a high-quality PET with the same properties as virgin PET, the chemicals required, the infrastructure and the transport of the waste polymer often make the price of recycled PET higher than the cost of synthesizing new PET (Paszun and Spychaj 1997). In addition, there are health risks associated with the use of some compounds, such as methanol.

As an alternative to chemical recycling, mechanical recycling is a much cheaper and less polluting method, which consists of grinding and shredding PET into flakes that are extruded into pellets or fibers and reprocessed. However, the recycled material is of low quality, as the heat used in the process causes photo-oxidation whereby the molecular weight is reduced as well as the viscosity leading to deterioration of the product in each recycling cycle (Park and Kim 2014). As an example, bottle-to-bottle mechanical recycling of PET requires to use at least 70% of virgin PET to maintain the properties of the material (Schyns and Shaver 2021).

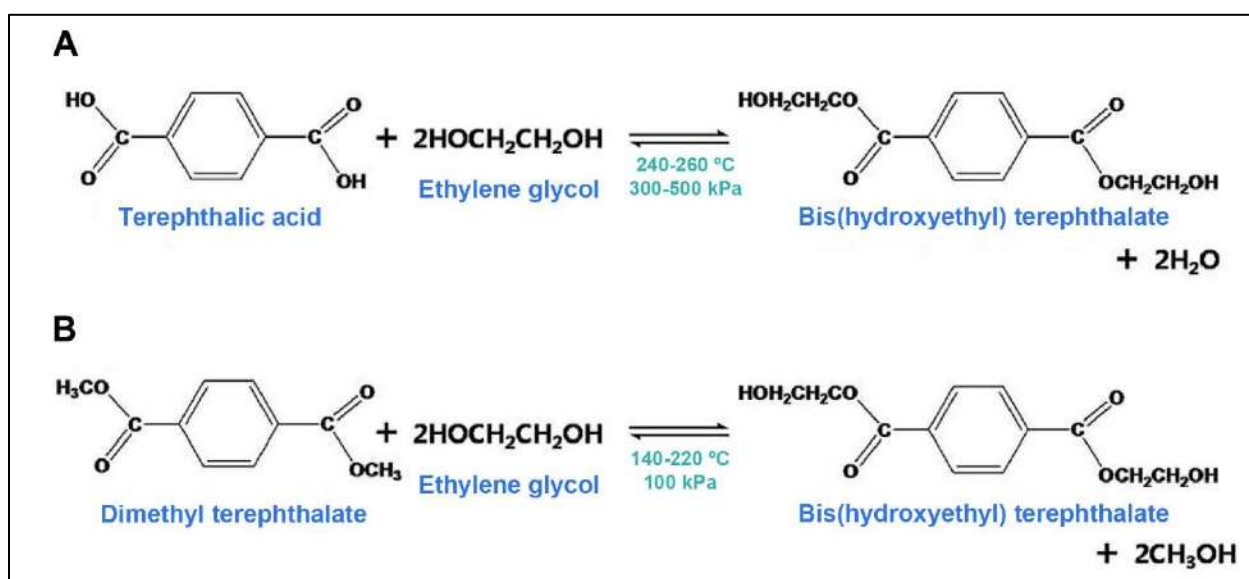


Figure 7. Synthesis reactions for PET. A) esterification B) transesterification. Modified from Park & Kim, 2014.

Biocatalysis as a solution to plastic pollution

Biocatalysis is the application of enzymes and microorganisms in synthetic chemistry, with environmentally positive effects falling under what is considered "green chemistry": the use of natural catalysts, biodegradable and non-toxic, together with mild reaction conditions of temperature, pH, and pressure and the avoidance of metals and traces (Sheldon and Woodley 2018). Over the past ten years, scientific and technological advances have established biocatalysis as a practical and environmentally friendly alternative to traditional catalysis at both industrial and laboratory levels (Bornscheuer et al. 2012). Nowadays, biocatalysis plays an important role in the mainstream organic chemistry, especially for enantioselective synthesis of active pharmaceutical intermediates (Sheldon and Woodley 2018).

Since biocatalysis began to be applied for chemical synthesis more than a hundred years ago, there are considered to have been three major waves or stages. The first wave started with the usage of components of living cells, such as plant extracts or microbial cells to synthesize chemicals. The limitation of these processes was mainly the instability of the catalysts, but this issue could be partially overcome by immobilizing the enzymes (Bornscheuer et al. 2012). The 1980s saw the development of the first protein engineering technologies that gave rise to the second wave of biocatalysis. These new methods allowed to develop new synthetic intermediates for drugs, herbicides, cosmetics, and polymers (Bornscheuer et al. 2012). The third wave of biocatalysis, which began in the mid-1990s and in which we now find ourselves, has been characterized by the development of directed evolution methods that have allowed rapid and extensive modification of biocatalysts (Arnold 1996; Bornscheuer et al. 2012). The development of these advanced molecular biology methods, such as error prone polymerase chain reaction (PCR), DNA shuffling and high-throughput screening have made it possible to mimic, artificially, the processes of Darwinian evolution that have always occurred naturally (Poppe and Vértessy 2018). The creation of "smart libraries" to reduce the number of variants and the number of iterative cycles of screening have improved the efficiency of these methods substantially. In addition, the development of bioinformatics tools and advances

in gene synthesis and sequencing have played a key role in the advancement of this third wave (Bornscheuer et al. 2012).

Biocatalysis would not have reached its current level of development were it not for advances in protein engineering, which has made possible to modify the original functions of natural enzymes and create new or improved functions in terms of specificity, selectivity, cofactor binding or thermostability. In general terms, protein engineering methods can be classified as directed evolution approaches, which do not require any knowledge about the structure of the enzyme, and knowledge-based approaches, which use a rational design that relies on prior information about the structure-sequence-function relationships of the enzyme.

The “irrational” approaches, such as directed evolution, mentioned above (Arnold 1996), consist of introducing mutations randomly and testing which variants have acquired the desired property by a selective screening. This requires a high-throughput screening method that allows myriad variants to be tested easily and quickly. Rational approaches, on the other hand, involve modifying specific residues of a protein based on detailed prior structural and functional information, thus creating a small number of variants to test through site-directed mutagenesis (Carter 1986). “Semi-rational” approaches combine random mutagenesis with rational design, targeting specific residues based on prior knowledge and replacing them with all (or a subset of) the 20 amino acids, creating libraries with a reduced number of variants. Having a high-throughput screening method in this case is advantageous, but not essential (Chica et al. 2005).

In the search for new plastic recycling methods that are environmentally friendly, sustainable, and low cost, the use of enzymes from microorganisms as biocatalysts has been proposed as a new alternative. In 1977 Tokiwa and Suzuki reported for the first time esterases and lipases able to hydrolyze aliphatic polyesters such as polycaprolactone (PCL) and poly(ethylene adipate) (PEA) (Tokiwa and Suzuki 1977).

Polymers with hydrolysable functional groups such as PET and PUR are more prone to biodegrade. For this reason, research on the biodegradation of synthetic polymers has mainly focused on the discovery of enzymes that hydrolyze these polymers, especially PET. Polymers with a C-C backbone, such as PE, PS,

PP and PVC are very unlikely to be degraded with enzymes because of the low reactivity of their bonds (**Figure 6**) (Wei and Zimmermann 2017b). Nevertheless, some laccases, lipases, and manganese peroxidases capable of degrading oxidized PE have been described. The most remarkable is a laccase from the ligninolytic fungus *Trametes versicolor* that decreased the molecular weight of a PE layer by an 88% in three days in presence of a redox mediator (1-hydroxybenzotriazole) (Fujisawa et al. 2001). Also, a lignin degrading fungus, *Phanerochaete chrysophobia* (MTCC-787) has been reported to cause a weight loss of 70% of oxidized polyethylene films after 15 days of incubation (Mukherjee and Kundu 2014). Regarding PS, a hydroquinone peroxidase from a lignin decolorizing bacterium, *Azotobacter beijerinckii* HM121, has been described to rapidly degrade this polymer solubilized in an organic phase in the presence of hydrogen peroxide and tetramethylhydroquinone (Nakamiya et al. 1997). No enzyme or organism has been reported to degrade PVC to date. Unfortunately, all the studies mentioned above have been carried out with semi purified enzyme, so it is not possible to obtain accurate and comparable data from them.

Discovering PET-degrading enzymes

The enzymes that have been characterized as PET degraders to date are of the esterase type (EC 3.1), mainly cutinases (3.1.1.74). Cutinases are the enzymes that degrade cutin, a polymer formed by hydroxylated 16- and 18- carbon fatty acids bonded together by ester bonds that is found in the cuticle of plants, a protective barrier composed of waxes and lipid polymers that prevents from dehydration and infection by pathogens. Cutinases can also degrade insoluble polymers, insoluble triacylglycerols, and soluble small esters (Chen et al. 2013). Although cutinases are structurally similar to lipases, their active sites are exposed to the solvent while in lipases it is buried under a cap domain. This cap is an amphiphilic α -helix, which undergoes a conformational change when in the presence of an oil-water interface. When the lid is opened, the hydrophobic residues on the underside bind to the lipid substrate and the structure is stabilized (Zisis et al. 2015). The absence of this lid allows cutinases to hydrolyze esters in solution and to accommodate longer polymers (Chen et al. 2013).

Cutinases catalyze the cleavage of ester bonds using water as a nucleophile. In the case of PET degradation, they hydrolyze this polymer into its monomers, TPA and EG, and also into the intermediates mono-(2-hydroxyethyl) terephthalate (MHET) and BHET (**Figure 8**), both of which are water-soluble (Vertommen et al. 2005). Structurally, these PET-degrading enzymes belong to the superfamily of α/β -hydrolases, featuring a highly conserved structure consisting of 8 or 9 β -sheets flanked by α -helices (**Figure 9**) and a catalytic triad composed of a nucleophilic residue (serine), an acidic residue (aspartate or glutamate) and a basic residue (histidine) (**Figure 9**) (Ollis et al. 1992). Topological conservation of these enzymes suggests that they come from a common ancestor and have diverged over time (Lenfant et al. 2013).

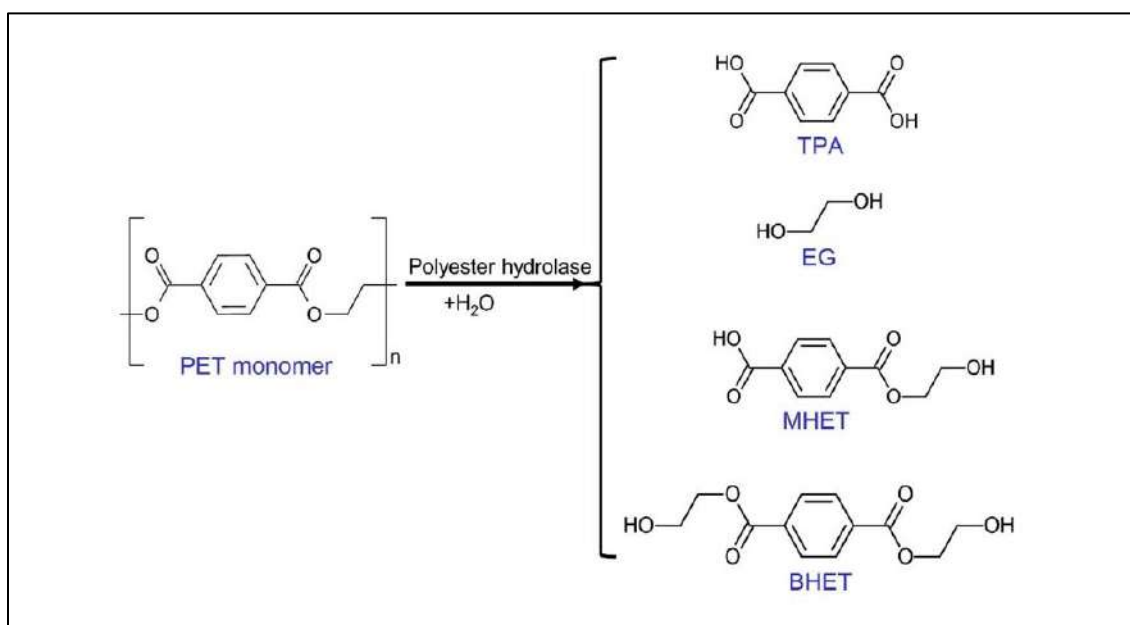


Figure 8. Products obtained from PET hydrolysis by polyester hydrolases. TPA, terephthalic acid; EG, ethylene glycol; MHET, mono-(2-hydroxyethyl) terephthalate; BHET, bis-(2-hydroxyethyl) terephthalate. Modified from: (Wei and Zimmermann 2017b).

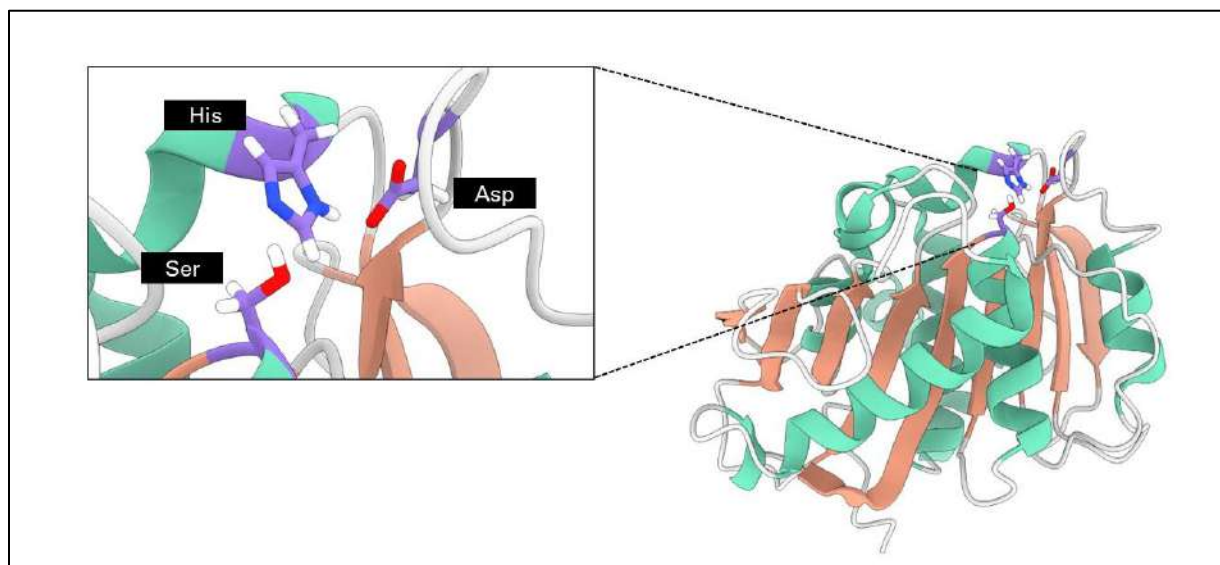


Figure 9. Structure and active site of an α/β hydrolase. Cartoon representation of a modeled structure of Mors1 (UNIPROT KB P19833), that shows the classic α/β hydrolase fold with 9 β -sheets surrounded by 6 α -helices and linked by loops. The catalytic triad is showed in red.

The reaction mechanism of PET hydrolysis starts with the nucleophilic attack of the serine to the carbonyl group attached to the first benzene ring of the PET. This attack is made possible by prior deprotonation of serine by histidine. Histidine is linked to aspartate by a hydrogen bond, and this increases the pKa of the imidazole nitrogen of histidine, allowing it to act as a strong base. Then, the substrate forms a tetrahedral intermediate that is stabilized by the oxyanion hole. The oxyanion hole is composed of two amino groups from a methionine and tyrosine. The tetrahedral intermediate releases an alcohol and then, by the attack of deprotonated water, acid is released. The catalytic mechanism ends by the release of the acid and the regeneration of the catalytic triad by rearrangement of electrons and proton of the histidine (**Figure 10**) (Jaeger et al. 1999).

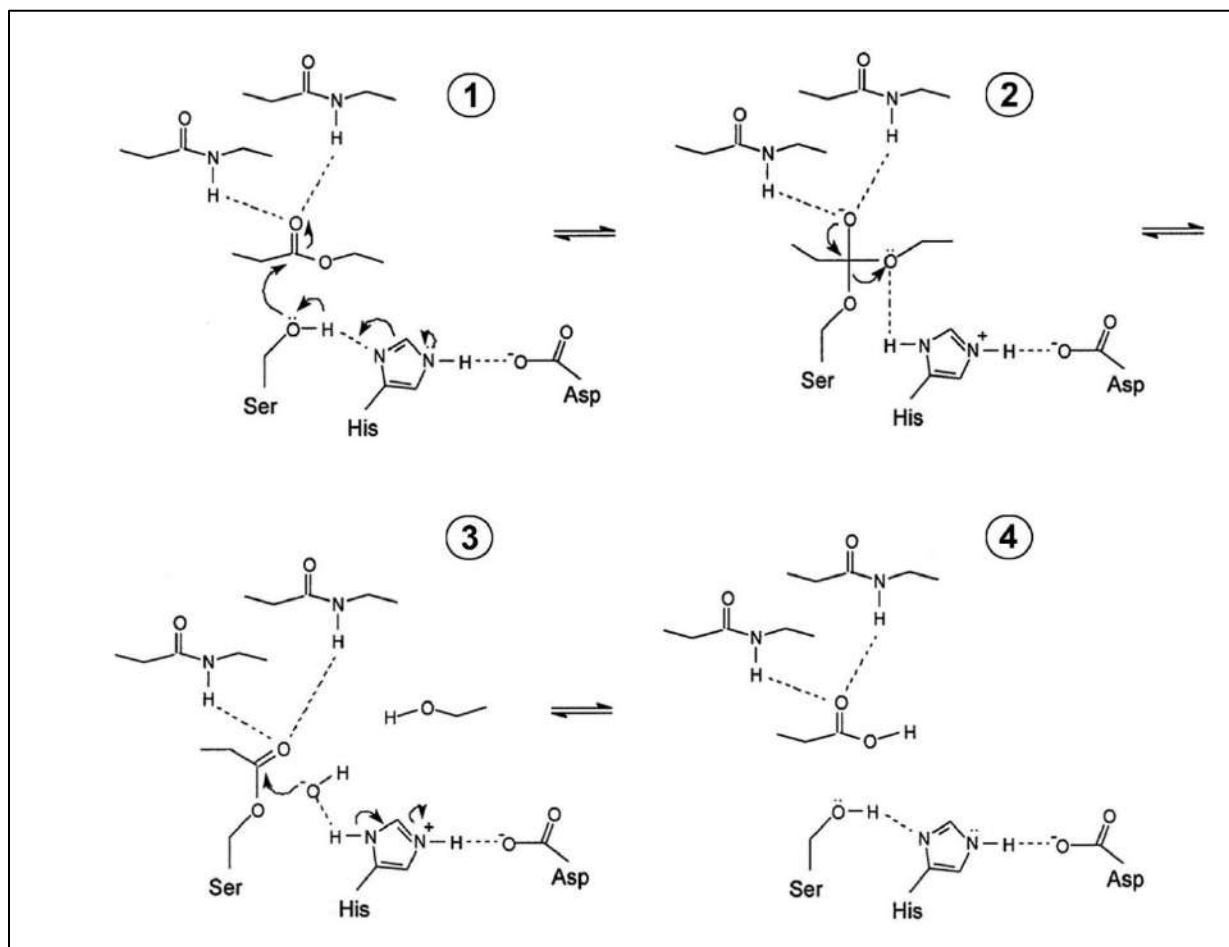


Figure 10. Catalytic mechanism of α/β hydrolases. 1) The substrate binds to the catalytic pocket, the serine that is activated by the histidine, attacks the carbonyl carbon atom of the substrate. 2) A tetrahedral intermediate is formed between the serine and the substrate, stabilized by two NH groups from residues of the oxyanion hole. The oxygen from the tetrahedral intermediate located in the oxyanion gives two electrons to the carbon, forming a π bond, and histidine donates a proton to the leaving alcohol component of the substrate. 3) A water molecule positions close to the histidine and is deprotonated. The water molecule, converted in a hydroxide with strong nucleophilic capacity, attacks the carbon from the covalent intermediate bonded to serine. 4) The histidine donates a proton to the oxygen of the serine, the ester bond between serine and the covalent intermediate is broken, and the acyl product is released (Jaeger et al. 1999).

Characterization and engineering of PET hydrolases

In recent years, research on PET hydrolases has increased enormously. The first enzyme reported to degrade PET (9% crystallinity, $T_g = 75\text{ }^\circ\text{C}$) was a hydrolase from the thermophilic bacterium *Thermobifida fusca* (TfH) (Müller et al. 2005). This enzyme hydrolyzed 54% of commercial PET film in 3 weeks at $55\text{ }^\circ\text{C}$ at a ratio of $25\text{ }\mu\text{g}$ enzyme per mg PET and showed erosion rates of 8 to $17\text{ }\mu\text{m}$ per week.

Later, a thermostable cutinase from the rot fungus *Humicola insolens* (HiC) was reported to hydrolyze 97% of low crystalline PET in 96 h ($7.5\text{ }\mu\text{g}$ of enzyme per mg of PET) which corresponds to a film thickness loss of $30\text{ }\mu\text{m}$ per day (Ronkvist et al. 2009). The combination of this enzyme with the MHET-hydrolyzing lipase from *Candida antarctica* (CalB), increased the production of TPA almost 8-fold (Carniel et al. 2017). HiC is the most active polyester hydrolase from a fungus reported so far.

In 2011, a homologous sequence to TfH was found in *Thermobifida fusca* KW3 strain (*TfCut2*) (Herrero Acero et al. 2011). This enzyme, together with its homologous *TfCut1* and TfH, showed enhanced thermostability in the presence of 10 mM CaCl_2 due to a cation binding site (Then et al. 2015). By replacing acidic residues of the Ca^{2+} binding site with arginines, it was possible to improve its thermostability in the absence of the calcium. This thermostabilized enzyme maintained its activity at $65\text{ }^\circ\text{C}$ in contrast to the WT enzyme but was less active at $60\text{ }^\circ\text{C}$. One hypothesis to explain this phenomenon is that the Ca^{2+} binding site was located close to the active site, so Ca^{2+} binding decreased the flexibility of the catalytic pocket, reducing activity at low temperatures. However, the increase in kinetic energy at $65\text{ }^\circ\text{C}$ would compensate the reduced flexibility of the active site by an overall higher flexibility of the enzyme, showing a 3.5-fold higher activity compared to the WT enzyme at $60\text{ }^\circ\text{C}$ (Then et al. 2015). Subsequent studies on *TfCut2* showed that it is strongly inhibited by MHET (Barth et al. 2015). However, by exchanging a binding residue in the active site with one present in LCC (G62A) the affinity of the enzyme for MHET decreased, increasing PET degradation activity from 17% to 42% in 50 h at $65\text{ }^\circ\text{C}$ (using $1\text{ }\mu\text{g}$ of enzyme per mg of PET) (Wei et al. 2016).

In 2014, a thermostabilized cutinase from the thermophilic bacterium *Saccharomonospora viridis* AHK190 (Cut190 S226P/R228S) was reported to hydrolyze 13.5% PET films at 63 °C in 3 days (using 1.3 µg of enzyme per mg of PET) (Kawai et al. 2014). In the same year, Sulaiman et al. isolated a cutinase-like enzyme from leaf-branch compost termed LCC, which was active at 65 °C and degraded 54% of PcW-PET (pulverized commercial PET) in 24 h at a ratio of 1 µg enzyme per mg of PET (Sulaiman et al. 2012).

The addition of a disulfide bridge in the vicinity of the active site of LCC (D238C/S283C) increased its T_m by 9.8 °C, reaching 94.5 °C. This variant, however, lost 28% of its activity. To restore the catalytic activity, the authors explored the key residues in binding by docking and selected eleven positions to mutate by site-specific saturation mutagenesis. As a result, 209 variants were created, of which 25 showed 75% or more activity than the WT enzyme. Among them, two variants with a mutation in position 243, which exchanged a Phe for either Ile or Trp, exhibited significantly better activity than the WT enzyme. These two mutations were added to the thermostable variant previously mentioned, creating the ICC (F243I/D238C/S283C) and the WCC (F243W/D238C/S283C) variants that restored the activity 122% and 28% and presented an increase in T_m of 6.2 °C and 10.1 °C, respectively, when compared to the WT. Moreover, from the 25 variants that showed 75% or more activity than the wild type, the ones with an increased thermal stability were chosen: T96M, Y127G, N246D and N246M. Then, these mutations were introduced into ICC and WCC, with the resulting variant ICCG (F243I/D238C/S283C/Y127G) presenting the best trade-off between specific activity and thermal stability, depolymerizing 90% of post-consumer PET in 9.3 h using 3 µg enzyme per mg PET. This is equivalent to a rate of $105.6 \pm 3.9 \text{ mg}_{\text{TAcq}} / \text{h mg}_{\text{enzyme}}$ (Tournier et al. 2020). Although the source organism of this enzyme is unknown, the gene sequence is homologous to that of *Thermobifida* polyester hydrolases (Wei and Zimmermann 2017a).

The good performance of LCC^{ICCM} was recently surpassed by another metagenomic enzyme from compost discovered by Sonnendecker and coworkers in 2021. This hydrolase, termed PHL7, whose characterization we collaborated on and is part of this thesis, completely hydrolyzed post-consumer PET in 18 hours at 70

°C (using 0.6 μg of enzyme per mg of PET) with an initial velocity of 13.6 $\mu\text{m h}^{-1}$. Although PHL7 presents a high identity to LCC (94%), its activity is twice as high as that for LCC (91 mg $\text{TPA}_{\text{eq}}/\text{h}/\text{mg}$ enzyme and 48 mg $\text{TPA}_{\text{eq}}/\text{h}/\text{mg}$ enzyme respectively) over a period of 4 to 8 hours, the range in which the rate for PHL7 is maximal (**Figure 11 A**) (Sonnendecker et al. 2021). The aminoacidic composition in the active site also exhibits similarities: residues G62, T64, S69, H130, M132, W156, A180, N213, together with the catalytic triad S131, D177, H209 are conserved (the numbering corresponds to PHL7). Only four residues within the binding pocket differ: F63 (LCC: Y95), L93 (F125), Q95 (Y127), I179 (V212). A Leu present in subsite II of PHL7 (L210) appears to be key to the superior activity of PHL7. When this residue is changed to Phe, a residue conserved in this position in LCC and other homologous of PHL7, the activity decreases by more than half. Conversely, the change to Leu from Phe in the homologous enzyme PHL3 increases the activity up to the level of PHL7 (**Figure 11 B**). The reason why this Leu plays such an important role is not clear, however docking studies showed a lower energetic contribution to PET binding of this Leu in contrast to Phe in LCC (Sonnendecker et al. 2021).

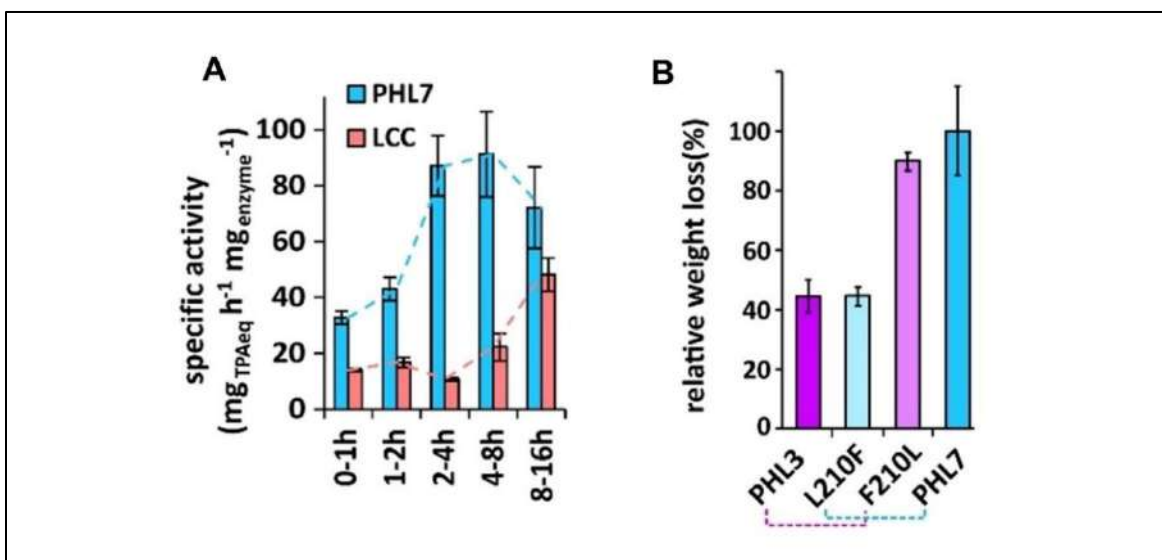


Figure 11. PET degradation assays by PHL7 and LCC. A) Specific activity of PHL7 and LCC measured as TPA equivalents (TPA_{eq}) per hour per mg of enzyme, released from PET films with 0.6 $\text{mg}_{\text{enzyme}}/\text{g}_{\text{PET}}$. **B)** Weight loss of PET films after 24h of reaction at 70 °C with 0.6 $\text{mg}_{\text{enzyme}}/\text{g}_{\text{PET}}$ for PHL7 and its homologue PHL3. When L210 is

mutated in PHL7 to Phe, the activity decreases. In contrast, when the Phe in PHL3 is mutated to Leu, the activity increases to the level of PHL7 (Sonnendecker et al. 2021).

Marten et al. showed that if the distance between the melting temperature of a polymer and the temperature at which degradation occurs is greater than 30 °C, biodegradation is not possible. Thus, given that PET has a T_m of 267 °C, hydrolysis of crystalline PET by enzymes is not expected to be possible (Marten et al. 2003). Consistently, all the enzymes described above degrade amorphous PET regions, having optimum temperatures of activity near the glass transition temperature of PET (~65 °C) where the chains of the polymer become more flexible, therefore being more prone to interact with the active site of the enzyme (Mueller 2006; Ronkvist et al. 2009; Sulaiman et al. 2012)

In 2016, Yoshida et al. described the first PET hydrolase with optimal activity at moderate temperatures (40 °C), termed “PETase”, subsequently named "*Is*PETase" by different authors. What was interesting about this enzyme was its mechanism to compensate for the high stiffness of PET at room temperature with a more flexible catalytic pocket that allowed a better fit of the substrate (Fecker et al. 2018). The increased instability of the active site was partially compensated by a disulfide bridge near the active center (C176-C212) not found in the thermophilic enzymes (Fecker et al. 2018). Moreover, the catalytic pocket of *Is*PETase was almost three times wider than in thermophilic enzymes (Austin et al. 2018). Nevertheless, the activity of *Is*PETase at 40 °C is very low when compared to LCC and PHL7 at 65 °C and 70 °C respectively (Tournier et al. 2020; Sonnendecker et al. 2021).

Regarding the key binding residues in *Is*PETase, it presents a Trp (W185, numbering corresponding to PDB 5XJH) that can adopt three different conformations (A, B and C) (**Figure 12**). When *Is*PETase is in the apo form, this Trp can be found in all three conformations, however, when the substrate is bound, the Trp is fixed in C conformation. In this position, the side chain is displaced from the active site allowing a better accommodation of PET.

This phenomenon of rotation of the Trp into different conformers to enable substrate binding has been termed as “wobbling”. In thermophilic cutinases, however, only A and B conformations are present. Comparison of the three-dimensional structures of *Is*PETase and thermophilic cutinases have indicated that the wobbling of Trp185 into three different conformations in *Is*PETase is allowed by a nearby Ser (Ser214) that permits the free movement of the lateral chain of the Trp. In thermophilic enzymes, there is a His at this position that prevents Trp wobbling (Han et al. 2017).

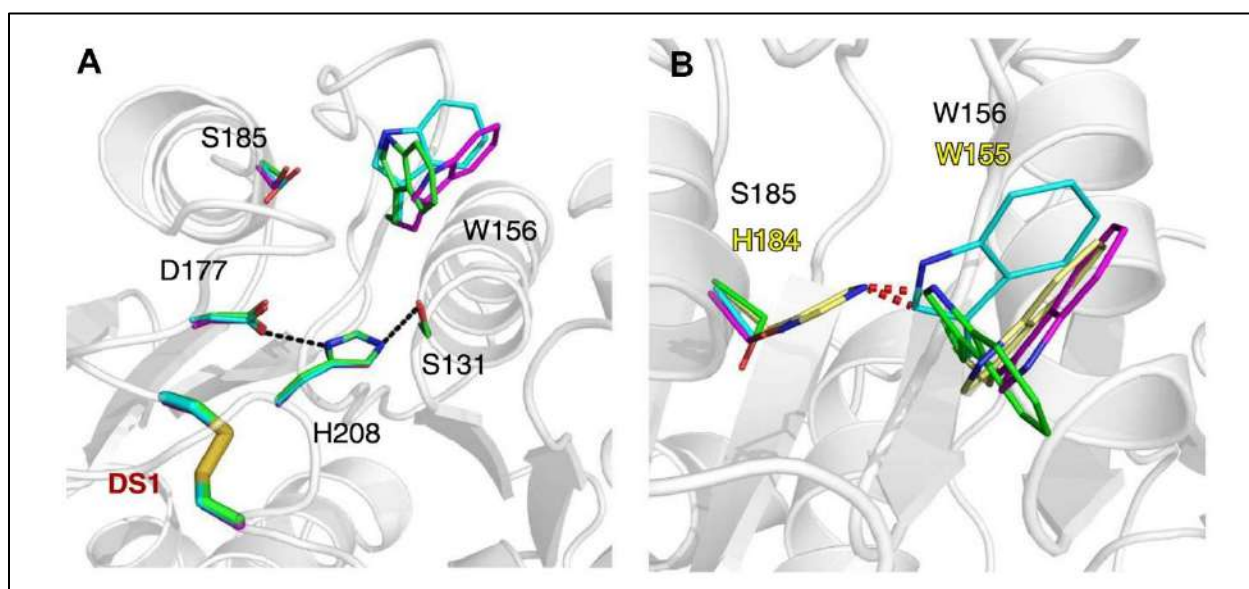


Figure 12. Active site of *Is*PETase in apo-form with the three different conformations of W185 (W156 in this image). A) *Is*PETase active site with the catalytic triad shown in sticks (S160, D206, H237; S131, D177, H208 in this image), as well as the three different conformations for W156: A (green), B (cyan), and C (magenta). Dash lines indicate distances <3.5 Å. DS1 stands for disulfide bridge 1. **B)** Comparison of *Is*PETase residue dispositions (in green, blue, and magenta) with the *Thermobifida fusca* PET degrading hydrolase (PDB ID, 4CG2) (in yellow). Residues W185 and S214 (PDB 5XG0) correspond in this image to W156 and S185 residues (PDB 5XJH). Red dash lines indicate distances <1.5 Å (Han et al. 2017).

There is also another Trp present in *IsPETase* (W159 in PDB 5XJH), which in thermophilic cutinases corresponds to His. This residue appears to be key in binding, since its mutation to His drastically decreases enzyme activity (Joo et al. 2018). Moreover, mutagenesis studies by Joo et al. found that lengthening of the active center by interchanging an Arg to Ala (R280A) improved catalytic activity by 32.4% over 36 h (Figure 13). In addition, Austin et al. created a double mutant (W159H/S238F) that resulted in a significant decrease in PET crystallinity and slightly improved activity by enhancing the π - π interactions with PET (Han et al. 2017).

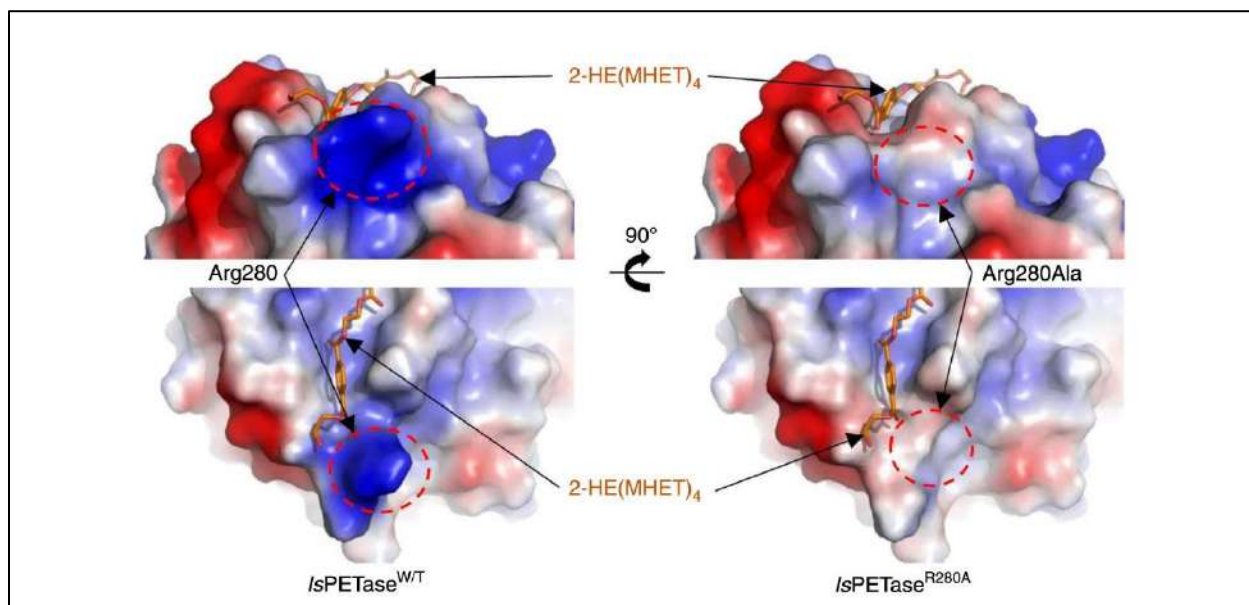


Figure 13. Active site of *IsPETase* and *IsPETase*^{R280A} in complex with 2-HE(MHET)₄. The mutation, indicated with dotted circles, produces an elongation of the binding pocket for the substrate (Joo et al. 2018).

Another remarkable mutation was the exchange of an Ile for Phe, a more polar residue, in position 208 (PDB 5XJH) increased the binding to the PET and thus the activity 2.5-fold (Austin et al. 2018; Ma et al. 2018; Joo et al. 2018). Furthermore, stabilization of the β 6- β 7 connecting loop by a double mutation

(S121D/D186H) increased the T_m by 6 °C. When the R280A mutation was added to this double variant, the hydrolytic activity increased 5.2-fold at 30 °C and almost 14-fold at 40 °C (Son et al. 2019).

Using a computational algorithm to simulate accumulative mutations termed GRAPE (Greedy Accumulated strategy for Protein Engineering), Cui and coworkers designed a multiple variant, with 10 residue substitutions, termed DuraPETase with an increased T_m of 31 °C. DuraPETase improved PET hydrolysis of semicrystalline (30%) PET films by 38-fold at 37 °C, and 170-fold at 50 °C, being this latest temperature the optimum temperature. Also, the long-term survival of the enzyme was dramatically enhanced from 1 day to 10 days. The improved activity and thermostability are believed to be due to the creation of new electrostatic interactions with the substrate (T140D, I168R, W159H, S188Q), an increased hydrophobic packing (Q119Y, A180I, S214H, R280A, L117F), a reduced conformational entropy (G165A) and an enhanced stabilization of substrate binding (L117F and Q119Y) (Cui et al. 2021).

On the other hand, a recent publication showed a multiple variant created by a 3D self-supervised convolutional neural network with activity similar to that of thermophilic LCC^{ICCM} enzyme (Lu et al. 2022). This computational tool, called MutCompute, uses an algorithm that predicts which residues in a protein are not optimized for their chemical environment by testing at each position the 20 canonical amino acids. Using as scaffold the thermo-stable PETase^{S121E/D186H/R280A} from Son et al. 2019, Lu et al. created a multiple variant, adding the N233K/R224Q mutations, named FAST-PETase (Functional, Active, Stable, and Tolerant PETase), which showed 2.4-fold and 38-fold higher activity at 40 and 50°C, respectively (**Figure 14**). The latter activity is similar to that of LCC^{ICCM}, but at a temperature 10 °C lower. In the experimentally solved crystal structure of this enzyme variant (PDB 7SH6) it could be observed that substituting Arg at position 224 by Gln forms a hydrogen bond with S192 (**Figure 15 C, D**). In turn, substitution of Asn233 by Lys established an intramolecular salt bridge with Glu204 (**Figure 15 E, F**).

Taken together, all these results demonstrate that there is ample scope for improving *Is*PETase activity by protein engineering.

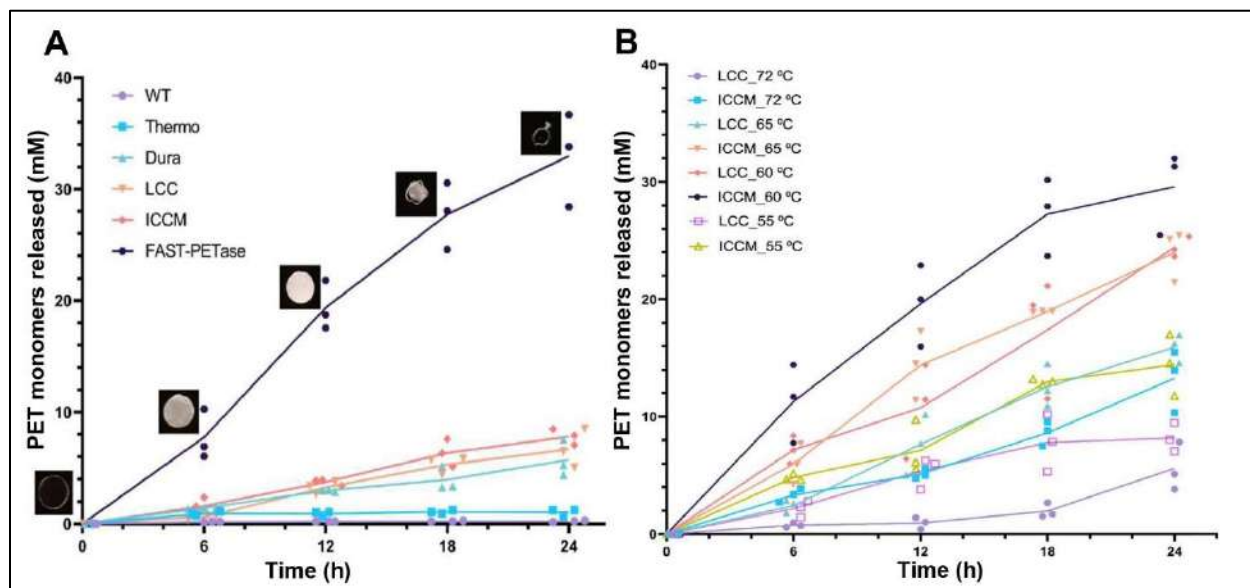


Figure 14. Enzymatic depolymerization of PET by *Is*PETase, LCC and their variants. **A)** Enzymatic activity measured as PET monomers released by *Is*PETase and its variants (ThermoPETase, DuraPETase and FAST-PETase) and LCC and its variant (ICCM) (Tournier et al. 2020) measured at 50 °C. **B)** Enzymatic activity measured as PET monomers released by LCC and ICCM at temperatures of 55, 60, 65 and 72 °C. In contrast to what showed for Tournier et al., the variant ICCM showed more activity at 60 than at 72 °C. The activity of ICCM is similar to that FAST-PETase but at a temperature 10 °C higher. Modified from: Lu et al., 2021.

Since PET is a non-soluble substrate, the rate of degradation is governed by the adsorption of the enzyme to the surface. Another approach to increase the PET hydrolysis rate, apart from the modification of residues of the catalytic site or by increasing its thermal stability and lifetime, is to introduce positive charges in the surface of the enzyme to increase its adsorption to PET polymers. In this regard, a recently discovered metagenomic PET degrading enzyme (PET2) increased its binding rate constant to PET by 2.7 times by introducing Arg and Lys residues in its surface (Nakamura et al. 2021).

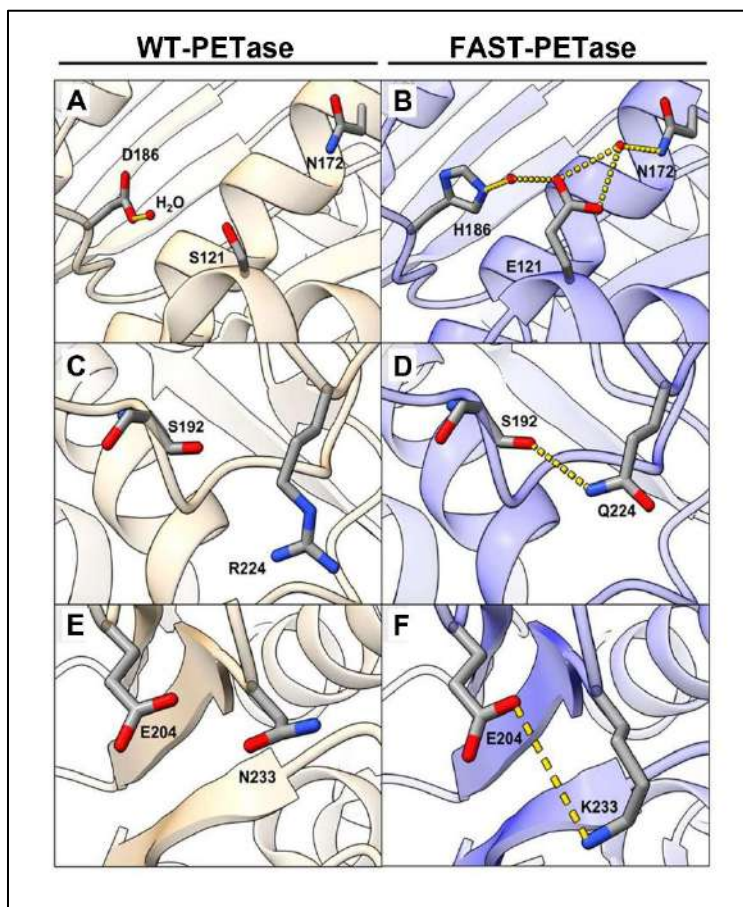


Figure 15. Structures of WT *Is*PETase and FAST-PETase. **A, B)** Mutations D186H and S121E in FAST-PETase create a new water-mediated hydrogen-bonding network with H186 and N172. **C, D)** The change of Arg to Gln creates a hydrogen bond to the side chain of S192. **E, F)** The charged side chain of K233 establishes a saline bridge with E204 in FAST-PETase absent in WT-PETase. Modified from: Lu et al., 2021.

On the other hand, it has also been shown that anionic surfactants are beneficial for the adsorption of the enzyme to the PET film. These molecules have a hydrophobic region that binds to the PET surface and a hydrophilic region that binds to the enzyme, enhancing the enzymatic activity up to 120-fold (**Figure 16**) (Furukawa et al. 2018).

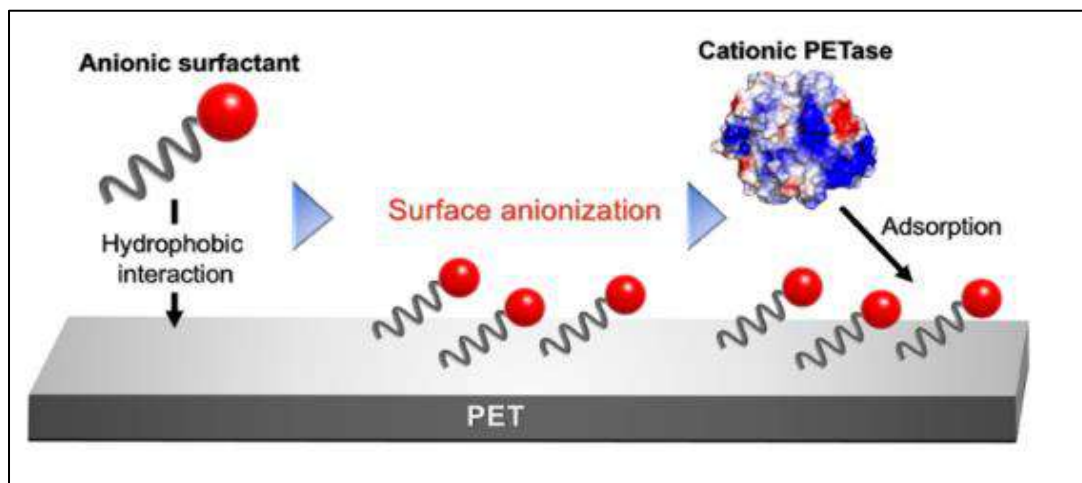


Figure 16. The addition of anionic surfactants to the PET surface increases the absorption of *Is*PETase to the PET film. Incubation of low crystallinity PET with anionic surfactants such as C14-OSO₃⁻ prior improved the enzymatic activity 120-fold (Furukawa et al. 2018).

Classification of PET-degrading enzymes

PET-degrading hydrolases have been categorized into two groups, type I and type II, depending on the aminoacidic composition of their active site, the presence of a disulfide bond near the catalytic pocket, and an enlargement of the connecting loop $\beta 8-\alpha 6$ (Joo et al. 2018). Type I enzymes lack the disulfide bond and the extended loop, while type II enzymes present both features. *Is*PETase and other sequences from mesophilic and thermophilic organisms like *Oleispira antarctica* are classified as type II enzymes, whereas most thermophilic PET hydrolases belong to type I group (Joo et al. 2018).

In this classification of PET hydrolases, based on docking studies with the substrate 2-HE(MHET)₄ and the enzyme *Is*PETase, the active site is divided into two regions, subsite I and II. Subsite I binds one PET subunit (i.e., TPA plus one or two EGs) as observed in crystallized structures (Han et al. 2017; Zeng et al. 2022) while subsite II could bind three MHET molecules through mainly hydrophobic interactions, although there are no crystallized structures to confirm this hypothesis. In subsite I, the residues are highly

conserved among the different polyester hydrolases. In contrast, subsite II presents a variable amino acid composition.

The main differences between type I and II enzymes in subsite II is the presence of a His, at position 159 in *IsPETase*, which is replaced by a Trp in type II enzymes (Joo et al. 2018). Furthermore, type II enzymes can be further divided into type IIa and type IIb, whose main differences in subsite II are a Phe/Tyr at position 238 of *IsPETase* for type IIa enzymes, whereas type IIb enzymes present a Ser. An additional feature of type IIb enzymes is that they have a Thr and an Ala at positions 88 and 89 of *IsPETase* respectively, similarly to type I enzymes (**Figure 17**).

Nevertheless, Wei et al. questioned the binding mode of the docked 2-HE(MHET)₄, arguing that at 30 °C, the ethylene glycol torsion angle Ψ in an amorphous is unlikely to adopt a trans conformation, as it was shown in the docked structure of 2-HE(MHET)₄ (Wei et al. 2019b). Therefore, residues in subsite IIb and IIc would be unlikely to interact with the two MHET moieties of 2-HE(MHET)₄.

Residues in <i>IsPETase</i>	Enzyme catalysis			Subsite I			Subsite II					Extended loop			Additional disulfide bond					
	S160	H237	D206	Y87	Q119	M161	W185	T88	A89	W159	S238	N241	S242	G243	N244	S245	N246	Q247	C203	C239
Type I	S	H	D	Y _F	Q _Y	M	W	TL	A _G	H	F	N _D	T _S _{LMF}	S _{PVTIAE}	N _D	-	-	-	GA	FA
Type IIa	S	H	D	Y _F	Q	M	W	VL	S _L	W	FY	N	G _{TSD}	G _D	Y _{GNS}	P _{STIFLA}	N _{YIS}	N _{EDG}	C	C
Type IIb	S	H	D	Y _F	Q	M	W	T	A	W	S _T	N	S _T	G	N	S	N	Q _A	C	C

Figure 17. Key residues involved in PET catalysis and classification of enzymes based on their aminoacidic composition. Numbering corresponds to *IsPETase* (Joo et al. 2018).

Methods for measuring enzymatic PET hydrolase activity

Existing methods for measuring PET hydrolysis activity are limited and generally tedious as PET is an insoluble substrate. The most common way to measure enzymatic activity is by quantifying the weight loss

of PET sheets or its degradation products. The main problem with gravimetric analysis is that the reaction must be stopped to measure the weight loss of the material, impeding to obtain kinetic data continuously.

Titration methods measure the change in pH of the solution due to the release of PET degradation products, such as TPA and MHET, allowing a real-time monitoring of the hydrolysis reaction. However, some products of the reaction, such as BHET and PET oligomers, cannot be measured. In addition, products with different amounts of carboxyl groups can be produced, such that a molecule with the same number of carbons could have different effects on pH, thus impeding an accurate measurement of the actual amount of product released (Frank et al. 2022). Although BHET, MHET, and TPA can be reliably quantified by reverse-phase HPLC (Pirillo et al. 2021), it is a time-consuming and expensive method.

Optical methods such as turbidimetric assays measure the enzymatic activity as the decrease in turbidity of a suspension of polymer nanoparticles over time. This technique allows a continuous monitoring of the reaction and enables easy quantification of hydrolysis and adsorption kinetic constants (Wei et al. 2014c; Belisário-Ferrari et al. 2019). However, nanoparticles are more amorphous than PET films and have a much higher surface-area ratio, which makes them more susceptible to degradation by enzymes. Thus, it is not possible to extrapolate enzyme activity with nanoparticles to activity with polymer films.

Another optical method consists of measuring TPA release by its modification through a $\text{Fe}_2(\text{SO}_4)$ -catalyzed Fenton reaction into a fluorescent probe, hydroxylphthalic acid (HOTH) (Wei et al. 2012), which can be measured spectrofluorometrically. The limitation of this method is that aliquots of the reaction supernatant must be taken every so often, which does not allow a continuous monitoring of the reaction.

A recently published method uses a different approach to those mentioned above: it measures the changes in impedance of PET films caused by enzymatic degradation. Impedance is the resistance to an electric current and it is modified by the process of enzyme erosion on the material. PET films are placed between two chambers filled with electrolytes and the enzyme solution. The film acts as a resistance to electric current, and this resistance decreases as the film becomes thinner due to enzymatic degradation. As pores

form, ions can pass through the PET film and the impedance drops dramatically. By measuring the changes in impedance from the onset of the enzymatic reaction to pore formation, the degradation kinetics of the polymer can be determined (Frank et al. 2022). This new method allows to determine in real time the enzymatic reaction with PET films, which is really promising, however, it requires a specific device, not yet commercially developed.

Finally, another new method based on FADS (fluorescence-activated droplet sorting in microfluidics) has recently been developed. This is the first high-throughput method developed so far for the hydrolytic activity of PET. In brief, microbes from nature are microencapsulated and each droplet is injected with fluorescein dibenzoate (FDBz), a chemical compound that resembles PET, and when hydrolyzed forms fluorescein that can be detected by fluorescence. Droplets are sorted by their fluorescence signal and the positive ones are isolated and plated on BHET agar plates for further screening and the final selected clones are evaluated for PET degradation by fermentation with PET fibers and observation of surface erosion of PET films. This method can be applied to test enzymatic variants, having an analysis capacity of 1000 droplets per second (Qiao et al. 2022).

Cold-adapted enzymes as potential PET biocatalysts

Since information of PET-degrading enzymes at moderate temperatures is so far very limited, the search for new enzymes in microorganisms adapted to low temperatures is of interest. Such enzymes could constitute templates as good as *IsPETase* for protein engineering campaigns to design better biocatalysts. Only recently, another mesophilic polyester hydrolase has been found in the Gram-negative marine bacterium *Pseudomonas aestusnigri*, isolated from a marine oil spill. This enzyme, classified as type IIa, exhibits hydrolytic activity on amorphous PET at 30 °C, although very limited compared to *IsPETase*. The variants obtained by rational mutagenesis were also able to release low amounts of MHET from bottled PET (Bollinger et al. 2020).

In this regard, recent studies have shown that the presence of plastics in marine environments is ubiquitous, with surface circulation models demonstrating that the abundance of plastics in marine polar environments is similar to that from other ocean and seas in the world (Cózar et al. 2017). Although the polar regions are uninhabited by humans, ocean currents transport the plastic debris from lower latitudes. For example, the floating debris from the North Atlantic Ocean travels to the Greenland and Barents seas where it is retained. As a result, the seafloor beneath these areas may be a sink for plastic debris (Cózar et al. 2017). Moreover, the concentration of plastic items around the Antarctica is estimated to be around 1,800 items/km², equal to that of 70% of the world's oceans.

Microorganisms such as bacteria, microalgae and invertebrates have been found attached to this floating plastic (Lacerda et al. 2019) and some microorganisms have been reported to feed on biodegradable and non-biodegradable polymers as sole carbon sources (Yoshida et al. 2016; Wallace et al. 2020; Meyer-Cifuentes et al. 2020). For example, terrestrial and marine microorganisms have been shown to grow on the biodegradable aliphatic-aromatic polymer poly (butylene adipate co-terephthalate) (PBAT), creating a synergistic relationship in which attached communities released oligomers that were subsequently degraded by unattached communities (Meyer-Cifuentes et al. 2020). Similarly, the bacterium *Ideonella sakaiensis* was able to grow on amorphous PET from commercial food containers or films as a sole carbon source (Wallace et al. 2020). Although an increasing number of organisms feeding on synthetic polymers have been found, it is not yet known whether these microorganisms are evolving to adapt to this new carbon source or whether this phenomenon is due to a broad substrate specificity of their enzymes.

Low temperatures drastically lessen the rate of enzymatic reactions. As a rule, a reduction of temperature of 10 °C decreases enzyme activity by 2 to 4-fold (Feller and Gerday 2003). Cold-adapted enzymes face the lack of thermal energy in the surroundings by incorporating structure and sequence features that allow them to maintain catalytic constants up to 10 times higher than their homologues at low temperatures (Feller and Gerday 2003). Following the Arrhenius equation that relates catalytic activity with temperature

(equation 10), cold-adapted enzymes decrease their activation energy (E_a) to compensate for the detrimental effect of the decrease in ambient temperature on the catalytic rate (k_{cat}) of the enzyme.

$$k_{cat} = Ae^{-E_a/(RT)} \quad (10)$$

Thus, the amount of energy they need to reach the transition state during the enzymatic reaction is lower (**Figure 18**). The decrease in the activation energy is achieved by reducing the enthalpy, i.e., reducing the number interaction between the enzyme and the substrate, and by increasing the entropy, i.e., making the catalytic pocket more flexible. The reduction in enthalpy also leads to substrate promiscuity, as the reduction of active site interactions makes enzymes less substrate-specific (Santiago et al. 2016).

Two main mechanisms of cold adaptation related to flexibility have been proposed: enzymes could have evolved towards the lowest possible stability of their native state or only some localized regions of the enzyme could have acquired greater flexibility (Papaleo et al. 2012). Consistently, cold-adapted enzymes exhibit either an increment of flexibility in localized regions near the active site (local flexibility) or in the whole structure (global flexibility). In many cases, only the active site presents a high structural flexibility, while the other regions not involved in catalysis keep their stiffness. This phenomenon partly explains why psychrophilic enzymes often exhibit a temperature of inactivation below the T_m (Feller and Gerday 2003).

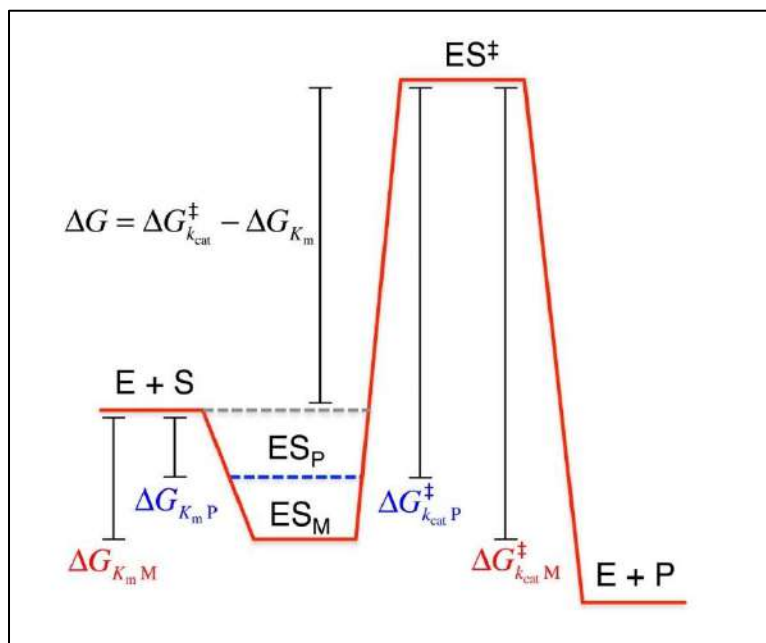


Figure 18. Diagram of energy for the enzymatic catalysis from substrates (S) to products (P) according to the transition state theory. The difference in energy of the enzyme-substrate complex is lower for the psychrophilic enzyme (ES_P) than for the mesophilic enzyme (ES_M) (Santiago et al. 2016).

There are several molecular mechanisms by which cold-adapted enzymes increase their structural flexibility. One of them is to displace the water molecules from the binding pocket when the substrate-complex is bound, which increases the entropy (Siddiqui 2017). It has also been observed that a reduction in the number of arginines and prolines is beneficial since these residues create multiple hydrogen bonds and salt bridges. Other similar mechanism consists of increasing the presence of asparagines, methionines and glycines, as well as aminoacids with small and neutral side chains. It has also been shown that lengthening of the loops, as well as an increased presence of hydrophobic residues exposed to the solvent, increases flexibility (De Maayer et al. 2014).

Regarding the interactions between the substrate and the active site, these are lower and weaker in cold-adapted enzymes when compared to their mesophilic homologs, which implies an increase in the K_M .

However, some cold-adapted enzymes can overcome this reduction in affinity by changing some residues in the binding pocket. As an example, a psychrophilic chitinase changes the hydrophobic interactions from its mesophilic counterpart for electrostatic interactions that are more stable at lower temperatures (Lonhienne et al. 2001). Increased flexibility generally leads to a reduction on structural stability. As a result, inactivation rates of cold-adapted enzymes are faster compared to the mesophilic counterparts (D'Amico et al. 2003) (**Figure 19**).

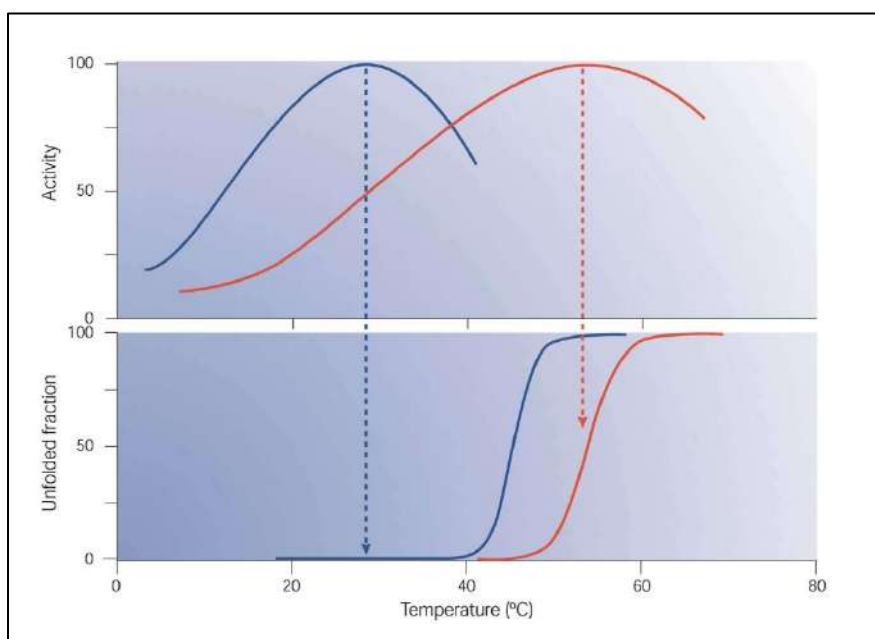


Figure 19. Temperatures of activity and unfolding of mesophilic and psychrophilic enzymes. Psychrophilic enzymes (blue) lose activity before their thermal denaturation occurs because of the heat-lability of their active-site. On the contrary, for mesophilic enzymes (red), the loss of activity corresponds to protein denaturation (Feller and Gerday 2003).

The most common strategy to study psychrophilic enzymes is by heterologous expression in mesophilic organisms. The genes can be either extracted from the genome of the microorganism by PCR or synthesized with the optimal codons for the host, if this genomic material is not available, and cloned into an expression

vector. The most common expression vectors used for cold-adapted enzymes are the commercially available pET plasmids, which enable recombinant protein production on *E. coli* strains such as BL21(DE3), the most widely used microorganism for this purpose. It is worth noting that there are other alternatives of vectors and hosts specially designed for expression of psychrophilic enzymes, such as the pCold vector and the ArcticExpress strain, but their use is not widespread (Santiago et al. 2016). The temperature at which these mesophilic microorganisms are grown is often below its optimum growth temperature to allow proper enzyme folding (Santiago et al. 2016). Regarding the purification process, most of the studies with cold-adapted enzymes used histidine tags for immobilized metal affinity chromatography and were extracted from the cytoplasm in a soluble form (Santiago et al. 2016).

Experimental and computational methods to assess the structural flexibility of cold-adapted enzymes.

Several experimental methods can be used to study the structural stability and flexibility of cold-adapted enzymes. One of the most common experimental methods is to measure the dynamic quenching of tryptophan fluorescence at increasing acrylamide concentrations. When acrylamide encounters a tryptophan residue, its fluorescence decays. Thus, this technique measures the rate of acrylamide diffusion into the protein, which is related to the dynamic fluctuations in the protein structure (Eftink and Ghiron 1975).

Another popular strategy is the use of amide backbone hydrogen/deuterium exchange measured by mass spectrometry. In this technique, the hydrogen atoms of the protein are replaced by the deuterium atoms of the solvent. The accessibility of the protein structure by the solvent molecules is measured by the rate of exchange of hydrogen for deuterium. To localize the regions in the protein where the deuterium exchange took place, the protein is quenched and digested by pepsin and the resultant peptides are measured by mass spectrometry (Zhang and Smith 1993).

Although these methods provide valuable information on structural flexibility, they require expensive infrastructure that is often difficult to access. In this regard, there are computational methods for studying structural flexibility that require less infrastructure and cost. Molecular dynamics (MD) simulations are a widespread computational approach that apply Newton's equations of motion to evaluate the local and global dynamic features of a protein with atomistic resolution (Noel and Onuchic 2012). To accurately model the interactions between these particles it is necessary to have a precise description of the potential energy or force field that governs their behavior (Grigoriev et al. 2008). Typically, these force fields are parameterized based on empirical data and include the effects of explicit solvent (Noel and Onuchic 2012). The procedure of a typical MD simulation is as follows: at each step of the process, the forces on the atoms, which are assumed to be constant over the time interval, are calculated and combined with their current positions and velocities to generate new positions and velocities. The atoms are moved to their new positions, the updated set of forces is calculated, and a new cycle of dynamics is initiated. This process is repeated many times, allowing the system to evolve over time and providing information about the behavior of the atoms at each step. Thus, by numerically integrating Hamilton's equations over time, a molecular trajectory is generated, which can be used to study the kinetic and thermodynamic properties of the system (Grigoriev et al. 2008).

Using MD simulations, it is possible to calculate the actual dynamics of a system and to determine the time-averaged properties of the system from these calculations (Grigoriev et al. 2008). Moreover, by analyzing the microscopic data obtained from molecular dynamics simulations, it is possible to make predictions about the macroscopic properties, such as pressure, temperature, or heat capacity, and to understand how these properties emerge from the behavior of individual particles (Grigoriev et al. 2008).

Accurate prediction of thermodynamic properties of solute molecules requires an appropriate representation of the solvent. Nevertheless, solvent models can be either explicit, in which the solvent is treated as a collection of individual particles, or implicit, in which the solvent is described using analytical models that

treat it as a continuous medium. The latter reduces the number of interacting particles and degrees of freedom in the system, making the calculations more efficient (Zhang et al. 2017).

To ensure the accuracy of molecular dynamics simulations, the time span simulated should be large enough to capture the kinetics of the process. The time scales of the vibrations of the system can vary from femtoseconds (bond vibrations) or picoseconds (collective vibrations) to milliseconds (protein folding). The integration time step should be determined by the most rapidly varying force, being of the order of femtoseconds (Grigoriev et al. 2008).

Multiple simulations are often produced, and the Root Mean-Square Deviation (RMSD) metric is employed to determine the reproducibility of the simulations. To assess protein dynamics and local structural flexibility, the per-residue Root Mean-Square Fluctuation (RMSF) index measures the amplitude of the fluctuations of each residue with respect to the average structure (Papaleo et al. 2012). Cautions must be taken with MD simulations of cold-adapted enzymes, as studies have shown that secondary structure motions are reproducible between different simulation replicates, but loop motions were more stochastic. This limitation can be overcome by increasing the simulation time and the number of independent trajectories performed, thus widening the conformational sampling (Papaleo et al. 2012).

Experimental and computational methods to assess the interactions between an enzyme and its substrate

In contrast to the vast diversity of computational and experimental strategies to study local structural flexibility in proteins, only a few approaches enable identification of the interactions between an enzyme and its substrate. A typical experimental effort corresponds to crystallization of the enzyme in the presence of a substrate, a product, or an analog, obtaining the bound complex after structure solution. However, as aforementioned, a specific challenge with cold-adapted enzymes is the increase in structural flexibility of the active site and the reduction and weakening of the interactions with the substrate (Lonhienne et al. 2001), which is detrimental for solving these regions by X-ray diffraction due to their high mobility even

in the crystalline condition. Moreover, crystallization assays in the presence of substrate analogs do not secure the observation of the electronic density of these moieties during structure solution and refinement.

An alternative to obtain the substrate-bound complex of an enzyme is the use of molecular docking, a computational technique used to predict the preferred orientation of a small molecule (ligand) when binding to a larger molecule (receptor). This process involves sampling various conformations and orientations of the ligand within the receptor binding site and using a scoring function to select the best conformation, orientation, and translation of the ligand (poses). The goal of molecular docking is to accurately predict the structure of the ligand when it binds to the receptor and its binding affinity. Different docking programs can vary in their computational approaches to conduct ligand placement, conformational space scanning, and binding scoring (Pérez and Tvaroška 2014). Regardless, all docking programs calculate the binding energy of the different poses by counting the number of favorable intermolecular interactions such as hydrogen bonds and hydrophobic contacts, and the different poses are ranked based on their predicted affinities with the protein (Roy et al. 2015).

Correct identification of the active site of an enzyme and validation of the appropriate placement of the substrate is crucial, as it can significantly affect the accuracy of docking simulations and subsequent experiments based on these results. In general, docking programs have robust algorithms that enable to identify the active site of a given enzyme by binding the ligand on different parts of the protein and exploring the best possible binding position (Roy et al. 2015). However, the most appropriate sources for validation of the active site of an enzyme and the appropriate binding pose of the substrate are biochemical experiments readily available in the literature (e.g., site-directed mutations that describe enzymatic activity loss) or solved crystal structures of homologous enzymes with similar ligands.

One of the biggest challenges in molecular docking is to address the flexibility of proteins due to their large size and many degrees of freedom. Depending on this, four types of docking can be distinguished:

- **Soft docking:** In soft docking, the protein and ligand are treated as flexible structures that can move and adapt to each other during the docking process (Pérez and Tvaroška 2014).
- **Side-chain flexibility:** This method allows side-chain mobility while keeping backbone mobility restricted. To explore the conformational space of side chains, it uses side-chain rotamer libraries that are subsequently subjected to optimization during the ligand docking procedure (Pérez and Tvaroška 2014).
- **Molecular relaxation:** This method places the ligand into the binding site and then relaxes the protein backbone and side chains nearby. The goal of the method is to find the binding orientation that minimizes the energy of the protein-ligand complex. This is typically done using energy minimization techniques, such as steepest descent or conjugate gradient methods, which involve iteratively adjusting the positions of the atoms in the protein and ligand to minimize the energy (Pérez and Tvaroška 2014).
- **Protein ensemble docking:** Protein ensemble docking is a method that involves using multiple conformations or models of the protein, rather than a single static structure, in the docking process. These different conformations, in turn, are obtained via MD simulations. The idea behind this approach is that a protein can have multiple conformations in its native state, and these conformations can be relevant for ligand binding. By considering multiple conformations of the protein, the docking process can explore different binding orientations and improve the accuracy of the predictions (Pérez and Tvaroška 2014).

To generate all the possible ligand conformations within the active site of the protein, different algorithms exist. One of them is the shape matching algorithm, based on the idea of shape complementarity, meaning that the shapes of the ligand and protein binding site should fit well together to form a stable complex. The ligand is placed in the protein binding site, using as criterion that the molecular surface of the ligand should harmonize with the molecular surface of the binding site. The ligand is allowed to explore different binding

orientations by allowing for three translational and three rotational degrees of freedom, while its conformation is typically fixed during this process. The shape matching algorithm is generally considered to be computationally efficient as it only requires a single conformation of the ligand and does not involve energy minimization or other computationally intensive processes (Roy et al. 2015).

Another algorithm is the systematic search, used for flexible ligand docking to explore all possible binding orientations of the ligand by considering all degrees of freedom of the ligand. A subtype of this algorithm is the "exhaustive search", whereby all possible rotations of the ligand bonds are tested. Another subtype is the "fragment approach" whereby the ligand is fragmented and the binding of these fragments is tested separately, connecting them back in the final steps (Roy et al. 2015).

Finally, the stochastic algorithm involves sampling ligand-binding orientations and conformations by making random changes to the ligand conformation, translational, and rotational positions. These changes are then accepted or rejected based on a probabilistic criterion. This method is based on the idea that by making random changes to the ligand conformation and position, it is possible to explore a large number of possible binding orientations and find the one with the highest affinity for the protein (Roy et al. 2015).

There are different types of stochastic methods, with the Monte Carlo algorithm being used in this work, which uses the Boltzmann probability function to allow a random change. First, the ligand is placed in a random position and orientation into the binding site of the protein, excluding the conformations in which the protein backbone and the ligand non-hydrogen atoms clash. Secondly, an energetic minimization is carried out, including small perturbations of the ligand pose, side-chain repacking, and gradient minimization. Depending on the size of the ligand, the size of the conformational ligand ensemble, and the binding site, this cycle can be repeated between 1,000 and 5,000 times (Meiler and Baker 2006).

To achieve better quality docking, in many cases, it is necessary to add distance restrictions, especially on key catalytic residues. With these constraints, one can control the way in which poses are generated by discarding those that are not likely to be catalytically active (Roy et al. 2015).

One of the key factors in determining the accuracy of a protein-ligand docking algorithm is the scoring function used during the docking analysis. An ideal scoring function should be both fast and accurate. There have been numerous scoring functions developed for use in docking studies, which can be broadly classified into different categories, some of the most popular ones are: force field, empirical and knowledge-based consensus scoring functions (Roy et al. 2015).

Force field scoring functions are widely used and is the scoring function used in this work. They are based on partitioning the ligand binding energy into individual components, such as electrostatic energies, van der Waals energies, and bond stretching, bending, and torsional energies. One of the main challenges of these scoring functions is to accurately account for solvent and entropy effects (Roy et al. 2015).

Empirical scoring functions consist of the sum of weighted energy terms, such as Van der Waals energy, electrostatic energy, hydrogen bonding energy, desolvation term, entropy term and hydrophobicity term. Compared to scoring functions based on force fields, empirical scoring functions are usually more computationally efficient because their energy terms are simpler. However, the accuracy of an empirical scoring function depends on the quality of the training set used to develop it (Roy et al. 2015).

Lastly, knowledge-based scoring functions are based on the analysis of a large number of known protein-ligand complexes, and they use this information to predict the affinity between a particular protein and a particular ligand using the Boltzmann law to convert atom pair preferences into distance-dependent pairwise potentials (Shen et al. 2011).

Hypothesis and objectives

PET consists of carbon chains with aromatic units linked by intermolecular forces. In their crystalline state, PET chains are structured in lamellas, tightly packed structures that are inaccessible to enzymes. Very high temperatures are required to break the intermolecular bonds between the chains. However, PET can also be found in an amorphous state, where the polymer chains are not distributed in a particular way and are more mobile and flexible. The glass transition temperature, which only applies to amorphous polymers, is the temperature at which the polymer changes from a glassy to a rubbery state (Qin 2016). At this point, the volume of the material and the mobility of the polymer chains increase. In the case of PET, this temperature is around 65 °C, which can vary slightly in the presence of water, buffer, etc. Since the mobility of polymer chains increases with temperature, temperatures above T_g will make PET more accessible to enzymes possible (Marten et al. 2003). However, not many enzymes can withstand such high temperatures. In addition, it is more desirable that future enzyme recycling processes can operate at room temperature to be more environmentally friendly and economical.

So far, there is little information on PET hydrolases active at moderate temperatures. Only two enzymes have been reported so far to degrade PET below the T_g : *IsPETase* and PE-H (Yoshida et al. 2016; Bollinger et al. 2020). *IsPETase* has higher activity than LCC at low temperatures, however, this activity remains very low compared to the activity of these enzymes at 60 °C and 70 °C. Nevertheless, a modification of 5 residues in *IsPETase* has resulted in a variant that is as active at 50 °C as LCC at 65 °C (Lu et al. 2021). This raises the question of whether it is possible to increase the activity of the mesophilic and psychrophilic enzymes to levels comparable to those of thermophilic enzymes, but at lower temperatures. The question is then what is the lowest temperature at which high enzyme activity can be obtained. That is, what is the temperature at which we can compensate for the rigidity of the polymer to achieve high activity.

In this regard, it has been shown that low-temperature adapted enzymes have a more flexible active site than their mesophilic and thermophilic counterparts (Feller and Gerday 2003). Also, plastics have been

mobilized through the ocean currents towards polar marine environments, inhabited by a diversity of microorganisms that thrive in these cold temperature conditions. Therefore, the hypothesis of this research is as follows:

Hypothesis

Antarctica is a source of cold-adapted PET hydrolase-like enzymes, in which the intrinsic flexibility of their active site can compensate for the rigidity of PET and enable its hydrolysis at temperatures below its T_g .

General objective

The general objective of this thesis is to identify and biochemically characterize putative cold-active PET hydrolases from Antarctic bacteria, and to improve the activity of the best candidate via rational protein engineering of its active site and explore the activity-stability tradeoffs of these engineered enzymes.

Specific objectives

1. To evaluate the polyesterase activity against PCL and PET and the thermostability of putative cold-active PET hydrolases from Antarctic bacteria found in protein sequence databases.
2. To determine the three-dimensional structure of the best candidate by X-ray crystallography and/or homology modelling.
3. To improve the catalytic activity against PET of the best enzyme by creating variants by rational protein engineering.
4. To study the structural flexibility of the best enzyme by molecular dynamic simulations.

CHAPTER II.
METHODOLOGY

Bioinformatic identification of OaCut and Mors1

A BLAST (Zhang 1998) search against the UniProt Knowledgebase (Magrane and Consortium 2011) was performed using the amino acid sequence of *Is*PETase (UniProtKB A0A0K8P6T7) as a query, identifying the sequences of OaCut (UniProtKB R4YKL9, 53% sequence identity) and Mors1 (UniProtKB P19833, 45% sequence identity) (**Supplementary Table 1**). These protein sequences were analyzed using the SignalP v5.0 server (Almagro Armenteros et al. 2019) for identification of signal peptides for extracellular export that are present in all known bacterial cutinases (Chen et al. 2008) and that are truncated from these enzymes for biochemical characterizations (Fecker et al. 2018). Disordered regions in the secondary structure were identified by PrDOS server (Ishida and Kinoshita 2007).

Protein expression and purification

Genes encoding truncated Mors1 (residues 59-319) and OaCut (residues 47-310) were synthesized (Genscript, Piscataway, NJ, USA), cloned into a pET28a vector (EMD Biosciences, Madison, WI, USA) as NdeI/BamHI fragments and transformed into *Escherichia coli* BL21(DE3). The bacteria were grown in Terrific Broth medium (Thermo Fisher Scientific, Waltham, MA, USA) supplemented with 37 µg/ml kanamycin at 37 °C with vigorous shaking. Upon reaching an optical density at 600 nm (OD₆₀₀) of 0.8, protein expression was induced using 1 mM isopropyl β-D-1-thiogalactopyranoside (IPTG) and the bacterial culture was further grown for 16 hours at 14 °C. Cells were harvested by centrifugation (3,200 xg, 4 °C, 30 min) and then lysed by sonication in buffer containing 20 mM HEPES pH 7.5, 20 mM imidazole, 500 mM NaCl, and 8 M urea. Afterwards, this buffer was changed to 50 mM sodium phosphate pH 8.0, 20 mM imidazole, 200 mM NaCl and 8 M urea. A cleared lysate was collected by centrifugation (24000 x g, 4 °C, 60 min), filtered and loaded onto a Ni-Sepharose resin (HisTrap™ FF crude, GE Healthcare Life Sciences, Pittsburgh, PA, USA). His-tagged protein was eluted using the same buffer supplemented with 350 mM imidazole and then dialyzed overnight at 4 °C in a buffer containing 20 mM HEPES pH 7.5, 75 mM 200 mM NaCl, 200 mM arginine. This buffer was later changed to 50 mM sodium phosphate pH 8.0,

200 mM NaCl and 200 mM arginine. Refolded protein was finally loaded onto a HiLoad Superdex 200 prep grade size-exclusion chromatography (SEC) column (GE Healthcare Life Sciences) using an ÄKTA pure FPLC (GE Healthcare Life Sciences) and eluted in buffer containing 20 mM HEPES pH 7.5 and 75 mM NaCl. This buffer was further modified to 50 mM sodium phosphate pH 8.0 and 200 mM NaCl. The purity of the preparations was confirmed by sodium dodecyl sulfate-polyacrylamide gel electrophoresis (SDS-PAGE). Protein concentration was determined by the Bradford assay (Bradford 1976), ROTI®Quant (Carl Roth GmbH + Co. KG, Karlsruhe, Germany), following the instructions on the supplier's manual. Bovine serum albumin (BSA) was used as standard for calibration of the Bradford assay.

Cloning and mutagenesis

Single-point variants of Mors1 gene were generated by polymerase chain reaction (PCR). For every reaction, the following mixture was used: 0.2 µl Phusion DNA polymerase (2 U/ µl) (Thermo Scientific, Waltham, MA, USA), 0.4 µl dNTP mix (10 mM), 1 µl plasmid template (50-100 ng/µl), 2 µl primers (100 µM) (**Supplementary Table 2**), 4 µl 5x Phusion buffer and 12.4 µl of water, for a total volume of 20 µl. The PCR program used is shown in **Supplementary Table 3**.

The PCR products were treated with DpnI to eliminate the parental plasmid. To do this, 10 µl of the PCR products were incubated with 0.4 µl of DpnI (New England Biolabs GmbH, Germany) at 37 °C for 90 min and then at 80 °C for 20 min. Then, the products were transformed into XL10-Gold® ultracompetent *E. coli* cells (Agilent Technologies, Santa Clara, CA, USA). Cells were plated out into agar plates with kanamycin. Plasmids were extracted from the positive colonies using the Monarch Plasmid Miniprep Kit (New England Biolabs GmbH, Germany).

For the construction of a chimeric Mors1-LCC, a flexible loop of the active site of Mors1 (residues 262-276) was replaced by the shorter loop of LCC (residues 203-215). The determination of this region was based on the comparison of the solved structure of LCC (PDB 4EB0) and the modelled structure of Mors1

generated in this work. The chimeric sequence was termed CM (Chimeric Mors1) (**Supplementary Table 1**). The sequence was synthesized (Genscript, Piscataway, NJ, USA), and cloned into a pET28a vector (EMD Biosciences, Madison, WI, USA) between the restriction sites NdeI and BamHI.

Sodium dodecyl sulfate -polyacrylamide gel electrophoresis (SDS-PAGE)

The purity of the enzymatic samples was tested in a 15% polyacrylamide gel (Tris-glycine buffer). Samples were loaded under reducing conditions. A pre-stained molecular marker (PS10 PLUS;11-180 kDa, Gene On, Ludwigshafen, Germany) was used as protein ladder for molecular weight evaluation. Staining was performed with Coomassie Brilliant Blue G-250 (Sigma-Aldrich, San Luis, MO, USA).

Thermal stability of OaCut and Mors1

The apparent melting temperature (T_m) of OaCut and Mors1 was determined using nano-differential scanning fluorimetry (nanoDSF). This technique measures the changes in fluorescence at 330 nm and 350 nm of the tryptophans of the protein as a function of an increase in temperature. In general, tryptophans are in the hydrophobic core of the protein and become exposed to the hydrophilic solvent when the protein denatures. The exposition of the tryptophans to the solvent causes a change of their fluorescence properties towards higher wavelengths in what is called “red shifting” (Ghisaidoobe and Chung 2014). The fluorescence signal at 350 nm barely changes, thus is rather linear, while at 330 nm the fluorescence intensity decreases drastically. The ratio of the 350 nm signal by the 330 nm signal leads to an inversion of the progression curve as a function of temperature. The first derivative of this curve gives a peak, when the slope is maximum, which corresponds to the T_m .

To analyze the samples, a thin glass capillary was filled with purified Mors1 and OaCut at a concentration of around 150 $\mu\text{g/ml}$ in 20 mM HEPES pH 7.5, 70 mM NaCl, and heated from 20 $^{\circ}\text{C}$ to 95 $^{\circ}\text{C}$ at a rate of 1 $^{\circ}\text{C/min}$ (nanoDSF, Prometheus NT.48, Nanotemper Technologies, Munich, Germany). The intrinsic

fluorescence emission of tryptophan residues was monitored at 330 and 350 nm, and the first derivative of the ratio of fluorescence at 330 and 350 nm was calculated to obtain the apparent T_m .

X-ray Crystallography

SEC-purified OaCut was concentrated by ultrafiltration and subjected to different crystallization conditions by the technique “sitting drop vapor diffusion crystallization” at 4 °C using commercial crystallization screening kits: Classics I, Classics II MPD, Anions and Pact Premier (NeXtal Biotech, USA). Crystals obtained were cryoprotected in a reservoir solution containing 20% glycerol and frozen in liquid N₂. The crystals were exposed to an X-ray beam using a Rigaku Micromax-003 X-ray source (Rigaku Americas, The Woodlands, TX) and a Dectris Pilatus 200K detector (Dectris, Baden-Dättwil, Switzerland). Assays were first performed with the truncated version of OaCut (residues 47-310). Due to lack of success in obtaining protein crystals, the full sequence without the signal peptide was also submitted to crystallization, termed as NSP (no signal peptide). Moreover, with the aim of co-crystallizing the enzyme with the substrate TPA, an inactive variant was created where the catalytic Ser was mutated to Ala (S148A).

PCL nanoparticle suspension preparation

To prepare PCL nanoparticles, 250 mg of poly- ϵ -caprolactone (PCL) (Sigma-Aldrich, San Luis, MO, USA) were dissolved in 10 ml acetone at 50 °C. The solution was poured into 100 ml of water under strong stirring and then filtered with a paper filter. To evaporate the acetone, the solution was incubated overnight at 50 °C. To quantify the concentration of PCL, three aliquots of 1 ml were centrifuged, the supernatants were removed, the pellets were dried overnight and weighted. The concentration was calculated as the mean of the three pellets in mg per ml.

PCL plate clearing assays

Plate clearing assays were performed to preliminary test if OaCut and Mors1 degraded PCL (Belisário-Ferrari et al. 2018). The formation of a clearing zone around colonies was used to indicate a PCL-

hydrolyzing activity (Danso et al. 2018). For the preparation of PCL agar plates, a nanoparticle suspension of PCL was added to autoclaved LB-agar (6% v/v) at 60 °C under stirring. Then, 0.5 mM IPTG and 37 µg/ml kanamycin were added before pouring the mixture into Petri dishes. After cooling, recombinant *E. coli* cells harboring the pET28a-OaCut and pET28a-Mors1 plasmids were inoculated onto the plates and incubated at room temperature up to 4 days.

Determination of optimum reaction temperature and buffer conditions for PCL hydrolysis by Mors1

To determine optimum reaction temperature and buffer conditions for the polyesterase activity of Mors1, the decrease in turbidity of a PCL nanoparticle suspension due to enzymatic hydrolysis was monitored at 600 nm as previously described (Wei et al. 2014a; Wei et al. 2014b). The reaction mixtures contained buffer and purified Mors1 (4.0 µg/ml) in a total volume of 200 µl. The reaction was started by the addition of 0.07 mg/ml PCL nanoparticle suspension. Initial hydrolysis rates were determined from the slope of the linear part of the graphs of decreasing OD₆₀₀ over time.

To determine the optimum reaction temperature for the hydrolysis of PCL, initial hydrolysis rates were measured at reaction temperatures between 5 °C and 35 °C in 20 mM HEPES pH 7.5 every 6 seconds using a Cary 60 UV-Vis spectrophotometer (Agilent Technologies, Santa Clara, CA, USA).

To determine the optimum NaCl concentration for the hydrolysis of PCL, hydrolysis rates were measured in 20 mM HEPES pH 7.5 buffer supplemented with NaCl in concentrations of 100, 200, and 500 mM. PCL hydrolysis rates were determined after 1, 3 and 24 h of incubation at 25 °C. The enzyme activity determined after 1 h of incubation in 20 mM HEPES pH 7.5 buffer was set to 100%.

The half-inactivation temperature of Mors1 (T_{50}), i.e., the temperature at which the enzyme activity was reduced by 50% in relation to its activity at 25 °C, was determined by incubating 3.0 µg/ml Mors1 for 15 min in 125 mM sodium phosphate buffer pH 8.0, 200 mM NaCl, at temperatures from 20 °C to 80 °C. The

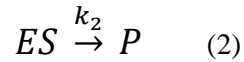
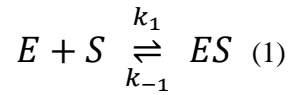
residual activity was determined at 25 °C by measuring the hydrolysis rates of PCL nanoparticles. Data was fitted to a sigmoidal Boltzmann regression curve, with the inflection point corresponding to the T_{50} value.

The effect of five buffers (sodium phosphate, Bis-Tris, HEPES, Tris and potassium phosphate) at pH 7.0 and 8.0 (Tris also at pH 9.0) on the hydrolysis of PCL nanoparticles by Mors1 was compared by reacting 4.0 $\mu\text{g/ml}$ Mors1 with 0.07 mg/ml PCL nanoparticles in 125 mM of the corresponding buffer supplemented with 200 mM NaCl for 1, 3, and 72 h at 25 °C. Hydrolysis rates determined after 1 h in 20 mM HEPES pH 7.5, 200 mM NaCl was set to 100%. All the experiments were performed in triplicates.

Kinetic model for polymer nanoparticle hydrolysis and determination of the kinetic constants of Mors1

Enzymatic degradation of polymers is an erosion process whereby enzymes attach to the surface and hydrolyze the ester bonds of the surface. The bonds inside the polymer are inaccessible until the upper layers have been degraded. For this reason, the reaction in its early stages is considered to occur under conditions of enzyme saturation and substrate limitation. The kinetic model used to describe this mechanism is the inverse of the Michaelis-Menten model, which is based on the derivative of the Langmuir adsorption isotherm. Thus, the reaction rate is limited by the surface area of the polymer (Ronkvist et al. 2009).

Mukai et al. first proposed a heterogeneous model for the hydrolysis of poly(β -hydroxybutyrate) (PHB) (Mukai et al. 1993) that was further modified by Timmins and Lenz (Timmins et al. 1997), and later by Scandola et al. creating a two-step kinetic model (Scandola et al. 1998). Mukai's model considers that when the enzyme binds to the substrate, it occupies a space that is no longer accessible for degradation. This means that there is a "binding domain" and a "catalytic domain" in which the actual catalysis takes place. According to this model, the rate of hydrolysis increases with the enzyme concentration ($[E]$) until all the surface is covered by enzyme (**Figure 20**). However, this model did not consider the substrate concentration and it was later included by Timmins et al. The latter model of Scandola, is a two-step model that stated that the enzymatic rate is directly proportional to the substrate surface area:



Where E is the enzyme, S is the substrate, ES is the enzyme-substrate complex, P is the product, k_1 is the adsorption constant, k_{-1} is the desorption constant and k_2 is the hydrolysis rate.

In this model the substrate S is understood as the area of the film, and ϑ as the fraction occupied by the ES complex. Therefore, the equilibrium adsorption reaction can be expressed as:

$$k_1[E]A(1 - \vartheta) = k_{-1}A\vartheta \quad (3)$$

Where C_e is the enzyme concentration.

From (3), ϑ can be derived as:

$$\vartheta = K[E]/(1 + K[E]) \quad (4)$$

Where K is the adsorption equilibrium constant ($K = k_1/k_{-1}$).

For equation (2), the rate can be expressed as:

$$V = k_2A\vartheta \quad (5)$$

By substituting ϑ from eq. (4):

$$V = \frac{k_2AK[E]}{1+K[E]} \quad (6)$$

Whose linear form is:

$$A/V = (1/Kk_2)(1/[E]) + 1/k_2 \quad (7)$$

From the representation of equation (7) the hydrolysis rate can be derived from the intercept and the adsorption constant K can be derived from the slope.

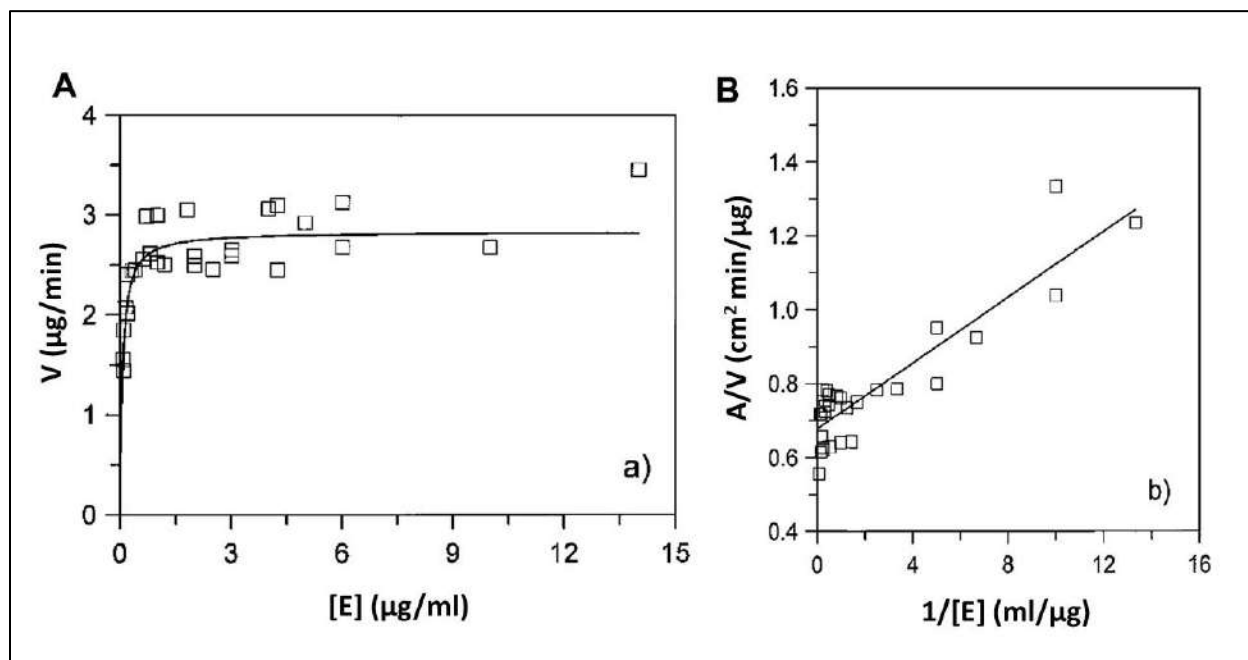


Figure 20. Hydrolysis rate of a polymer film as a function of the enzyme concentration. **A)** Rate (V) of enzymatic hydrolysis of PHB as a function of enzyme concentration ($[E]$). The curve represents the rate calculated according to the model proposed by Scandola (Scandola et al. 1998). **B)** Linear representation of data from a) plotted according to equation 7. Squares are the experimental data and lines are the least-squares fit (Scandola et al. 1998).

Although this model describes the behavior of heterogeneous catalysis of different polyesters, it presents limitations: First, the model considers the entire area of the polymer, however, only the amorphous zones can be degraded, therefore, the area to be considered is smaller, also, the degradation of the surface is not uniform. Second, the model does not take into account that the reaction rates in the amorphous and crystalline areas of the polymer are significantly different (Scandola et al. 1998).

Measuring the enzymatic degradation of a solid substrate by determining the weight loss gravimetrically and quantifying the products by high performing liquid chromatography (HPLC) is time consuming and requires long times of incubation. As an alternative, degradation of polymer particles in suspension is an easier and faster way to compare different enzymes (Wei et al. 2014a). To this regard, Scandola's model was modified to be applied to a polymer suspensions where the enzymatic activity is measured as the decrease in the turbidity of a particle suspension (τ). The velocity of the reaction is measured as the square root of the relation between the turbidity and the initial turbidity:

$$-\frac{d(\sqrt{\tau/\tau_0})}{dt} = \frac{k_\tau K C_e}{1 + K C_e} \quad (8)$$

where τ_0 is the initial turbidity of the suspension of nanoparticles, and k_τ , a relative hydrolysis rate whose relation to the hydrolysis rate k_2 is:

$$k_\tau = 2k_2 \sqrt{\frac{\pi}{A_0}} \quad (9)$$

To determine the kinetic parameters of the PCL hydrolysis reaction catalyzed by Mors1, kinetic assays were performed at 25 °C in a reaction mixture containing 125 mM sodium phosphate pH 8.0, 200 mM NaCl and 0.07 mg/ml PCL nanoparticle suspension with varying enzyme concentrations from 0.6 to 22.0 μ g/ml. Assays were performed in triplicates using 96-well microplates, measuring the change in turbidity at OD₆₀₀ in 10 sec intervals for a total reaction time of 10 min on a Synergy HTX microplate reader (Biotek Instruments Inc, Winooski, VT, USA). Kinetic parameters were determined using equation (8) (Wei et al. 2014a; Wei et al. 2014b). Similar experiments were performed for *Is*PETase.

Turbidimetric quantification of PCL hydrolysis activity of Mors1 variants

The PCL nanoparticle hydrolysis rate for WT Mors1 and several rationally engineered variants was measured on a Synergy HTX microplate reader at the enzyme concentration at which WT Mors1 showed maximum activity (20 µg/ml). Each well contained a reaction mixture comprising 20 µg/ml of the corresponding enzyme in a solution containing 125 mM sodium phosphate pH 8.0, 200 mM NaCl. The reaction was started by the addition of 134 µl of 0.07 mg/ml PCL nanoparticle suspension, corresponding to an initial OD₆₀₀ of 0.8. Measurements were taken every 2 seconds. Negative controls (without enzyme) were also performed. The reaction was carried out at 25 °C. All the measurements were performed in triplicates.

PCL degradation with crude extract

PCL degradation assays were also performed with crude extracts of *E. coli* cells harboring the plasmid encoding Mors1. Enzyme overexpression in 200 ml of *E. coli* C41(DE3) cell grown at 37 °C was induced with 1 mM IPTG after reaching an OD₆₀₀ = 0.8, cultured overnight at 14 °C, and centrifugated. The pellets were resuspended in 100 mM sodium phosphate buffer pH 8.0 and sonicated. After centrifugation, the supernatants were collected and 20 µl of them were placed into a 96 well-plate. To initiate the reaction, the corresponding volume of PCL nanoparticle solution was added to reach an initial OD₆₀₀ of 0.8 and its decrease in turbidity was monitored as previously described. As negative control, a culture of *E. coli* C41(DE3) without recombinant plasmid was used. Also, a non-induced culture was used to check is the plasmid had protein expression leakage in the absence of IPTG. The concentration of proteins in the soluble fraction was measured by the Bradford assay. All the experiments were performed in triplicates.

MHET inhibition assay

To test if the enzyme is inhibited by MHET, the hydrolysis of PCL was measured in the presence of this substrate. Mors1 (4.0 µg/ml) was incubated in 20 mM HEPES pH 7.5, 10 mM MHET. The velocity of the PCL hydrolysis reaction was measured as the decrease in turbidity, as previously described.

Hydrolysis of amorphous PET films by Mors1, OaCut, and IsPETase

Amorphous PET films with a size of 0.5 cm × 3 cm (~45 mg) (250 µm thickness; product number ES301445, Goodfellow, Hamburg, Germany) were washed, weighted, and placed in Eppendorf tubes in a reaction mixture containing 1 M potassium phosphate pH 8.0, 200 mM NaCl and 400 nM of Mors1, 400 nM of OaCut, or 100 nM of IsPETase at 25 °C for 24 h under vigorous shaking. The amount of PET film per microliter of the reaction volume (0.025 mg PET/µl reaction) was identical to what was described for the analysis of IsPETase (Yoshida et al. 2016). The PET films were collected, washed with water, aqueous SDS 0.5 % and ethanol, dried at 50 °C overnight, and their weight loss was determined gravimetrically. Hydrolysis reactions were also performed for 6, 7, and 10 days with 400 nM Mors1 and for 6 days with 400 nM OaCut.

The soluble PET hydrolysis products mono(2-hydroxyethyl) terephthalate (MHET) and terephthalic acid (TPA), present in the supernatants after 24 h of incubation of the PET films with the different enzymes, were analyzed by HPLC using a C18 column (Eurosper II 100-5; 150 x 2 mm with a pre-column, Knauer Wissenschaftliche Geräte GmbH, Berlin, Germany) at a flow rate of 0.3 mL/min on an Agilent 1100 Series HPLC instrument (Agilent Technologies, La Jolla, CA, USA). The mobile phase consisted of acetonitrile with 0.1 % formic acid (A) and 0.1 % formic acid (B). A gradient was performed as follows: 95% B (0.0 min), 80% B (0.1 min), 76% B (3.0 min), 60% B (3.1 min), 0% B (8.0 min), hold for 2 min and back to 95% B (analysis time 12.0 min). The injection volume of the sample was 2 µL and the separated products were detected by their absorbance at 241 nm. TPA (Sigma Aldrich, St. Louis, MO, USA) and MHET was

used as standard. MHET was synthesized as described elsewhere by the hydrolysis of bis(hydroxyethyl) terephthalate (BHET) (Sigma Aldrich, St. Louis, MO, USA) with KOH (Palm et al. 2019). Trimesic acid (TMA) (Sigma Aldrich, St. Louis, MO, USA) was used as internal standard.

Scanning electron microscopy of PET films

PET films fixed on glass substrates were analyzed with a scanning electron microscope (EVO LS10, Carl Zeiss GmbH, Germany) with a LAB6 cathode (Kimball Physics, New Hampshire, USA) and a secondary electron detector. PET films were sputter-coated using a BAL-TEC model SCD 050 (Leica Biosystems, Wetzlar, Germany) with 25 nm gold prior to imaging. Images were captured at an acceleration voltage of 7 kV and a probe current of 5 pA.

Fluorescent dye labeling of free cysteines in Mors1

The presence of free sulfhydryl groups of cysteine residues in Mors1 was determined by covalent labeling with the fluorescent dye 7-fluoro-2,1,3-benzoxadiazole-4-sulfonamide (ABD-F) (Kirley 1989). Both Mors1 and BSA were adjusted to equal molar concentrations and 4 μ L of protein was mixed with 5 μ L of 2x reaction buffer (200 mM H_3BO_3 , 4 mM EDTA, 6% SDS, pH 8.0), 1 μ L of 10x ABD-F (40 mM in DMSO) and incubated for 30 min at 37 °C. Labeled samples were separated on an SDS-PAGE gel under non-reducing conditions and fluorescence was detected in a ChemiDoc XRS+ Gel Imaging System (Bio-Rad Laboratories, Hercules CA, USA). BSA was used as a positive control since it contains 35 cysteines residues that form 17 disulfide bridges and one free cysteine which can be covalently labeled with ABD.

Comparative modelling of Mors1

A comparative model for Mors1 was generated by first selecting high-sequence identity structure templates through a BLAST search against the Protein Data Bank (Berman et al. 2000). The solved crystal structures of IsPETase (PDB 6EQE) (Austin et al. 2018), the cutinases from *Thermobifida cellulositica* (PDB 5LUI) (Ribitsch et al. 2017) and *Thermobifida fusca* (PDB 4CG2) (Roth et al. 2014) and a polyester hydrolase of

Pseudomonas aestusnigri (PDB 6SBN) (Bollinger et al. 2020) were selected. Chain A of each structure was extracted and used as template for the RosettaScripts XML modelling protocol (Bender et al. 2016) to generate a total of 1,000 models, where explicit information about the position of the two conserved disulfide bonds and an additional bond were obtained according to the Cys residues present in the sequence. The lowest-energy model with the lowest RMSD against the template structures was selected and its stereochemical quality was assessed using Verify3D (Lüthy et al. 1992), PROVE (Pontius et al. 1996), PROCHECK (Laskowski et al. 1993) and WHATCHECK (Hoofst et al. 1996). Further refinement of this structure was conducted using two custom relax protocols (Song et al. 2013) with and without restraints on the active site, generating 5,000 additional models that underwent a similar energetical and structural quality assessment.

The five models with lowest-energy and RMSD against the template structure of *IsPETase* (PDB 6EQE) were selected for further analysis (**Supplementary Figure 1**). We did not observe significant differences in the Ramachandran plots for the models 119, 620, 650, 803 and 952. Only 2 amino acids, excluding glycine, were in the non-favored regions, similar to the structure of *IsPETase* who presented one residue in a non-favored region, corresponding to Ser 132. Using Verify3D (Eisenberg et al. 1997), which determines the compatibility of the model with its own primary sequence based on known protein structures, we obtained positive values for all the models, with models 119 and 650 showing the best results. With PROVE, better results were obtained for model 952 with a buried outlier protein atom total of 3.6%. Considering WHATCHECK results, the model 199 showed less errors in comparison to the others and displayed a properly oriented catalytic triad as in the template structures. Model 119 was selected, and 5,000 relaxed models were generated. No improvements were obtained, indicating a good quality of the model 119.

Similarly, a homology model for the CM^{A266C} mutant was constructed using the chain A of the crystal structures of the cutinases *Thermobifida fusca* (PDB 4CG2), Leaf-branch bacterial compost cutinase (PDB

4EB0), *Thermobifida cellulositytica* (PDB 5LUI) and *IsPETase* (PDB 6EQE). The chain A of each crystal structure was extracted and used as a template. The subsequent modelling protocol was the same as the one mentioned above for Mors1. A total of 1,000 initial models were created, from which the model with the lowest energy and lowest RMSD compared to the *IsPETase* structure (PDB 6EQE) was selected (**Supplementary Figure 6**). This structure was subjected to a relaxation protocol, generating 5,000 additional models. From these, the 10 lowest-energy models were selected (**Supplementary Table 5**), selecting model 4549 after a structural and stereochemical analysis similar to WT Mors1.

Molecular dynamics simulations

Molecular dynamics (MD) simulations with Mors1 and *IsPETase* (PDB 6EQE) were carried out using AMBER16 suite along with the ff14SB force field (Maier et al. 2015). The protonation state of the residues at pH 8.0 was estimated using the H⁺ server (Anandakrishnan et al. 2012). Then, the system was solvated with TIP3P water molecules and neutralized with counter ions in a truncated octahedral box of 1.5 nm of padding with periodic boundary conditions. The system was first minimized using a steepest descent method with position restraints on waters and ions, followed by a second minimization without any position restraints. The system was heated from 0 to 298 K for 150 ps at a constant volume using a Langevin thermostat, followed by equilibration of the solvent atoms of each system for 100 ps at 298 K and constant pressure of 1 bar using a Berendsen barostat until density was stable, upon which a third and final equilibration step of the whole system for 100 ps under the same temperature and pressure conditions was performed. Production MD runs were carried out in four replicas for 100 ns each, using a timestep of 2.0 fs alongside the SHAKE (Ryckaert et al. 1977) algorithm and the particle mesh Ewald method (Darden et al. 1993) for long-range electrostatics, with a 10 Å cutoff for short-range electrostatics. Independent runs were ensured by using random seeds for initial velocities during the equilibration step. Replicas were checked for structural convergence using the overall backbone root mean-square deviation (RMSD) from the first frame of the respective trajectory (**Supplementary Figure 3**). Comparison of the differences in local

structural flexibility between *IsPETase* and Mors1 were determined by calculating the per-residue root mean square fluctuations (RMSF). RMSD and RMSF were calculated using CPPTRAJ of AmberTools20 (Roe and Cheatham 2013).

We also performed MD simulations to determine the potential change in structural flexibility on the active site loops of the engineered variants of Mors1 that experimentally showed higher enzymatic activity than the WT enzyme. MD simulations for Mors1 and CM^{A266C} were carried out for a time span of 1 μ s (Gu et al. 2015) using AMBER20 at two different temperatures, 298 and 318 K, following the protocol mentioned above. Replicas were checked for structural convergence using the overall backbone RMSD from the first frame (**Supplementary Figure 3**) and the local flexibility was again analyzed by comparing the per-residue RMSF. Relative frequency of hydrogen bond distance between the γ hydrogen (HG) of S160 and ϵ nitrogen (NE2) of H237, and between the δ oxygen (OD2) of D206 and δ hydrogen (HD1) of H237, were calculated using CPPTRAJ of AmberTools20 (Roe and Cheatham 2013) (

Supplementary Table 7).

Identification of potential PET hydrolases in Antarctic coastal metagenomes

Genes encoding Mors1 homologs were identified from massive sequencing data obtained in 2014 from surface marine waters of Bahía Chile, Antarctica (Alcamán-Arias et al. 2018), available at the NCBI Bioproject no. PRJNA421008. Metagenome readings were filtered using a quality score (Qscore) > 30 and assembled with the SPAdes v3.10.1 software using the "meta" option (Bankevich et al. 2012). The prediction of open reading frames (ORFs) was made from contigs greater than 500 bp with Prodigal v2.6.3 using the "meta" mode and bypassing the Shine-Dalgarno sequence (Hyatt et al. 2010). Lastly, potential polyester hydrolases from the predicted proteins of these metagenomes were identified via local sequence homology analysis against the protein sequence of Mors1 (UniProtKB P19833) using BLASTP (Zhang et al. 1998), with hits having >50% coverage and >70% sequence identity considered valid.

Abundance and taxonomic affiliation of potential metagenomic PET hydrolases

The composition of the bacteria community was evaluated through 16S miTAG analysis, which were obtained and recorded from metagenomes using METAXA2 (Bengtsson-Palme et al. 2015) in metagenomic mode using default parameters. Recruitment of readings to the sequences of potential Mors1 homologs was carried out through the use of Bowtie2 v2.2.6 (Langmead and Salzberg 2012) in the end-to-end alignment mode and allowing 1 mismatch in a seed alignment during multiseed alignment. Then, we identified the possible taxonomic identity of the candidate metagenome sequences through BLASTP (Zhang et al. 1998) against the Refseq_prot database (NCBI, January 2020). Only the best hit was reported, since the first 10 results corresponded to the same taxonomy.

Molecular docking

Molecular docking was performed of a soluble PET substrate analog, 1,2-ethylene-mono-terephthalate-mono(2-hydroxyethyl terephthalate) (EMT) onto the active site of PHL7 and LCC, using Rosetta3 (Leaver-Fay et al. 2011; Lemmon and Meiler 2012). To further analyze the binding mode of the terephthalic ring in the active site of the enzymes, molecular docking of MHET and TPA was also performed.

The conformational diversity of the ligands was represented by creating 277, 52 and 3 conformers for EMT, MHET and TPA, respectively, using the confab package of Open Babel (Boyle et al. 2011). The conformers were generated based on an energy cutoff of 50 kcal mol⁻¹ and an RMSD cutoff of 1.3 Å, 0.4 Å and 0.4 Å for EMT, MHET and TPA, respectively.

For the docking procedure, 40,000 enzyme-substrate and enzyme-product complex structures were generated with a custom Rosetta3 XML script enabling backbone and side-chain flexibility as previously described (Fecker et al. 2018). The top 100 docking poses for all enzyme-ligand pairs were subjected to pairwise ligand RMSD calculation using DockRMSD (Bell and Zhang 2019) to generate a distance matrix for unsupervised exploratory hierarchical clustering analysis. The ligand RMSD matrix was employed to build an euclidean distance matrix using the `dist()` function built in R stats (R Core Team 2020) package and the Ward.D2 method was used to cluster the distance matrix. For visualization of the clustering results, we employed `fviz_cluster` function included in `factoextra` (Kassambara, A. and Mundt 2020) and `ggplot2` (Hadley Wickham 2016).

The cluster that best represented the optimal binding poses of EMT, MHET and TPA into the active sites of PHL7 and LCC was determined by visually assessing that the terephthalic ring of the molecules occupied the same site as the esterase product *p*-nitrophenol (PDB 5XH2) and the MHET analog 1-(2-hydroxyethyl) 4-methyl terephthalate (HEMT, PDB 5XH3) in available crystal structures of a double mutant of *Is*PETase (Han et al. 2017). The lowest binding energy complex for each enzyme-ligand pair was selected along with

four additional complexes with lowest ligand RMSD for decomposition of the per-residue energetic contributions to ligand binding using Rosetta3 DDG mover (Alexander et al. 2013).

CHAPTER III.

RESULTS

III.I Structural and functional characterization of Antarctic hydrolases OaCut and Mors1

The results provided in this sub-chapter are published in the following article:

Blázquez-Sánchez P, Engelberger F, Cifuentes-Anticevic J, Sonnendecker C, Griñén A, Reyes J, Díez B, Guixé V, Richter PK, Zimmermann W, Ramírez-Sarmiento CA (2021) Antarctic polyester hydrolases degrade aliphatic and aromatic polyesters at moderate temperatures. *Appl Environ Microbiol* 1–36 . <https://doi.org/10.1128/aem.01842-21>

Mors1 and OaCut can be expressed in *E. coli* in a non-soluble form

The protein sequences of Mors1 and OaCut were transformed and expressed in *E. coli*. Signal peptides, identified by SignalP server (Almagro Armenteros et al. 2019) were removed. In Mors1 the signal peptide corresponded to residues 1-28 and in OaCut to residues 1-25. Even without the signal peptide, the N-terminal region of Mors1 still had a 29 residue-long region that was absent in the sequence of *IsPETase* and OaCut. We therefore analyzed the presence of disordered regions using the PrDOS server (Ishida and Kinoshita 2007), predicting that residues 46-58 were disordered. Manual comparison of the sequence of Mors1 and OaCut against the truncated sequence and structure of *IsPETase* (PDB 6EQE) showed that, in agreement with the analysis from PrDOS, the α/β hydrolase fold was covered by residues 59-319 in Mors1 and 47-310 in OaCut. We therefore removed the disorder regions prior to expression in *E. coli*.

To test the solubility of the expressed proteins OaCut and Mors1, *E. coli* BL21(DE3) cells were disrupted by sonication and centrifuged, and the presence of each enzyme on pellet and the supernatant was analyzed by SDS-PAGE. For both proteins there was a prominent band in the pellet fraction, indicating that these proteins were expressed in insoluble form, as it was reported previously for *IsPETase* (Fecker et al. 2018). For further purification, denaturing agents such as hydrochloride guanidine (at a final concentration of 6 M) and urea (at a final concentration of 8 M) were used. After IMAC purification, the samples were dialyzed

overnight at 4° C to remove the denaturing agent and refold the enzymes. However, since this process was time-consuming, in the following purifications we omitted this process by directly loading the denatured protein into the SEC column, obtaining the same results. SDS-PAGE of the SEC samples shows a single band approximately at 30 kDa, indicating that the proteins were purified to homogeneity (**Figure 21**).

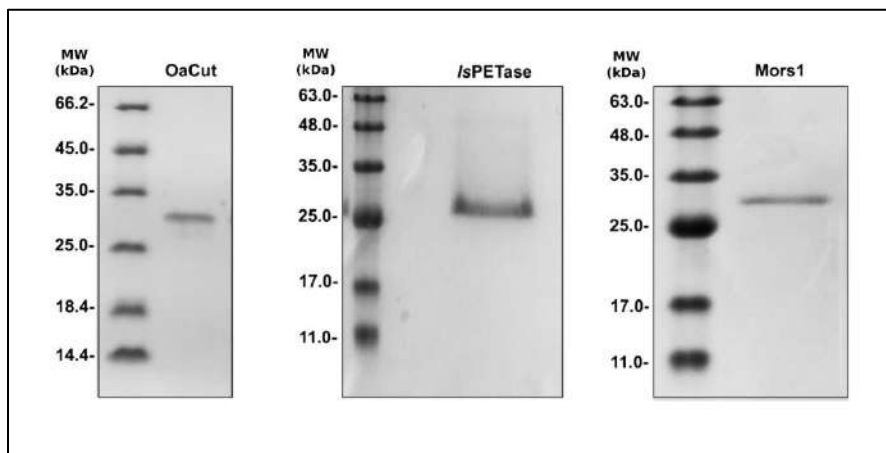


Figure 21. SDS-PAGE of recombinant truncated OaCut (27.8 kDa, 0.5 µg), IsPETase (28.6 kDa, 0.5 µg) and Mors1 (28.6 kDa, 0.5 µg) after purification by affinity and size exclusion chromatography. Proteins were stained with Coomassie Blue. Left lane: molecular weight size marker.

Mors1 and OaCut degrade PCL at moderate temperatures

We analyzed the ability of Mors1 and OaCut to degrade PCL and PET at moderate temperatures. To detect polyester hydrolysis activity of OaCut and Mors1, plate clearing assays were performed with PCL. Overnight incubation at 25 °C resulted in the formation of clearing zones around *E. coli* colonies overexpressing Mors1 and OaCut in plates containing PCL (**Figure 22 A, B**).

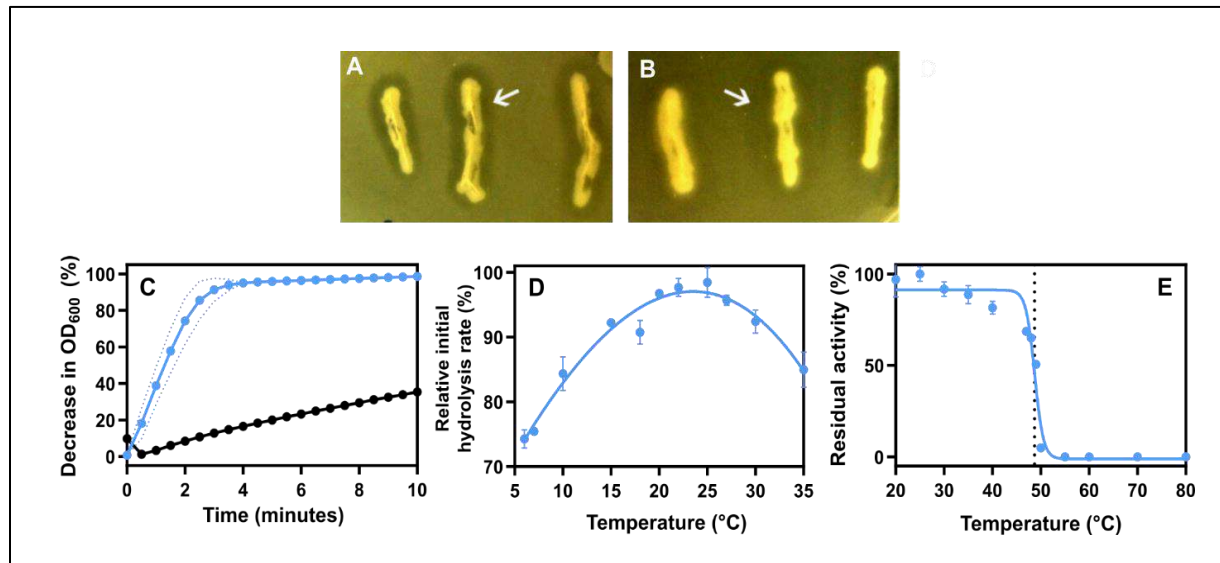


Figure 22. Hydrolysis of PCL by Mors1 and OaCut. **A)** Agar plate containing PCL with *E. coli* expressing Mors1. **B)** Agar plate containing PCL with *E. coli* expressing OaCut. **C)** Time course of PCL hydrolysis (decrease of turbidity of a PCL nanoparticle suspension) by Mors1 (blue) and OaCut (black). Dotted line: standard deviation. **D)** Relative initial hydrolysis rates of PCL nanoparticles by Mors1 at different reaction temperatures; 100% = hydrolysis rate at 25 °C. **E)** Determination of the thermal inactivation temperature ($T_{50} = 48.7$ °C) of Mors1.

The PCL-hydrolyzing activity of the two enzymes was compared by measuring the decrease of turbidity of a PCL nanoparticle suspension. Mors1 completely clarified the suspension after a reaction time of 3 min while OaCut decreased the turbidity by only 28% in this time (**Figure 22 C**).

Analysis of Mors1 by nanoDSF indicated an apparent melting temperature (T_m) of 52.0 °C and an onset temperature for denaturation of 31.0 °C. OaCut showed an apparent melting temperature T_m of 40.4 °C and an onset temperature for denaturation of 34.8 °C (**Table 1**). These values were similar to the T_m of the mesophilic *IsPETase* (Son et al. 2019) and other previously characterized psychrophilic enzymes from *O. antarctica* RB-8, such as the esterase OLEAN_C09750 with a reported T_m of 45 °C (Kube et al. 2013).

Table 1. Onset temperature for denaturation and melting temperature (T_m) of Mors1, OaCut and IsPETase determined with nanoDSF.

	Onset temperature for denaturation ($^{\circ}\text{C}$)	T_m ($^{\circ}\text{C}$)
Mors1	30.97 ± 0.03	52.00 ± 0.08
OaCut	34.77 ± 0.25	40.36 ± 0.12
IsPETase	31.7 ± 0.29	47.1 ± 0.3

Using an enzyme concentration of 4.0 $\mu\text{g/ml}$ (0.13 μM) and a PCL nanoparticle concentration of 0.07 mg/ml, the optimum reaction temperature for PCL hydrolysis by Mors1 was determined at 25 $^{\circ}\text{C}$ (**Figure 22 D**). Mors1 also showed a thermal inactivation temperature (T_{50}) of 48.7 ± 0.1 $^{\circ}\text{C}$ and lost 95% of its PCL-hydrolyzing activity at 50 $^{\circ}\text{C}$ (**Figure 22 E**).

Crystallographic structures of Mors1 and OaCut were not obtained

The SEC-purified OaCut was concentrated to a maximum of 2 mg/ml and subjected to different crystallization conditions. However, the attempt to obtain crystals of OaCut failed despite intensive efforts. Only salt crystals were obtained (**Supplementary Table 4**). Our collaborator, Prof. Richard C. Garratt and his group of Biophysics and Structural Biology from the University of Sao Paulo tried similar crystallization conditions for Mors1, but no crystals were obtained neither.

Mors1 presents higher hydrolysis rates with phosphate buffers and high salt concentrations

A screening of different reaction buffers showed that the highest PCL-hydrolyzing activity was obtained with sodium phosphate and potassium phosphate buffers at pH 8.0 with 81% and 76% of remaining enzyme activity after 72 h of incubation, respectively (**Figure 23 A**). A further increase of the activity by 20% was

observed in the presence of 200 mM NaCl in the reaction mixture (**Figure 23 B**). The incubation of the enzyme in 200 mM NaCl resulted in a 23% increase of enzyme activity after 1 h of incubation when compared to buffer without NaCl. At 500 mM NaCl, Mors1 was completely inactivated. The enzyme retains 51% of its activity after incubation for 20 h in a buffer containing 100 or 200 mM NaCl while losing 75% of its activity in the absence of NaCl.

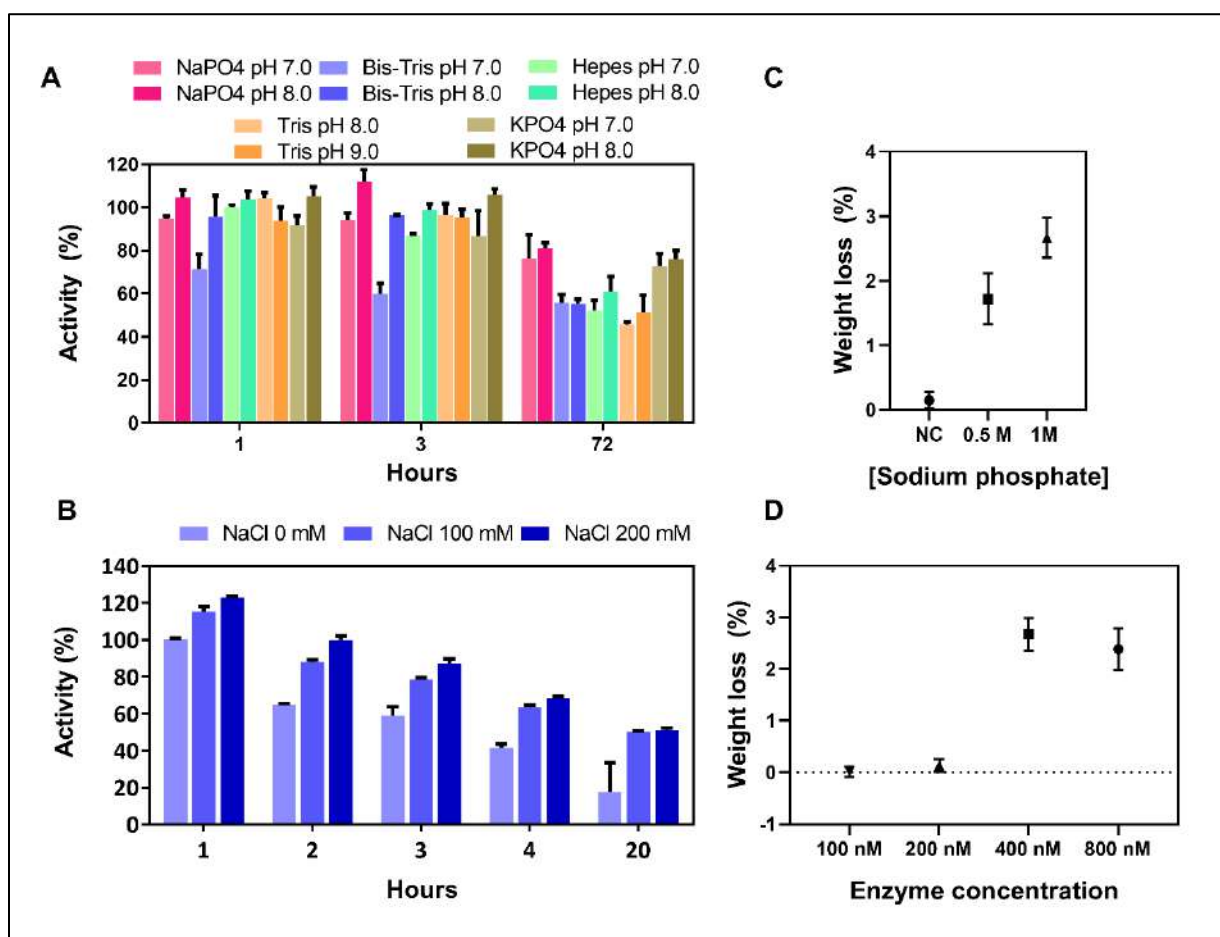


Figure 23. Effect of NaCl and buffer on the hydrolysis of PCL nanoparticles by Mors1. **A)** Relative residual PCL-hydrolysis rates of Mors1 after incubation for 1 to 20 h with NaCl (20 mM HEPES buffer pH 7.5 = 100%). **B)** Relative residual PCL-hydrolyzing activity of Mors1 after incubation for 1 to 20 h with different buffers (20 mM HEPES pH 7.5 with 200 mM NaCl = 100%). All experiments were performed in triplicates. **C)** Effect of the sodium phosphate buffer concentration at pH 8.0 on the PET-hydrolysis by Mors1. The reaction was carried out with an

enzyme concentration of 400 nM for 10 days at 25 °C. **D)** Effect of the enzyme concentration on the PET-hydrolysis by Mors1. The reaction was carried out with 1M sodium phosphate buffer pH 8.0 for 10 days at 25 °C.

These results could be explained by a structural stabilization of Mors1 by phosphate buffers and salt. The results obtained for Mors1 are similar to those observed for LCC and *TfCut2*, where Tris showed a negative effect and phosphate buffers showed a positive effect on the enzyme activity (Schmidt et al. 2016). These results confirm previous reports on the effects of buffer composition and salts on the activity of psychrophilic enzymes (Kube et al. 2013) and polyester hydrolases (Schmidt et al. 2016).

Once buffer, salt and pH conditions were determined with the model substrate PCL, the enzyme concentration and buffer concentration were optimized for PET hydrolysis (**Figure 23 C, D**). A high buffer concentration appeared to be necessary for the performance of the enzyme, as the terephthalic acid released during the hydrolysis reaction would considerably lower the pH and alter the enzyme activity otherwise (**Figure 23 C**). An enzyme concentration around 400 nM seemed to be optimal for PET films of ~ 40 mg with a surface of 1.5 cm² (0.5 x 3cm) (**Figure 23 D**).

Kinetic parameters of PCL hydrolysis by Mors1 are similar to *IsPETase*

When we compared the kinetic parameters for PCL hydrolysis of Mors1 with *IsPETase* and the published data for the thermophilic enzymes from *Thermomonospora curvata*, we observed that both Mors1 and *IsPETase* showed a similarly high PCL-hydrolyzing activity (**Table 2**).

Determination of the kinetic parameters for Mors1 and *IsPETase* (**Figure 24**) demonstrated that their apparent hydrolysis rates (k_{τ}) and adsorption equilibrium constants (K_A) were in a similar range, with *IsPETase* showing a 8.5% higher apparent hydrolysis rate and a 38% higher adsorption equilibrium constant for PCL (**Table 2**). Remarkably, both enzymes showed 13- to 16-fold higher apparent hydrolysis rates and equal or higher adsorption equilibrium constants at 25 °C than their thermophilic counterparts near the melting temperature of PCL (60 °C) (Wei et al. 2014a; Bartnikowski et al. 2019).

Table 2. Kinetic parameters of PCL hydrolysis by Mors1, *IsPETase*, Tcur1278 and Tcur0990.

	k_{τ} ($10^{-3}/\text{min}^{-1}$)	K_A (ml/mg)
Mors1	1544 ± 23.3	152 ± 5.4
<i>IsPETase</i>	1688 ± 81.0	94 ± 7.8
Tcur1278	122.2 ± 11.9	41.1 ± 4.5
Tcur0390	108.3 ± 5.7	96 ± 9.8

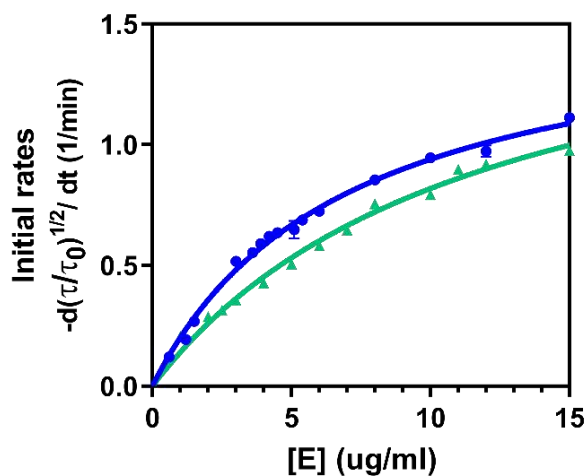


Figure 24. Initial PCL hydrolysis rates by Mors1 (blue) and *IsPETase* (green) at varying enzyme concentrations. PCL hydrolysis assays were performed at 25 °C using 0.07 mg/ml of nanoparticles. Experiments were performed in triplicates.

Mors1 hydrolyzes amorphous PET films at moderate temperatures

We further compared the ability of Mors1 and *IsPETase* to hydrolyze amorphous PET films at 25 °C. After a reaction time of 24 h with 400 nM (11 $\mu\text{g}/\text{ml}$) Mors1 or 100 nM (2.7 $\mu\text{g}/\text{ml}$) *IsPETase* in 1 M potassium phosphate buffer pH 8.0, a 0.59% and 0.46% weight loss of the films was determined, respectively (**Figure**

25 A). While Mors1 and *IsPETase* released similar amounts of terephthalic acid (TPA) and mono(2-hydroxyethyl) terephthalate (MHET), MHET was the main aromatic hydrolysis product of Mors1 at pH 8.0 whereas *IsPETase* mainly produced TPA (**Figure 25 A, Figure 26**). Lower concentrations of Mors1 or higher concentrations of *IsPETase* resulted in a decreased weight loss of the PET films. OaCut caused a lower weight loss of 0.4% compared to Mors1 (1.98%) after a reaction time of 6 days at 25 °C (**Figure 25 B**). Upon longer reaction times up to 10 days, Mors1 degraded 2.5% of the PET films (**Figure 25 C**). The surface of the transparent PET films treated with Mors1 for 10 days became opaque indicating an erosion of the surface (**Figure 25 D**). Analysis by scanning electron microscopy indeed showed the occurrence of pits and grooves on the surface (**Figure 25 E and F**). Similar effects have previously been observed with other PET-hydrolyzing enzymes (Wei et al. 2019a).

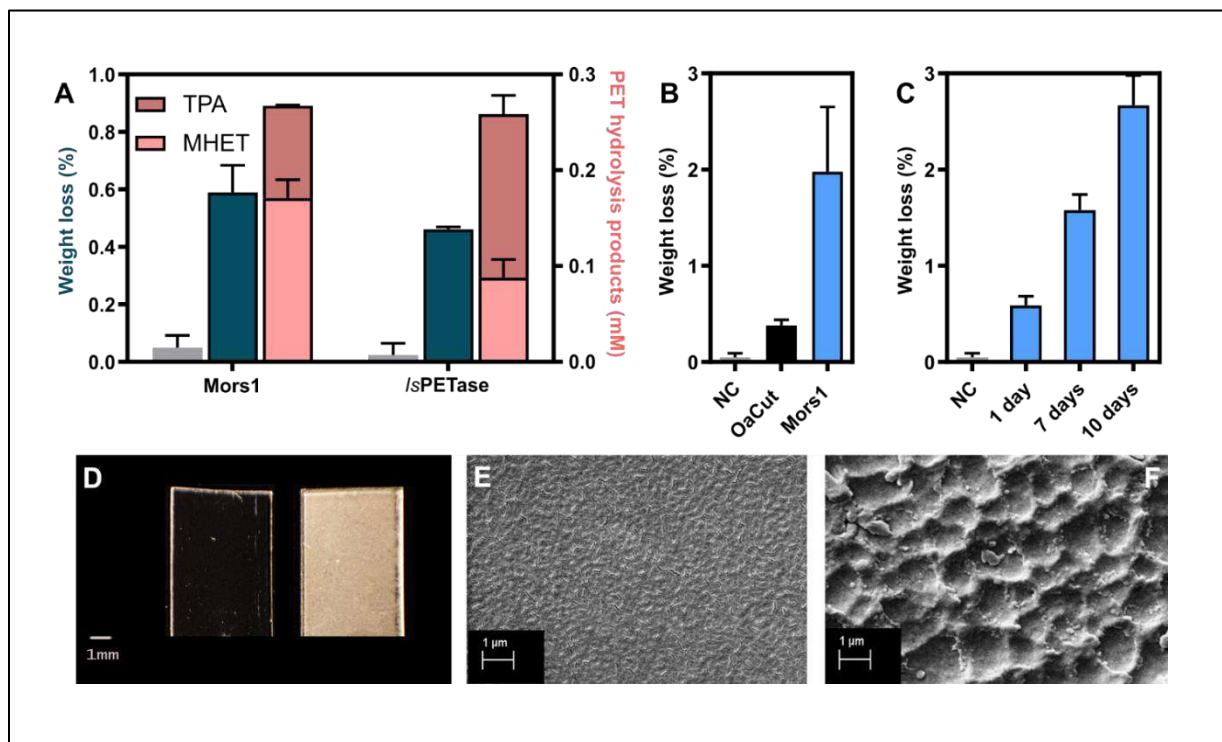


Figure 25. Enzymatic degradation of amorphous PET films. **A)** Weight loss of PET films (in dark green) and amounts of TPA and MHET (in pink) released by Mors1 and *IsPETase* after a reaction time of 24h at 25 °C. In grey, negative control without enzyme. **B)** Weight loss of PET films after a reaction time of 6 days at 25 °C with Mors1 and

OaCut. NC: Negative control without enzyme. **C)** Weight loss of PET films after a reaction time of 1, 7, and 10 days at 25 °C with Mors1. **D)** Surface changes of amorphous PET films. Control (left) and treated with Mors1 for 10 days at 25 °C (right). Scanning electron microscopic images of the surface of an untreated PET film (**E)** and a film treated with Mors1 for 10 days at 25 °C (**F)**.

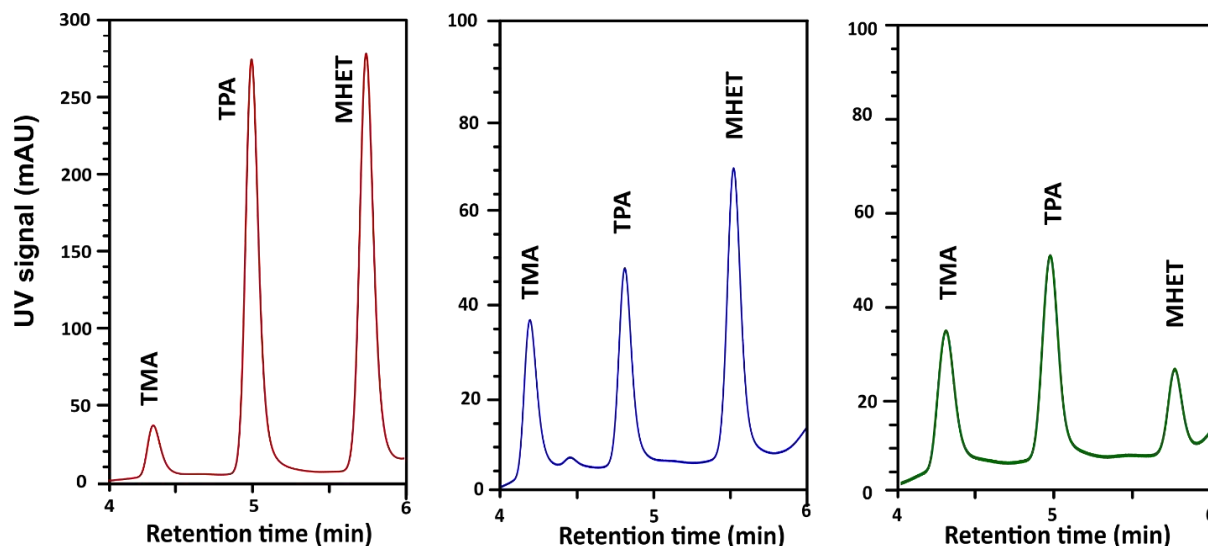


Figure 26. HPLC elution profile of TPA and MHET detected in the supernatant of reaction mixtures of Mors1 and *IsPETase* with amorphous PET films. In red, standards of TPA, MEHT and TMA (Trimesic acid, internal standard), in blue, TPA and MHET released by Mors1. In green, TPA and MHET released by *IsPETase* (dilution factor of 2).

Mors1 is not inhibited by MHET

Inhibition of activity by the PET degradation product, MHET, has been previously reported for *TjCut* enzyme (Barth et al. 2015), which showed a significant decrease in activity when incubated with 2 mM. To test whether Mors1 activity was also affected, a PCL degradation assay was performed in the presence of MHET at a single concentration of 10 mM. No difference in reaction rate was observed between the control and the sample with MHET (**Figure 27**). This result suggests that MHET does not interfere with the active

site of the enzyme. It should be noted that MHET is expected to bind to subsite I of the active site (Joo et al. 2018), so we cannot know whether other larger molecules resulting from PET degradation that also bind to subsite II would have an inhibitory effect.

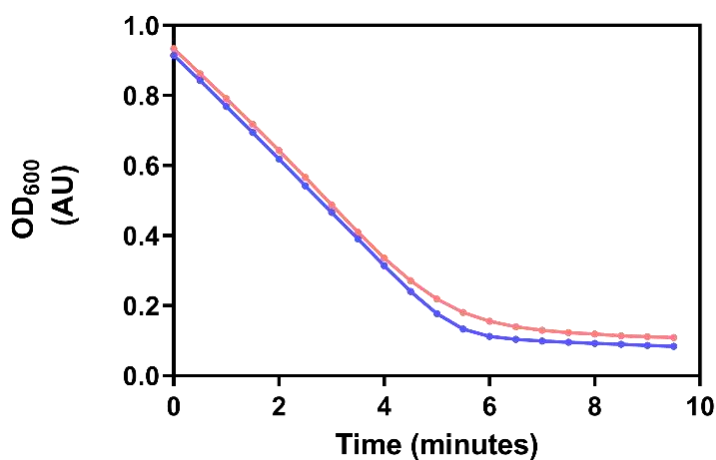


Figure 27. Optical density at 600nm of a PCL nanoparticle suspension during time incubated with Mors1 and MHET. Mors1 (4.0 $\mu\text{g/ml}$) was incubated in 20 mM HEPES pH 7.5 and 10 mM MHET (red). Negative control without MHET (blue). Measurements were performed in triplicates.

The active site of Mors1 presents features from mesophilic and thermophilic PET-hydrolyzing cutinases

Once we established that Mors1 can hydrolyze amorphous PET films at moderate temperatures, we compared the amino acid residue composition of its active site with the mesophilic *IsPETase* and with thermophilic PET hydrolases. We generated a comparative model of Mors1 (**Supplementary Figure 1**) using Rosetta3 (Leaver-Fay et al. 2011) and also performed a multiple sequence alignment (MSA) of Mors1 against *IsPETase* (UniProtKB: A0A0K8P6T7), *OaCut* (UniProtKB: R4YL88), *Thermobifida fusca* cutinase (*TfCut2*, GenBank: PZN61876.1) and the metagenomic leaf-branch compost cutinase (LCC,

UniProtKB: G9BY57). Careful inspection of the MSA (Figure 28 A) and the comparative model of Mors1 (Figure 28 B) showed that Mors1 exhibits features of both mesophilic and thermophilic PET hydrolases.

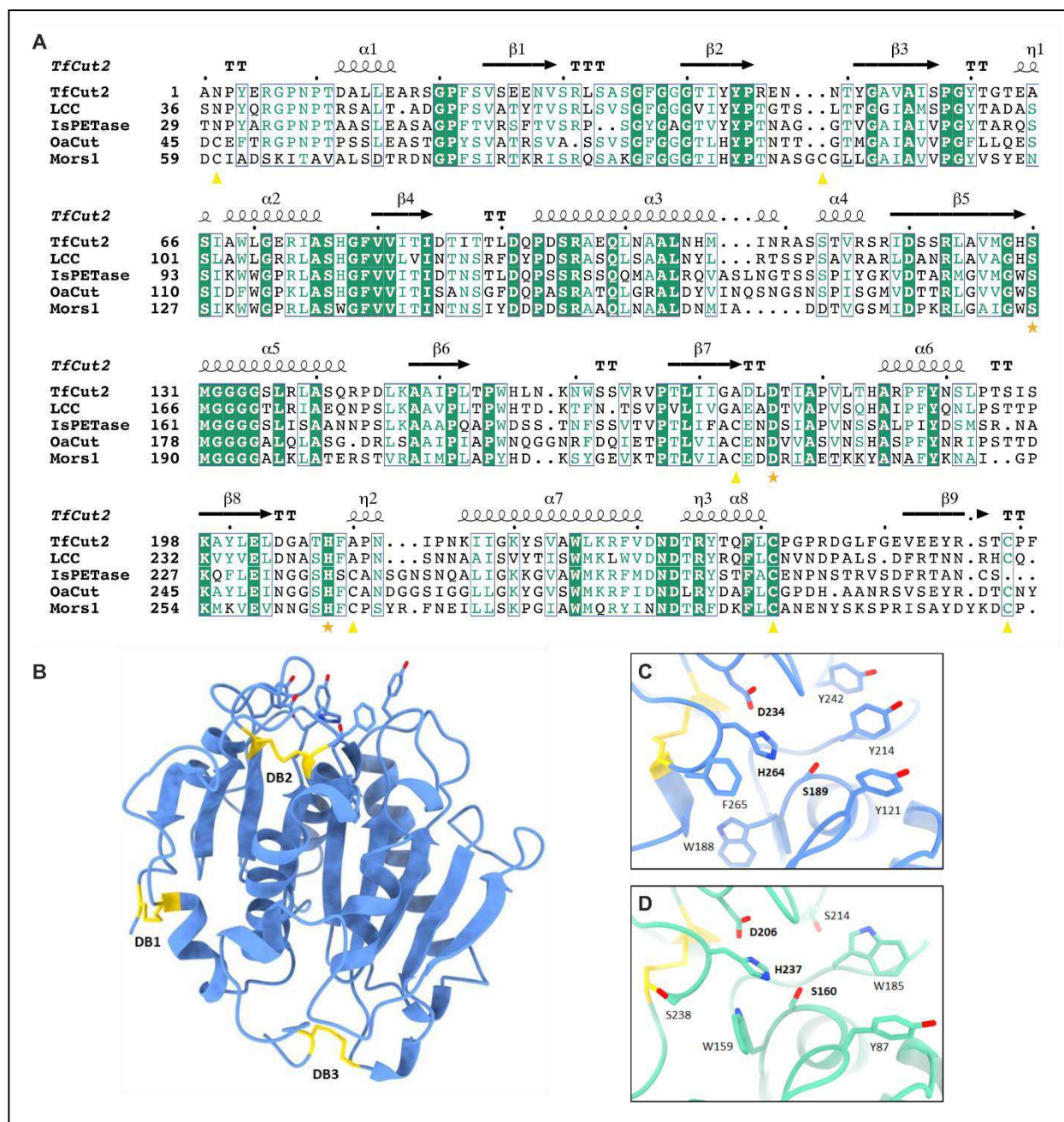


Figure 28. Comparison of the sequence and structure of Mors1, OaCut, IsPETase, TfCut2, and LCC. A) Multiple sequence alignment. Residues numbered according to the full protein sequences with signal peptide. Strictly

conserved residues are highlighted in green background, with yellow triangles indicating Cys pairs that form disulfide bonds and orange stars indicating catalytic residues. A secondary structure topology based on the structure of *TfCut2* (PDB 4CG1) is shown on top of the sequence alignment. **B**) Cartoon representation of the modelled structure of Mors1, showing its three disulfide bridges (DB) in yellow sticks. **C**) Active site of Mors1 (blue), with catalytic residues in bold. **D**) Active site of *IsPETase* (green), showing residues equivalent to Mors1 and catalytic residues in bold.

While all enzymes showed a strict conservation of the catalytic triad (S189, D234, H264 in Mors1) and of a Tyr residue (Y121 in Mors1) important for the activity of these enzymes (**Figure 28 C**) (Joo et al. 2018), *IsPETase* contains an additional disulfide bond (C231-C266 in Mors1, DB2 in **Figure 28 B**) located near the Asp and His residues of the catalytic triad, which is also present in *IsPETase* (C203-C239 in *IsPETase*, **Figure 28 A**) and in other Type IIa and IIb enzymes, that has been shown to be critical for its hydrolytic activity (Fecker et al. 2018; Joo et al. 2018). The model of Mors1 revealed a third disulfide bridge (C60-C109, DB1 in **Figure 28 B**) absent in *IsPETase*, which may constitute an adaptation to low temperatures. By fluorescence labelling of free cysteine thiol groups of Mors1 (Kirley 1989), we confirmed the presence of this additional disulfide bridge (**Supplementary Figure 2**).

While both Mors1 and *IsPETase* also shared the conservation of a Trp residue (W188 in Mors1 and 159 in *IsPETase*), which is substituted by His in thermophilic counterparts, Mors1 carried a Phe residue (F265) that is conserved among PET hydrolases of thermophilic microorganisms and is replaced by Ser in *IsPETase* (**Figure 28 A, C, D**). Both residues have recently been the target for protein engineering of *IsPETase*, leading to a double mutant of this enzyme with improved activity by the addition of His and Phe residues typically found in thermophilic cutinases (Austin et al. 2018). Furthermore, the residues Y214 and Y242 present in Mors1 and in other homologous sequences from psychrophilic organisms corresponded to Trp in all other enzymes, and to His in thermophilic cutinases and Ser in *IsPETase*, respectively (**Figure 28 A, C, D**).

Flexibility as a hallmark of temperature adaptation

In previous reports, the ability of *IsPETase* to degrade PET at moderate temperature has been partly explained by its higher active site flexibility when compared to the thermophilic cutinases (Fecker et al. 2018). Thus, we explored the structural flexibility of Mors1 by MD simulations (**Figure 29**).

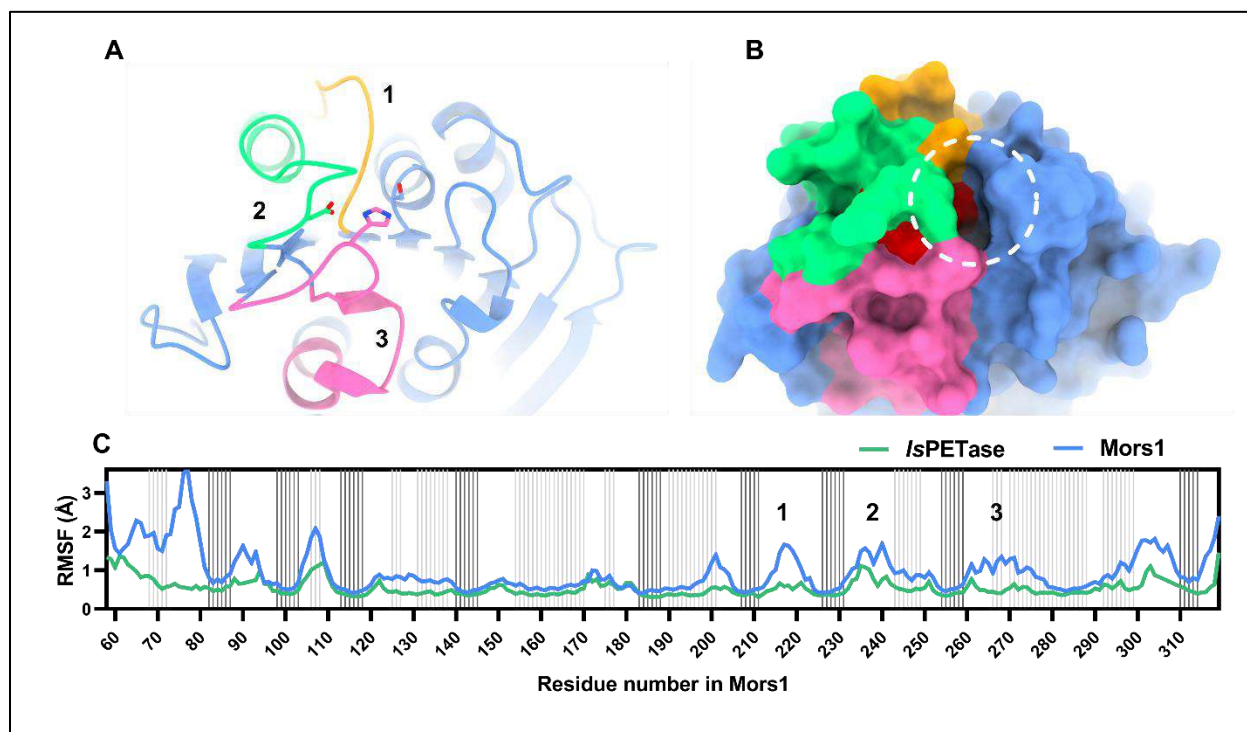


Figure 29. Local structural dynamics of Mors1. **A)** Structure of Mors1 with the flexible regions (1,2,3) around the active site represented in colors. The catalytic triad and disulfide bridge are displayed in sticks. **B)** Surface representation of (A) with the binding groove where the PET is believed to bind encircled in white. **C)** Average backbone RMSF of Mors1 and *IsPETase* structures. The secondary structure is indicated as lines in the background, with α -helices in black and β -sheets in grey. The regions 1,2,3 in the vicinity of the active site show a higher RMFS in Mors1 than in *IsPETase*. The residue numbering corresponds to Mors1.

The analysis of several 100 ns MD trajectories of Mors1 showed regions with significant increments in RMSF when compared to *IsPETase*, particularly of three regions that conform the active site and its surroundings: 1) the β 6- β 7 loop (residues 212-222) where Y214 from subsite I is located, whose equivalent residue in *IsPETase* (W185) is crucial for stabilization of the substrate via π - π interactions; 2) helix 4 and the loops β 7- α 4 and β 8- α 4 (residues 231-251) in Mors1, where the catalytic Asp is located (D324); and 3) loop β 8- α 5 (262-276) where the catalytic His is located (H264), which contains the so called extended loop (271-275) (Joo et al. 2018).

Identification of polyester hydrolases from Antarctic marine environments

To identify further potential polyester hydrolases from Antarctic marine environments, we assembled two marine metagenomes from Chile Bay (Greenwich Island) in Antarctica (NCBI: Bioproject no. PRJNA421008) (Alcamán-Arias et al. 2018) using SPAdes (Bankevich et al. 2012): One was corresponding to a condition of low productivity, based on the concentration of chlorophyll *a* (Low Chl*a*), and the second was corresponding to a condition of high productivity during a phytoplankton bloom recorded in the austral summer of 2014 in Chile Bay (High Chl*a*). Once we obtained all predicted proteins from these metagenomes using Prodigal (Hyatt et al. 2010), we used the full-length amino acid sequence of Mors1 (UniProtKB P19833) as reference to identify homologs from these predicted Antarctic metagenome proteins using BLASTP (Zhang et al. 1998).

This analysis led to the identification of 6 enzymes having 71-90% sequence identity and 56-97% sequence coverage in both metagenomes (**Supplementary Table 8** and **Figure 30**). When analyzing the source contigs, we observed that the proteins with lower sequence coverage (mtgmn1, mtgmn3) were truncated not by the presence of terminal codons, but because the contig was terminated before a protein termination signal could be identified. Moreover, bioinformatic analysis using SignalP (Almagro Armenteros et al. 2019) identified a signal peptide in 4 of these enzymes (mtgmn1, mtgmn3, mtgmn4, mtgmn6), in

consistency to what is observed for all characterized PET hydrolases to date. Regarding the taxonomic affiliation of these enzymes, BLAST analysis against the RefSeq protein database showed that they had high sequence identity (>82%) with proteins of the genus *Psychrobacter* of the Moraxellaceae family (Supplementary Table 9). The difference in the taxonomic assignment of these enzymes to the genus *Psychrobacter* and not to the genus *Moraxella* could be explained by a possibly erroneous sequence annotation of Mors1, which was taxonomically classified using biochemical tests and not genome phylogeny analysis.

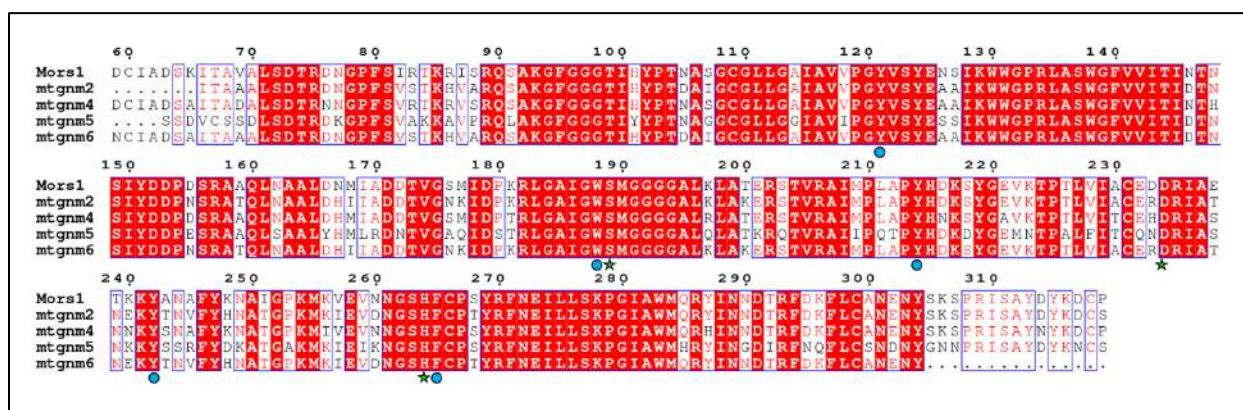


Figure 30. Sequence variability of potential polyester hydrolases from Antarctic metagenomes. A multiple sequence alignment between Mors1 and homologous enzyme candidates with high sequence coverage from Antarctic metagenomes from Chile Bay. Blue boxes indicate columns with either strict (red background) or 75% (red characters) sequence conservation between all enzymes. Green stars indicate conserved catalytic residues, whereas blue spheres indicate active site residues.

When evaluating the relative abundance of the taxa that potentially carry these sequences in the Antarctic metagenomes, we determined that the *Moraxellaceae* family represented ~40% of the total reads assigned as 16S rRNA genes in the Low Chla metagenome. Meanwhile, in the High Chla metagenome, the reads assigned to the *Moraxellaceae* family represented only ~3% of the total. These values were in good

agreement with those reported previously (Alarcón-Schumacher et al. 2019), where Pseudomonadales (to which *Moraxella* and *Psychrobacter* genera belong) was the dominant marine order in a low Chla metagenome, and then Alteromonadales order dominated in a high Chla metagenome obtained during the phytoplankton bloom recorded in Chile Bay in 2014. Using Bowtie2 (Langmead and Salzberg 2012), we determined that the MorsI homologs recruit only 0.0005% and 0.0001% of the total number of reads from the Low and High Chla metagenomes, respectively. This low abundance, compared to the relative abundance of 16S rRNA genes of the *Moraxellaceae* family members, indicates that not all members of this family are carriers of these candidate enzymes.

III.II Improvement of the hydrolytic activity of Mors1 via protein engineering

Single point variants of Mors1 did not improve hydrolytic activity

To determine the change in catalytic activity of the single-point variants of Mors1 on PET and PCL, activity assays were performed with these polyesters using the previously determined buffer, pH, temperature, and enzyme concentration conditions for WT Mors1. The relative PET hydrolysis activity was calculated as the percentage of weight loss obtained by the variants compared to the weight loss of WT Mors1 after 24 h at 25 °C. Similarly, the hydrolytic activity on PCL of the variants relative to the WT Mors1 was calculated as the percentage of the initial hydrolysis rate, monitored as the linear decrease in turbidity of the nanoparticle suspension at 25 °C.

To elucidate the residues involved in PET binding of Mors1 and to improve the PET hydrolysis rate, site-directed mutagenesis experiments were conducted. Key positions for binding within the active site of *Is*PETase (Han et al. 2017; Chen et al. 2018) as well as beneficial mutations previously engineered and tested in this mesophilic enzyme (Ma et al. 2018; Joo et al. 2018) were mutated in Mors1. Residue W185 in *Is*PETase (PDB 5XJH) is a highly conserved residue among PET hydrolases (**Figure 28 A**) and has been shown to be crucial for enzymatic activity (Han et al. 2017). Mors1 has a Tyr at this position (Y214) and when substituted with Trp (Y214W) the hydrolytic activity on PCL remained unchanged, however the activity on PET decreased by more than half. For *Is*PETase, the side chain of this Trp can adopt a conformation that is not allowed in thermophilic enzymes but is more productive for PET binding.

The wobbling of W185 is allowed due to the presence of a Ser residue in the vicinity, which corresponds to His in thermophilic enzymes and compromises Trp movement (**Figure 17** and **Figure 12 A**). When this Ser is mutated for His in *Is*PETase, the activity decreases substantially ($43.87 \pm 0.30\%$ for MHET and $9.73 \pm 0.77\%$ for TPA production) (Han et al. 2017). Mors1 presents a Tyr in the homologous position and when

mutated to His, mimicking the thermophilic enzymes (Y242H) the activity is also reduced (87.5 % for PCL and 84% for PET) (**Figure 31 D**). It was not possible to observe the effect of Y242S on Mors1 because purification of the enzyme was unsuccessful. However, this mutation was inserted into the triple mutant (Y242S/F246I/Y214W). This mutant was made on the basis of recent work that showed that an Ile at position 218 of *IsPETase*, together with S214, increased the mobility of the β 6- β 7 loop where W185 is located, and the addition of these two residues as a double-mutation substantially increases the PET hydrolase activity of type IIb (PbPL and BurPL), type IIa (CtPL, PET2) and type I (*TfCut*) enzymes (Chen et al. 2021). Recreation of these mutations in Mors1 through engineering of the triple variant Y242S/F246I/Y214W led to an enzyme with almost complete loss of activity (92%) for both PCL and PET (**Figure 31 D**), which may be due to local structural destabilization caused by the increased flexibility of the β 6- β 7 loop (**Figure 31 A, B**).

Another mutation that was beneficial for *IsPETase* activity was the exchange of an Ile for Phe (I179F), based on an improvement of the enzyme affinity for PET by increasing hydrophobicity in the active site (Ma et al. 2018). When this residue is mutated in Mors1 (I236F), the activity is completely lost for both PCL and PET (**Figure 31 D**), highlighting the importance of this position within the active site of Mors1. One possible explanation for this phenomenon may be that the Phe side chain hinders the entry of PCL and PET into the catalytic pocket.

Another relevant residue is the Trp located near the catalytic Ser (W188), which also corresponds to a Trp in *IsPETase* but to a His in the thermophilic homologs. Substitution of the native residue by His causes a loss of activity of 87% for both polymers (**Figure 31 D**), similar to what was observed for the W159H (numbering corresponds to PDB 5XJH) variant of *IsPETase* (Han et al. 2017). Mimicking another mutation made in *IsPETase*, R309 was changed to Ala, a residue in subsite II of *IsPETase* that is believed increase the activity due to an enlargement of the active site (**Figure 12**) (Joo et al. 2018). However, this mutation in Mors1 causes a loss of activity of 32% for PCL and 68% for PET (**Figure 31 D**).

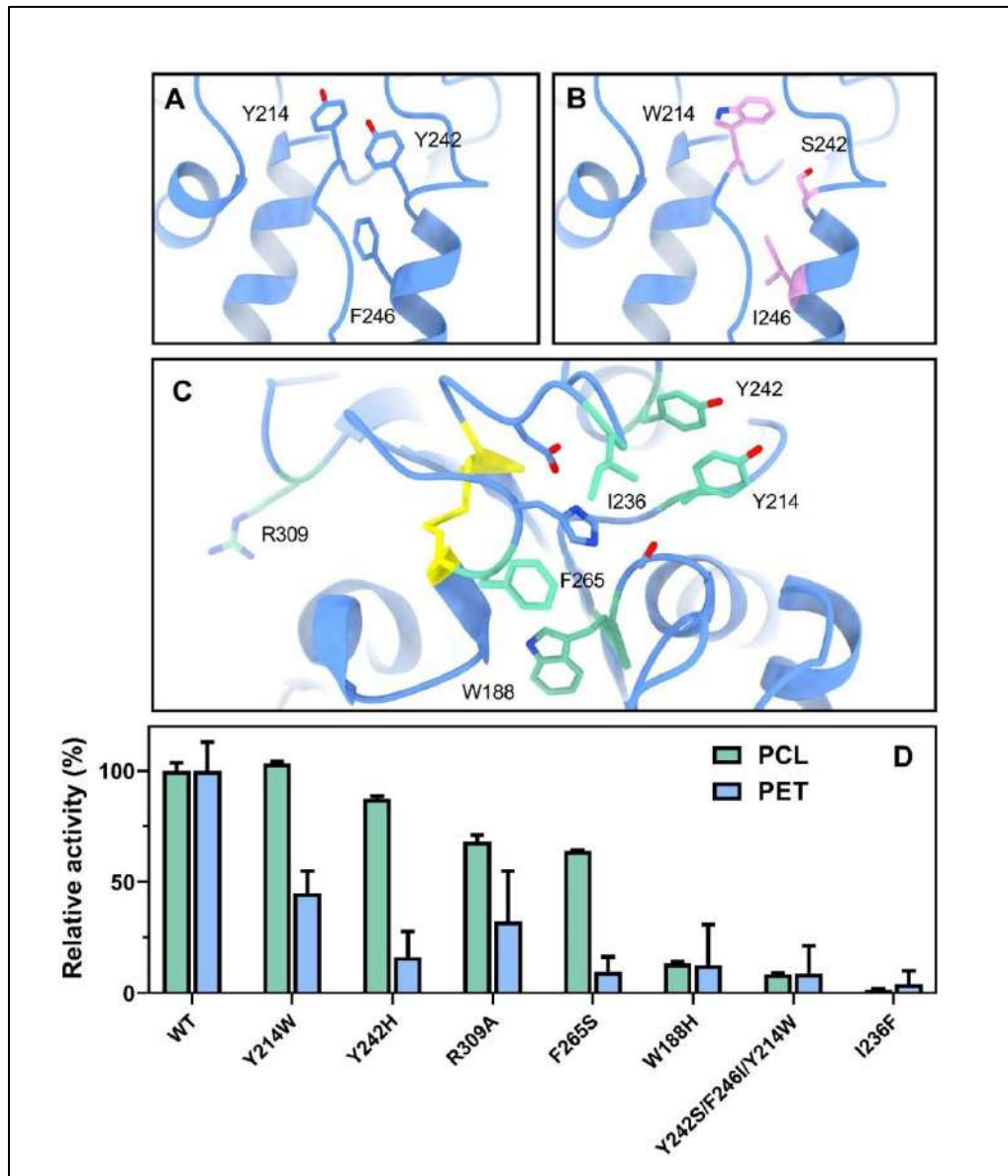


Figure 31. Variants of Mors1 and their activity on PCL and PET. **A)** Structure of Mors1 with the three residues proposed as essential for PET hydrolysis in (Chen et al. 2021). **B)** Mors1^{Y242S/F246I/Y214W} with the three residues mutated indicated in pink. **C)** Active site of Mors1 with the residues mutated in green. In blue and sticks the catalytic triad. In yellow, the disulfide bridge. **D)** Relative activity of the variants on PCL nanoparticles and PET films compared to the WT. Experiments were performed in triplicates.

Finally, Mors1 has a conserved Phe residue (F265) among thermophilic PET hydrolases that corresponds to a Ser in *Is*PETase. When this Ser is exchanged for a Phe in *Is*PETase, the width of the active cleavage is reduced and the activity is slightly increased (Austin et al. 2018). When the Phe of Mors1 is exchanged for a Ser, there is a decrease in activity of 36% for PCL and a very steep drop for PET of 91% (**Figure 31 D**), corroborating that the presence of a Phe is beneficial.

Thermostability of single-point variants remains unchanged

The measurement of the thermostability of Mors1 in 50 mM sodium phosphate buffer, pH 8.0 ($T_m = 57.3$ °C) increased 5.3 °C compared to when the protein is in 20 mM HEPES pH 7.5 ($T_m = 52$ °C). Moreover, the onset temperature is increased very significantly by 15.83 °C, from 30.97 °C for the protein incubated in HEPES to 46.8 °C for the protein incubated in sodium phosphate buffer. This means that the temperature range for the melting curve of Mors1 in phosphate buffer is more reduced. However, this does not mean that the protein in phosphate buffer is active up to 46.8 °C. In line to what was postulated for psychrophilic enzymes, the activity is lost before the proteins reach their thermal denaturation point because their active site is usually more heat-labile than the whole structure (Feller 2013). This phenomenon was observed for Mors1, which showed an optimum activity at 25 °C, while its denaturation started at 31 °C.

As expected, only slight changes in thermostability were observed for the variants. Mutations Y214W and F265S showed a slight increase of 0.8 and 0.1 °C, respectively. Mutants R309A and Y242S/F246I/Y214W decrease their T_m in 0.1 and 0.3 °C, respectively. Only the Y242H and W188H showed a variation greater than 1 °C (1.1 °C and 1.2 °C respectively) (**Figure 32 A** and **Supplementary Figure 4**). The T_m of the I178F variant could not be determined, probably due to the low concentration of the protein in solution. It is noticeable that the curves of the first derivative of the ratio of the fluorescence for the variants show a shift

on the left from the main peak which might indicate two different structural populations (**Supplementary Figure 4**).

To explore the effect of disulfide bridges on the thermostability of Mors1, the enzyme was incubated in the presence of 1 mM and 100 mM DTT, similar to what Tournier et al. assayed with LCC. When they incubated the enzyme with 1 mM DTT, different populations were observed with lower thermostabilities due to the reduction of one or two disulfide bridges. At a concentration of 100 mM DTT, a single population with all three disulfide bridges reduced was observed with a greatly reduced thermostability ($-20\text{ }^{\circ}\text{C}$). When repeated this assay with Mors1 using 1 mM DTT, a population with a T_m of $42.3\text{ }^{\circ}\text{C}$ was observed, which means a $15\text{ }^{\circ}\text{C}$ reduction of the T_m . With 100 mM DTT no curve was observed, this may be due to a structural destabilization, since Mors1 is already a labile protein, reducing all its disulfide bridges could lead to the loss of the native structure (**Figure 32 B**).

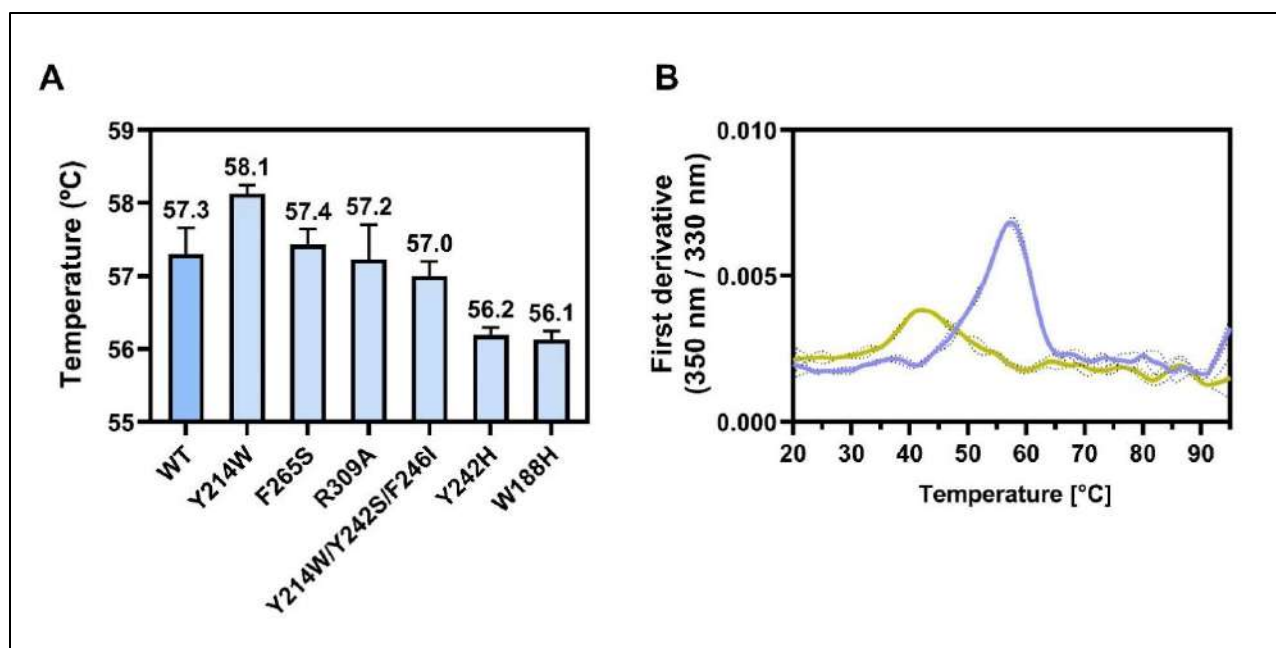


Figure 32. T_m values of Mors1 and variants. **A)** T_m of Mors1 and its variants. Means are indicated above the bars.

B) First derivative of the ratio of the fluorescence measured at 350 and 330 nm from $20\text{ }^{\circ}\text{C}$ to $90\text{ }^{\circ}\text{C}$ of Mors1 in

presence of DTT. Blue: Mors1 without DTT. Gold: Mors1 in presence of 1 mM DTT. Dotted lines represent standard deviations. All the experiments were conducted in triplicates.

Chimeric Mors1 has an improved PET hydrolytic activity

The Type-II PET degrading enzymes, to which *IsPETase* belongs, are characterized by having a loop that conforms the active site longer than the one of Type I enzymes, such as LCC and other thermophilic homologues (Joo et al. 2018). It also possesses an extra disulfide bridge that maintains the integrity of the active site despite the increased flexibility caused by this loop (Fecker et al. 2018). This loop extension of three residues that, according to Joo et al., gives rise to the formation of subsites IIb and IIc, it is also present in Mors1 (residues 271-275) being one of the regions that exhibits a higher mobility within the active site when compared with *IsPETase* (**Figure 29 C**).

Reasoning that the active site loops of Mors1 are more flexible than the mesophilic and thermophilic PET hydrolases, and that loop swapping has been employed as a protein engineering strategy to improve enzyme activity and stability in the past (Nestl and Hauer 2014), a structure-based approach was carried out to rationally design a chimeric protein in which the loop connecting $\beta 8$ - $\alpha 6$ was exchanged for the homologous loop of the thermophilic enzyme LCC. Specifically, the 15-residue region that comprises the highly flexible active site loop within Mors1 (residues 262-276), including the extended loop (residues 271-275), was replaced by the homologous 13-residue region in LCC (residues 203-215), sharing 46.15% sequence identity (**Figure 29 C**).

This chimeric variant, termed CM (chimeric Mors1), lost the active site disulfide bridge (C231-C266) characteristic from Type II enzymes such as *IsPETase* because of the substitution of Cys 266 by Ala. The lack of the disulfide bridge cost the total loss of activity (**Figure 33 A**). However, when the bridge was restored by reversing the mutation of Ala266 to Cys, the respective variant (CM^{A266C}) recovered the

enzymatic activity (**Figure 33 A, C**). While the activity against PCL at 25 °C of CM^{A266C} was equal to that of WT Mors1, it decreased almost 3-fold for PET at the same temperature (**Figure 33 E**).

Reasoning that this could be due to a shift in the optimal temperature for activity of the enzyme, the activity of CM^{A266C} against PCL and PET was also assayed at temperatures up to 65 °C. For PCL, the optimal temperature for the polyesterase activity of this variant was 45 °C, which is 20 °C higher than for WT Mors1 and at which temperature Mors1 is not active (**Figure 33 D**). Moreover, at this new optimal temperature, the PET hydrolase activity of CM^{A266C} is 4.8-fold higher than WT Mors1 at 25 °C. Interestingly, despite this significant increase, the T_m of CM^{A266C} is 1.6 °C lower than for Mors1 and the onset temperature for denaturation is 10 °C lower (**Table 3**). However, the first derivative of the ratio of the fluorescence for CM^{A266C} appears to present two distinct peaks, whereas the curve for CM presents a sharper peak. This could indicate two different populations for CM^{A266C} (**Supplementary Figure 5**). Also, the T_m of the CM variant does not change relative to WT Mors1, in contrast to previous studies showing that the removal of this disulfide bridge caused a drop of 13.2 °C of the T_m in *IsPETase* (Joo et al. 2018).

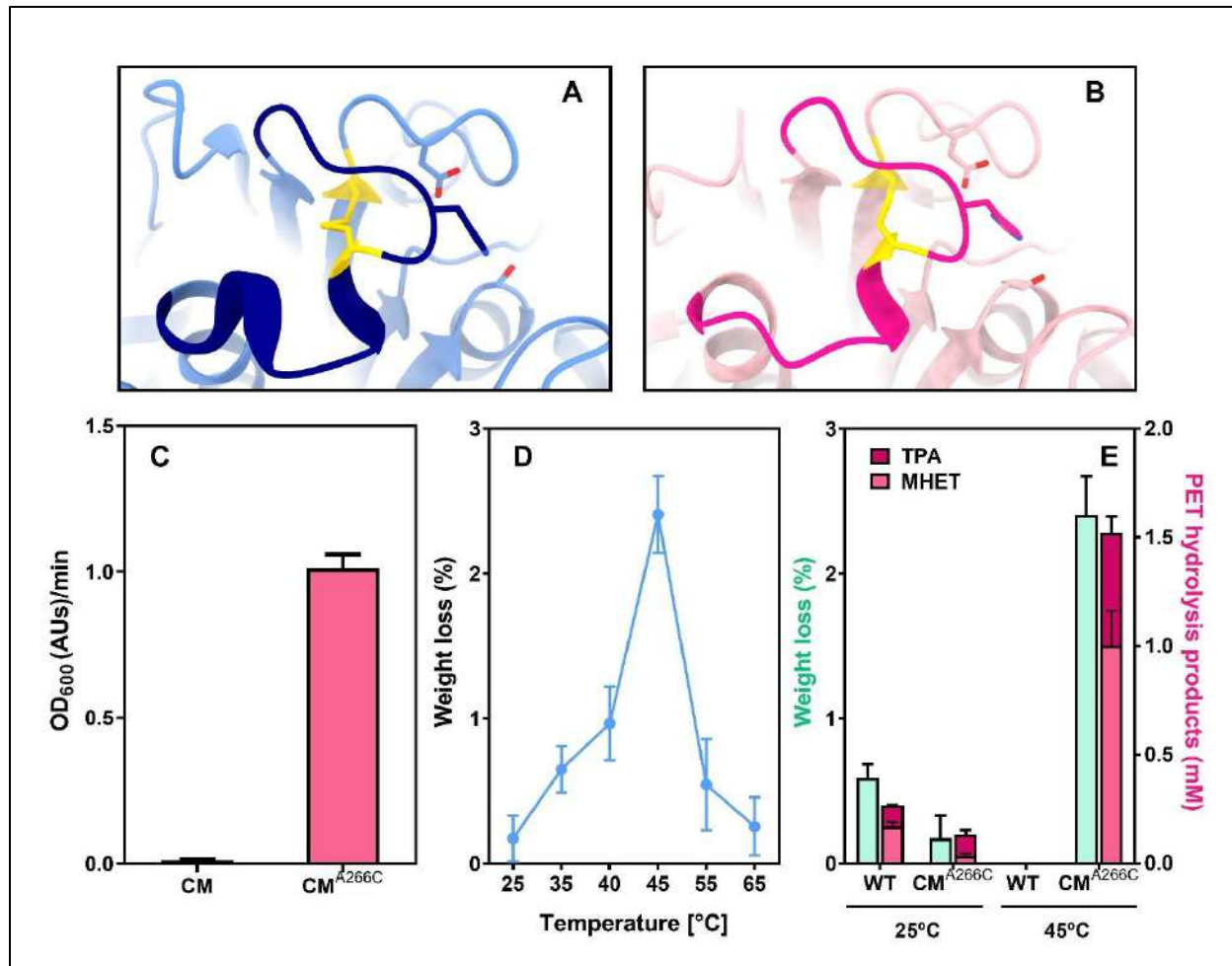


Figure 33. Activity of CM^{A266C} on PET compared to Mors1. **A)** Structure of Mors1 with region 3 indicated in dark blue. **B)** Structure of CM^{A266C} with the region 3 inserted from LCC colored in dark pink. The catalytic triad is showed in sticks. In yellow, the disulfide bridge. **C)** Activity on a PCL nanoparticle suspension of CM and CM^{A266C} measured as a decrease in turbidity (AUs/min) at 25 °C. **D)** Optimal temperature for PET degradation of CM^{A266C} measured as weight loss of PET films after a reaction time of 24 h. **E)** Weight loss of PET films (in green) and amounts of TPA and MHET (in pink) released by Mors1 and CM^{A266C} after a reaction time of 24 h at 25 °C and 45 °C. All experiments were performed in triplicates.

Table 3. Melting temperatures of Mors1, CM and CM^{A266C}. The proteins were in a solution containing 50 mM sodium phosphate pH 8.0 and 200 mM NaCl. Experiments were performed in triplicates.

	Onset temperature for denaturation (°C)	T _m (°C)
Mors1	46.8 ± 1.4	57.3 ± 0.3
CM	40.5 ± 1.6	54.7 ± 0.2
CM^{A266C}	36.8 ± 2.3	55.7 ± 0.3

PCL degradation with crude extract

To test whether PCL activity could be quantitatively determined directly from crude extracts, three cultures of *E. coli* C41(DE3) were grown, one without the recombinant plasmid as a control and two cultures transformed with the Mors1-containing plasmid, one of which was induced with IPTG for protein overexpression. Cells were harvested, lysed by sonication, and centrifuged, soluble fractions were collected, and protein concentration was determined by Bradford assay. The protein concentration in the control was 0.19 mg/ml, in the non-induced sample transformed with the vector 1.25 mg/ml and in the induced sample transformed with the vector 0.91 mg/ml. The samples were diluted to equal their concentrations and the PCL activity of the crude extracts was assessed by measuring the decrease in absorbance of a solution of PCL nanoparticles (**Figure 34 A**). The activity of the induced sample without diluting was also compared to the control (**Figure 34 B**).

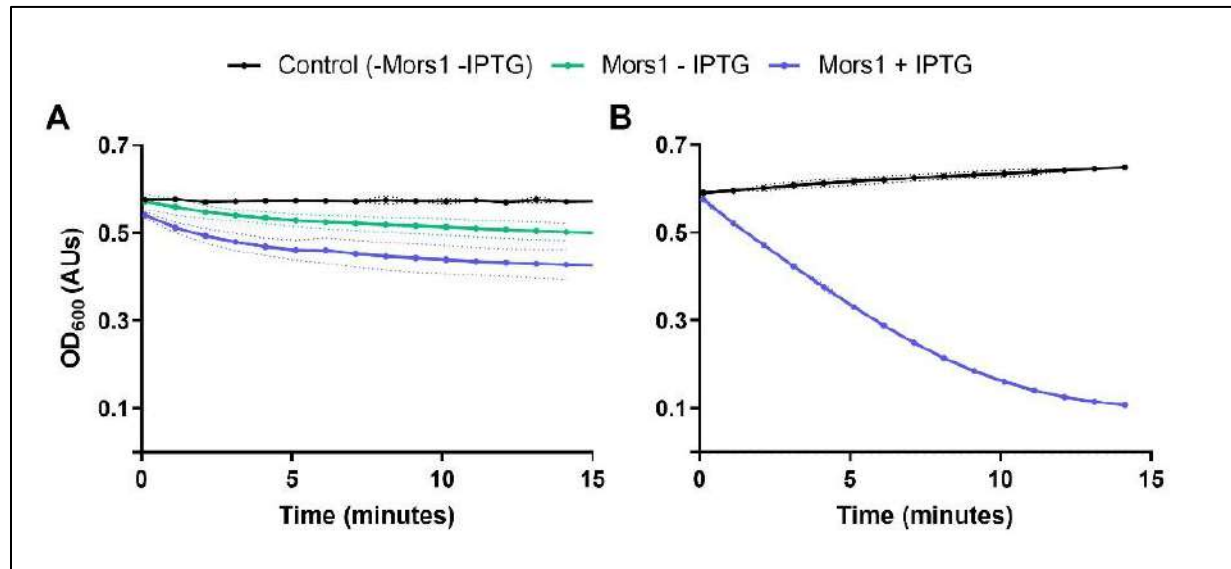


Figure 34. PCL degradation with crude extracts. **A)** Time course of PCL hydrolysis (decrease of turbidity of a PCL nanoparticle suspension) by crude extracts from *E. coli* cultures without plasmid (negative control, black), with Mors1-containing plasmid uninduced (green) and with Mors1-containing plasmid induced (blue). Protein concentration in the three samples was 0.19 mg/ml. The control and the +Mors1+ IPTG samples were diluted to equal the concentration of +Mors1 -IPTG sample. **B)** Time course of PCL hydrolysis comparing the control (0.19 mg/ml) and the transformed with Mors1-containing plasmid and induced with IPTG (0.91 mg/ml). Small, dotted lines: standard deviation. Experiments were performed in triplicates.

The results showed that both, the induced and non-induced transformed cultures had activity on PCL, with the activity of the induced culture being higher than that of the non-induced culture. No activity was observed in the control, which means that *E. coli* enzymes cannot degrade PCL, or at least it is not observable in the amounts that are expressed in *E. coli*. The presence of PCL-hydrolytic activity in the non-induced culture shows that the vector has protein expression leakage and Mors1 is not fully regulated by IPTG. Nevertheless, these results confirm that it is possible to measure PCL hydrolytic activity from crude extracts without the need for purifying the proteins.

MD simulations of the loop swapping variant

To prove our hypothesis that CM^{A266C} improved activity at 45 °C was due to a reduction in the active site flexibility, MD simulations were performed at 25 °C and 45 °C with Mors1 and CM^{A266C} homology models. The integrity of the catalytic triad was assessed in each replicate by measuring the mean distance between Ser160-His237 and His237-Asp206 (

Supplementary Table 7). The results showed that at 25 °C, only one replicate out of 4, for each protein, showed a sufficiently close distance between the catalytic residues for hydrogen bridges to form. A distance of up to 3.6 Å was accepted as valid, which is close to the established range of 2.7 to 3.3 Å (McRee 1999). Based on this, Mors1 replica 4 and CM^{A266C} replica 4 were chosen for the subsequent RMSF analysis. When this same analysis of the replicates was performed at 45 °C, none of the replicates of Mors1 or CM^{A266C} met the established minimum distance (

Supplementary Table 7).

RMSF analysis of the replica 4 for Mors1 and CM^{A266C} was performed. CM^{A266C} showed slightly reduced mobility in the swapped loop region, especially in residues 270 and 271 of the extended loop (**Figure 35**). The mean RMSF for this region was 0.91 Å for CM^{A266C} and 1.12 Å for Mors1. This could be an indication that this region was indeed stabilized by swapping its loop with that of LCC.

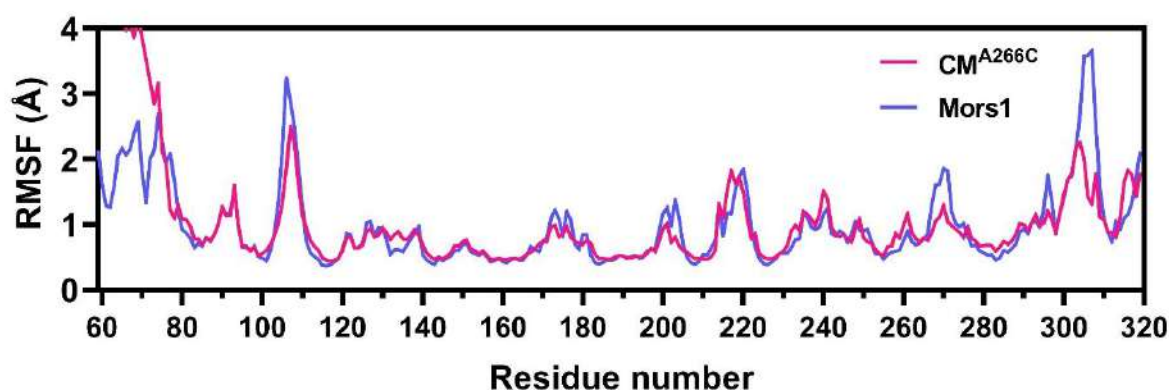


Figure 35. Average backbone RMSF of Mors1 and CM^{A266C}. Simulations were performed at 25 °C for a time span of 1000 ns. RMSF of replica number 4 for each structure are shown. The region mutated in CM^{A266C} (residues 262-276) showed a slightly reduced flexibility. The residue numbering corresponds to Mors1.

III.III Characterization of the thermophilic PHL7 enzyme binding residues

The results provided in this sub-chapter are published in the following article:

Sonnendecker C, Oeser J, Richter PK, Hille P, Zhao Z, Fischer C, Lippold H, **Blázquez-Sánchez P**, Engelberger F, Ramírez-Sarmiento CA, Oeser T, Lihanova Y, Frank R, Jahnke H-G, Billig S, Abel B, Sträter N, Matysik J, Zimmermann W (2021) Low Carbon Footprint Recycling of Post-Consumer PET Plastic with a Metagenomic Polyester Hydrolase. *ChemSusChem* 1–11 .
<https://doi.org/10.1002/cssc.202101062>

The thermophilic polyester hydrolase LCC (PDB: 6EB0), first described by Sulaiman et al. (Sulaiman et al. 2012) and found in a leaf branch compost pile, has been the enzyme with the highest specific activity on PET reported so far. Tournier and coworkers created a variant of this enzyme in which they added a disulfide bridge in the vicinity of its active site (D238C/S283C) that increased its T_m by 9.8 °C. This variant, although possesses a melting temperature of 94.5 °C, lost 28% of its activity. To restore the catalytic activity, the authors explored the key residues in binding by docking and selected eleven positions to mutate by site-specific saturation mutagenesis. As a result, 209 variants were created, of which 25 showed 75% or more activity than the wild type. Two variants with a mutation in position 243 that exchanged a Phe for either Ile or Trp exhibited better activity than the WT enzyme. These two mutations were added to the thermostable variant, thus creating the ICC (F243I/D238C/S283C) and the WCC (F243W/D238C/S283C) variants that restored the activity by 122% and 28% and presented an increased T_m compared to the WT enzyme of 6.2 °C and 10.1 °C, respectively. Moreover, from the 25 variants that showed 75% or more activity than the wild type, the ones with an increased thermal stability were chosen: T96M, Y127G, N246D and N246M and these mutations were introduced into ICC and WCC. The resulting variant ICCG (F243I/D238C/S283C/Y127G) presented the best trade-off between specific activity and thermal stability, depolymerizing 90% of post-consumer PET in 9.3h with a ratio of 3 mg of enzyme per g of PET, a rate of $105.6 \pm 3.9 \text{ mg}_{\text{TAEq}} / \text{h mg}_{\text{enzyme}}$ (Tournier et al. 2020).

However, the good performance of LCC^{ICCM}, was recently overcome by the polyester hydrolase, also isolated from a compost, PHL7, showed an outstanding ability to hydrolyze PET by completely degrading a PET film in 18h in a ratio of 0.6 mg_{enzyme}/g_{PET}, with an initial velocity of 6.8 $\mu\text{m h}^{-1}$. Although PHL7 presents a high identity to LCC (94%), its activity is twice as high as that for LCC for amorphous PET films after 16 hours of reaction at 70 °C (Sonnendecker et al. 2021).

The difference in RMSD between the two enzymes, PHL7 (PDB: 7NEI) and LCC (PDB: 4EB0), is only of 1.08 Å and the aminoacidic composition in the active site also exhibits similarities: PHL7 residues G62,

T64, S69, H130, M132, W156, A180, N213, together with the catalytic triad S131, D177, H209 are conserved. Only four residues within the binding pocket differ: F63 (LCC: Y95), L93 (F125), Q95 (Y127), I179 (V212). Moreover, the exchange of L210 in PHL7 by Phe, which is conserved among LCC and other homologous of PHL7, decreases the activity to the level of its homolog, PHL3. Likewise, when F210 in PHL3 was replaced by Leu, the activity increased to the level of PHL7, giving a clue to the importance of this residue within the binding pocket of PHL7 (Sonnendecker et al. 2021).

In this work, we studied the binding mode of EMT, MHET and TPA in PHL7 and the energetic contribution of the residues of the catalytic pocket of PHL7 and LCC with these ligands by docking. Previous results obtained with the polyester hydrolase *IsPETase* indicated that the per-residue energetic contributions to binding affinity are in good agreement with the catalytic contributions of active site residues towards PET hydrolysis (Fecker et al. 2018). In this study, 40,000 structures of enzyme-substrate and enzyme-product complexes were generated and clustered by conformational similarity based on measuring the difference in RMSD of the ligands in the top 100 docking poses. For PHL7, 29 out of 100 of the lowest binding energy EMT docking poses positioned a terephthalic ring in the same groove as seen for p-nitrophenol and 4-methyl terephthalate (HEMT) in solved structures of *IsPETase* (Han et al. 2017) (**Supplementary Figure 7**). A similar EMT binding conformation was found in 19 complexes with LCC (**Supplementary Table 10** and **Supplementary Figure 8**). Further analysis of the five best EMT-bound complexes of PHL7 and LCC demonstrated that their binding energies were similar (-11.9 ± 1.0 and -12.0 ± 0.6 Rosetta Energy Units (REU) for PHL7 and LCC, respectively), but the specific per-residue contributions to ligand binding varied between these enzymes (**Figure 36 B**).

Residue F63 in PHL7, which conforms with the aromatic clamp of subsite I of polyester hydrolases (Joo et al. 2018) contributed almost twice the binding energy than the equivalent residue Y95 in LCC, whereas no differences were observed for the aromatic clamp residue W156 (W190 in LCC) (**Figure 36**). Other subsite I residues, such as the contiguous T64 and I179 gave a small contribution to EMT binding not found in

LCC. In contrast, residues near or within subsite II in LCC (S101, Y127, H242, F243) gave a higher contribution to EMT binding than the equivalent residues in PHL7 (S69, Q95, H209, L210). Among them, residue F243 (LCC), which is characteristically replaced by Ser in *IsPETase* (Fecker et al. 2018) and other Type IIb polyester hydrolases (Joo et al. 2018) and is also replaced by L210 in PHL7, is one of the three residues that contributes most of the binding energy in LCC but has a negligible contribution towards EMT binding in PHL7. These results suggest that the Phe/Leu replacement could be partially responsible for the changes in per-residue binding energy contributions in PHL7, similarly to what was observed for *IsPETase* by the substitution of the highly conserved Phe in thermophilic enzymes by Ser (Fecker et al. 2018).

Energetic analysis of the five best docking poses for MHET (**Supplementary Figure 7**) showed that its binding was more favored in PHL7 (-10.7 ± 0.4 REU) than in LCC (-9.2 ± 0.2 REU). The same phenomenon was observed for TPA (**Supplementary Figure 7**) (-10.0 ± 0.4 and -9.0 ± 0.3 REU for PHL7 and LCC, respectively). Interestingly, the per-residue contribution of F63 in subsite I towards MHET and TPA (**Supplementary Figure 9**) binding was lower than for EMT (**Figure 36 B** and **Figure 37**), and similar to the energetic contribution of Y95 in LCC.

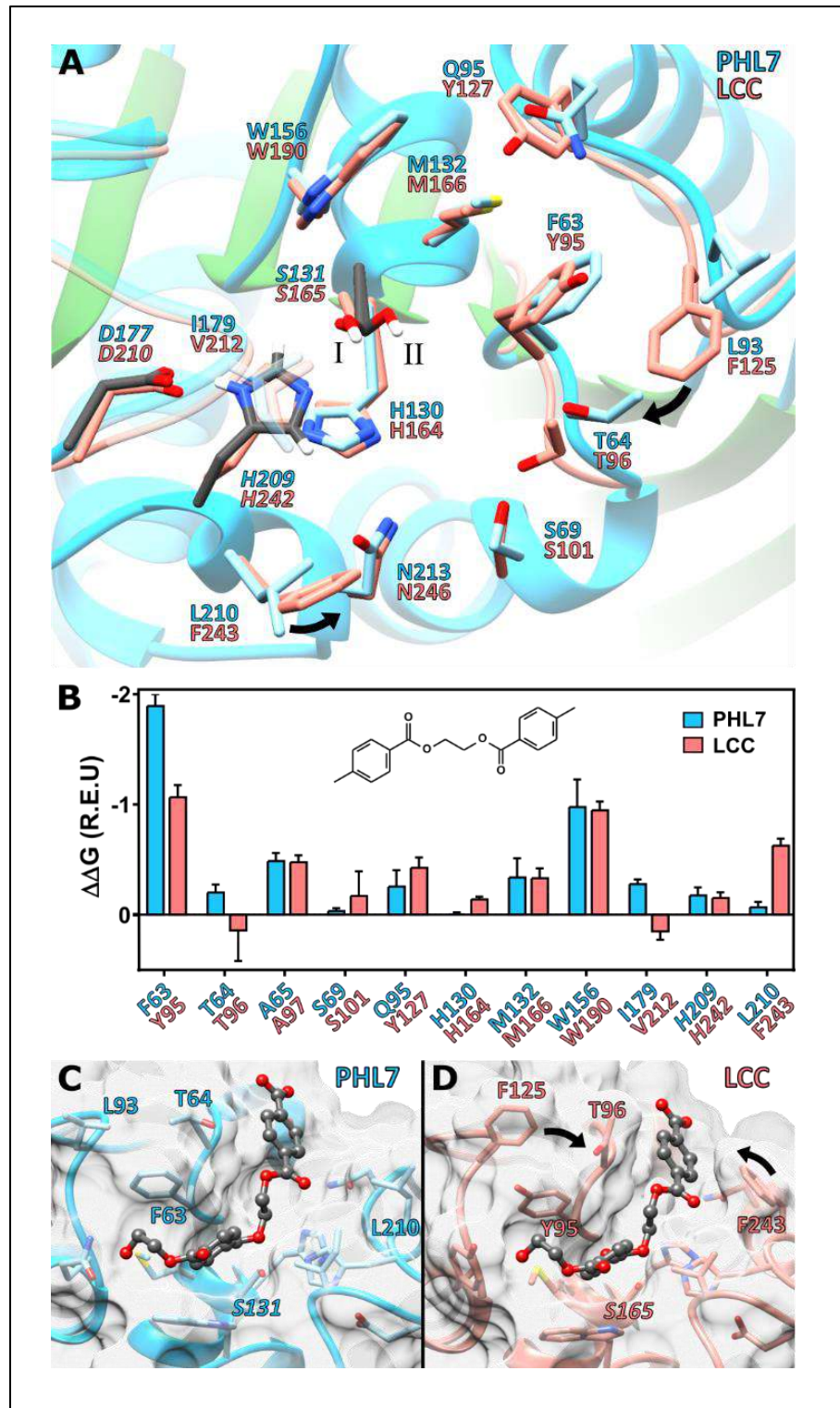


Figure 36. Comparison of the crystal structures of PHL7 and LCC and docking experiments. A) Active site structure of PHL7 (chain A) and LCC. S131 adopts two different conformations of which the most occupied is

displayed. **B)** Predicted per-residue binding energy contribution based on a docking of 1,2- ethylene-mono-terephthalate-mono(2-hydroxyethyl terephthalate) (EMT) in PHL7 and LCC. The best five out of 40,000 complexes with the lowest interface binding energy and RMSD lower than 1.5 Å in relation to the p-nitrophenol and HEMT co-crystal structure of *IsPETase* are shown (Han et al. 2017). **C)** and **D)** Lowest RMSD pose of the 0.25% best interface binding energy complexes of EMT with PHL7 (**C)** and LCC (**D)**) (Sonnendecker et al. 2021).

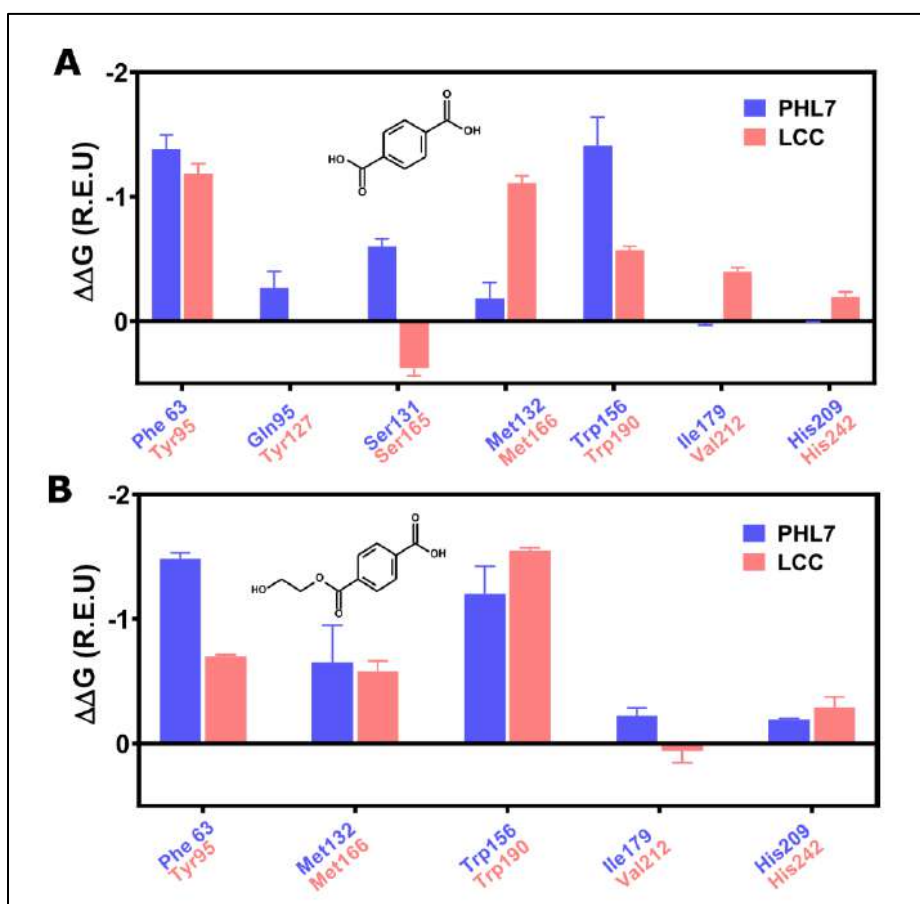


Figure 37. Predicted per-residue binding energy contributions for TPA (A) and MHET (B) in PHL7 and LCC. The best five complexes from a total of 40,000 with the lowest interface binding energy and a RMSD lower than 1.5 Å in relation to the HEMT crystal structure (Han et al. 2017) were selected.

CHAPTER IV.

DISCUSSION AND CONCLUSIONS

Discussion

In this work, two protein sequences from the Antarctic bacteria *Moraxella sp.* strain TA144 (Mors1) and *Oleispira antarctica* RB-8 (OaCut) were functionally and structurally characterized, demonstrating their ability to hydrolyze the aliphatic polyester PCL and the aromatic polyester PET at moderate temperatures, with Mors1 showing a higher activity. While the degradation of PCL by OaCut has been reported previously, hydrolysis of PET had not been observed (Danso et al. 2018).

The hydrolysis of PCL at 30 °C by a lipase from *Moraxella sp.* TA144 (MorEst) has also been reported (Nikolaivits et al. 2020). A weight loss of 18% after 3 days of reaction was achieved in a mixture containing 10 mg/ml of powdered PCL with 25 mg of enzyme and a further addition of 12 mg of MorEst 24 and 48 h later. MorEst also hydrolyzed bis(2-hydroxyethyl) terephthalate and a PET dimer, but a commercial PET sample was not hydrolyzed. Since the sequence of the enzyme was not communicated, the identity of MorEst with Mors1 could not be determined.

It has been previously demonstrated that polyester hydrolases, for example the metagenomic leaf-branch compost cutinase LCC or Tcur1278 and Tcur0390 from the thermophilic actinomycete *Thermomonospora curvata* efficiently degraded PCL at a reaction temperature of about 50 °C (Sulaiman et al. 2012; Wei et al. 2014b). *IsPETase* has been described not to be able to degrade aliphatic polyesters such as polybutylene succinate and polylactic acid (Austin et al. 2018). In contrast, *IsPETase* and Mors1 exhibit similar kinetic parameters for the hydrolysis of the aliphatic polyester PCL at pH 8.0 at a reaction temperature of 25 °C.

Regarding PET hydrolysis, Mors1 showed a considerable higher PET-degrading activity than OaCut. Mors1 caused a weight loss of amorphous PET films and released PET hydrolysis products at optimum reaction conditions in the same range as the mesophilic *IsPETase*, demonstrating the ability of Antarctic psychrophilic enzymes to degrade PET, although it is worth noting that the activity of *IsPETase* can be further increased by about 3-fold at pH 9.0 (Yoshida et al. 2016).

A classification of PET hydrolases based on their amino acid residue conservation in subsites I and II within the active site of these enzymes (Joo et al. 2018) enabled to categorize OaCut as a Type IIa enzyme due to its residue composition (L105, L106, W176, F256, F259 in subsite II). In contrast, Mors1 presented differences in both subsites (D153, Y214 in subsite I; V122, S123, W188, F265, S268 in subsite II), which impedes its unambiguous classification under any of the Type I, IIa or IIb categories. These results suggest that the composition of the active site of these polyester hydrolases is more diverse than previously considered.

Computational analysis of the sequence and structure of Mors1 suggested that its ability to hydrolyze PCL and amorphous PET at moderate temperatures is due to features that this enzyme shares with both thermophilic PET hydrolases and the mesophilic *IsPETase*. The presence of a disulfide bond near the active site, absent in thermophiles but equivalent to the one found in Type II enzymes (Joo et al. 2018) was a prominent indicator that Mors1 could also show polyester-hydrolyzing activity at moderate temperatures. In *IsPETase*, this disulfide bond compensates the increased structural flexibility of its active site while keeping the integrity of the catalytic triad. An opening of the disulfide bond decreased the V_{\max} for the hydrolysis of *p*-nitrophenyl acetate by almost 28% (Fecker et al. 2018) and its replacement by Ala causing a T_m drop of 13.2 °C (Joo et al. 2018). Our MD simulations provided evidence that Mors1 also possesses a highly flexible active site, which could explain its activity at 25 °C. Our analysis suggested the presence of a further disulfide bond (C60-C109) in Mors1, which could also correspond to the stabilization strategy of psychrophilic and psychrotropic organisms to counterbalance the additional flexibility on the structure of their enzymes (Fecker et al. 2018). The effect of this putative disulfide bridge on the structural stability of Mors1 could be assessed by comparing the mobility of the region around the disulfide bridge of Mors1 and an *in silico* mutant with alanine-substituted cysteines C60-C109. Higher mobility would be expected in the mutant for the loops composed of residues 59-82 and 104-112.

The increased flexibility of regions that contain both catalytic and substrate binding residues could be indicative of enthalpic-entropic tradeoffs to enable PET hydrolysis at moderate temperatures, as it has been shown for other cold-active enzymes (Santiago et al. 2016). However, further docking experiments followed by MD simulations are required to analyze such tradeoffs in the active site of Mors1.

Reasoning that there could be more enzymes from Antarctic microorganisms catalyzing the hydrolysis of polyesters at moderate temperatures and considering recent bioinformatic analysis of proteome and metagenome databases that identified 6 Antarctic enzymes among 853 potential PET hydrolases from marine and terrestrial environments (Danso et al. 2018), we performed a metagenomic analysis of Antarctic marine environments. The results provided evidence for the presence of further potential polyester hydrolases homologous to Mors1 with likely similar activities in Antarctic coastal waters, specifically in members of the family Moraxellaceae. Among 6 new enzymes identified with moderate to high identity to Mors1, we observed a localized sequence variability in regions near the active site residues, which suggested potential differences in their polyester-hydrolyzing activity. Interestingly, mtgmn sequences 4 and 6 also have Cys at position 60 and 109, which may indicate that the disulfide bridge 1 (DB1) is a common feature of a new type of PET-hydrolase enzymes.

No homologous Antarctic enzymes were detected outside the family Moraxellaceae, which could be due to a specific niche inhabited by some members of the Moraxellaceae family. The low abundance of the enzyme sequences in Antarctic metagenomes compared to the relative abundance of the Moraxellaceae family members in the bacterial marine community suggests a possible niche function of members of this family in using these hydrolases.

Although *IsPETase* and Mors1 catalyzed the hydrolysis of amorphous PET at moderate temperatures, their hydrolysis rates remained low when compared to thermophilic cutinases at higher temperatures. Due to the stiffness of the PET polymer below its glass transition temperature above 60 °C, an extensive degradation of PET cannot be expected at 25 °C (Wei et al. 2019b). However, in applications requiring a limited

hydrolysis of PET at moderate temperatures, for example in laundry detergents for synthetic textiles (Dong et al. 2020), the Antarctic psychrophilic polyester hydrolases have the potential to become valuable industrial biocatalysts in the future.

Determining the existence of metabolic pathways to assimilate PET degradation products in Antarctic microorganism communities (Meyer-Cifuentes et al. 2020) could give further clues as to whether there is an evolutionary adaptation of microorganisms to consume PET in the environment or if the ability of the described enzymes to hydrolyze PET is rather due to their unusual broad substrate specificity.

Our results established that Mors1 and OaCut are polyester hydrolases able to hydrolyze both aliphatic and aromatic polyesters at moderate temperatures. Sequence comparison analysis showed that the active site of Mors1 contained features of both the mesophilic *IsPETase* and thermophilic enzymes. Metagenomic analysis of Antarctic seawater samples enabled the identification of potential further PET hydrolases of the Moraxellaceae family, their abundance in the marine community, and sequence variations. Altogether, our results describe an Antarctic psychrophilic enzyme that degrades amorphous PET at moderate temperatures, furthering our understanding of the sequence variations that have allowed the emergence of this catalytic activity in nature.

To explore key PET binding residues in the active site of Mors1 and to enhance catalytic activity, single-point variants were created based on published literature for *IsPETase* and thermophilic enzymes. The mutations added to Mors1 mimicked previous mutations that increased catalytic activity in *IsPETase*, such as I236F (Ma et al. 2018), R309A (Joo et al. 2018) or mimicked key residues described for binding in *IsPETase* such as Y214W, Y242S, F265S (Han et al. 2017), or in thermophiles (W188H, Y242H). In addition, a triple mutant was created based on the insertion of amino acids S214 and I218, unique to *IsPETase*, which are associated with the wobbling of W185 (Han et al. 2017). Upon insertion of these two amino acids into other type IIb (PbPL and BurPL), type IIa (CtPL, PET2) and type I (*TfCut*) proteins, their activity with PET increased (Chen et al. 2021). In the case of LCC, the maximum activity did not increase

but the optimum temperature was shifted 10 °C lower, presenting the same efficiency at 60 °C as the wild type at 70 °C. As Mors1 did not have the Trp corresponding in *IsPETase* to W185, it was also added. However, this triple mutant lost almost all activity relative to WT. This may be because residues F246I and Y242S increase the flexibility of the $\beta 6$ - $\beta 7$ loop, and since Mors1 is already a thermolabile protein, this change may have completely destabilized the structure.

None of the point mutations enhanced Mors1 activity against PET neither against PCL but decreased it. Of particular interest are the W188H and I236F variants, which almost completely reduced activity indicating that both positions are important for substrate binding. In *IsPETase*, changing Ile to Phe increased hydrophobicity in the generating a 2.5-fold increase in activity (Ma et al. 2018). However, upon mutation of this residue in Mors1, the activity is completely lost. The reason behind this phenomenon could be that the side chain of Phe is blocking the catalytic pocket, preventing substrate access. On the other hand, Austin et al. published reported a variant of *IsPETase* (W159H) that decreased PET crystallinity as well as slightly increased the activity (Austin et al. 2018). In addition, another work showed that this mutation also increased the thermostability (Meng et al., 2021). In the case of Mors1, there is a loss of activity of almost 90%. One hypothesis to explain this may be that the His generates electrostatic repulsions with the substrate which is highly hydrophobic. Another possibility is that Trp could be making π - π interactions with the substrate that have disappeared with this mutation.

None of the variants produced changes in thermostability of more than 1.5 °C, as expected, since these changes had not been reported in *IsPETase* as modifiers of thermal stability. However, it was noticeable that the thermostability of Mors1 increased by 5.3 °C when changing the buffer from HEPES pH 7.5 to sodium phosphate pH 8.0. This buffer had already been reported in a previous publication to be beneficial for enzyme activity (Schmidt et al., 2016).

To explore the importance of the flexibility of the active center of Mors1 in its activity at low temperatures, a chimeric variant (CM) was designed in which the region 262-276 of the active site, which comprises the

so-called extended loop (271-275) was substituted for the homologous region of the thermophilic enzyme LCC. Upon insertion of this region, the disulfide bridge of the active center of Mors1 was lost, leading to a total loss of enzyme activity when assayed with PCL. However, restoring this disulfide bridge loop with the CM^{266C} mutant also restore its polyesterase activity, being equal to that of WT at 25 °C for PCL. This accounts for the enormous importance of this disulfide bridge in stabilizing the active center and the integrity of the catalytic triad in the enzymes adapted to low and moderate temperatures. This phenomenon was previously reported in *IsPETase*, in which mutations of these Cys to Ser resulted in variants with little or no activity (Han et al. 2017). Similarly, when mutated for Ala the variants completely lost their activity for BHET and reduced their activity by about 80% against PET films (Joo et al. 2018). Also, MD simulations revealed that the mean distance of the hydrogen bonds between the residues of the catalytic triad (Asp and His and His and Ser) when the disulfide bridge is reduced, increased around 0.4 Å, compromising the integrity of the catalytic triad (Fecker et al. 2018).

This destabilization of the active center in *IsPETase* also led to a reduction in thermostability of 13.2 °C (Joo et al. 2018), which is not observed in CM. The lack of the disulfide bridge in CM variant does not affect overall thermostability. This could be explained by the fact that many psychrophilic enzymes show greater flexibility only in the active site, while the other regions not involved in catalysis maintain their rigidity. Therefore, local destabilization of the active center would not affect the overall stability.

To explore the possible changes in flexibility in the active site of the variant CM^{266C}, MD simulations were performed with a homology model created through the same protocol used for the Mors1 model. We hypothesized that replacing the high mobility region comprising residues 262-276 of Mors1 for the homologous region in the thermophilic LCC would increase local stability, maintaining the integrity of the catalytic triad at higher temperatures. This would explain why we observed more than 4-fold increase in CM^{266C} activity relative to Mors1 that could not be explained by the sequence identity of the loop, because in this case, we should also see an increase in CM^{266C} activity at 25 °C relative to Mors1 and this is not the

case. Analyzing the per-residue RMSF of the 1000 ns replicates at 25 °C, CM^{A266C} showed a slightly reduced flexibility compared to Mors1. This could explain why CM^{A266C} shows enhanced activity at higher temperatures, as the movement of this region would be restricted, keeping the active center stabilized. Likewise, the lower activity of CM at 25 °C could be explained by the same phenomenon: as it has less flexibility than Mors1, the activation energy required for catalysis would be higher, therefore, the activity is lower. However, we believe that it would be necessary to carry out these simulations with crystallographic structures to corroborate this hypothesis.

To measure the hydrolysis activity of PCL in a quantitative and rapid way, crude extracts containing the enzyme Mors1 were used. It was observed that it is possible to measure PCL degradation directly from these extracts without the need to purify the protein. This can be used to develop a screening method later to characterize many variants. To compare the activity of the different crude extracts, it is first necessary to quantify the amount of recombinant protein in each sample, which depends on the level of expression in each culture. To normalize the enzymatic activity by the amount of recombinant protein, we propose the use of vectors with fluorescent GFP protein so that protein concentration and activity can be determined in a 96-well format.

When thinking about energetic and cost-effective biological PET recycling processes, the ideal is to think of processes that can be carried out at ambient or moderate temperatures. However, the enzymatic reaction rates are strongly conditioned by the mobility of the polymer chains. At temperatures close to T_g , the probability of the chains interacting with the active center of the enzyme is higher.

Although mesophilic and psychrophilic enzymes can degrade PET at temperatures well below T_g (~ 65 °C), their activity is very limited when compared to the activity of thermophiles at temperatures close to T_g . Studies on *IsPETase* to improve activity at moderate temperatures (30 °C to 40 °C) have not yielded very promising results. Likewise, the mutations carried out in Mors1 in this work to improve activity at 25 °C

have not been fruitful. For this reason, to obtain competitive enzymes, it seems necessary to increase the reaction temperature over 30 - 40 °C.

Currently, there are two approaches to obtain PET degrading enzymes with improved thermostability. One is to increase the thermostability of the thermophilic enzymes as much as possible. However, at temperatures around 75 °C, the transition of the polymer microstructure from a less ordered amorphous state to a non-degradable crystalline state can occur significantly earlier and faster, which would compete with enzymatic depolymerization and thus becomes the main determinant of the total level of degradation achievable (Wei et al. 2022).

Another strategy has focused on increasing the thermostability of *IsPETase*, and while this has been substantially achieved reaching a T_m up to 82.5 °C (Son et al. 2019; Bell et al. 2021; Cui et al. 2021) the activity has never exceeded the activity of thermophilic LCC or PHL7. However, recent work has come to change this paradigm. A modification of only 5 residues in *IsPETase* using deep learning strategies has resulted in a variant that is equally active at 50 °C as LCC^{ICCM} at 70° (Lu et al. 2021).

Variants obtained with deep learning techniques such as MutCompute (Lu et al. 2021) and GRAPE (Sun et al. 2021; Cui et al. 2021) have been shown to be more effective in increasing stability and activity than rational approaches (Han et al. 2017; Ma et al. 2018; Joo et al. 2018; Son et al. 2019; Brott et al. 2021).

Based on the above, the question then focuses on what would be the lowest temperature at which optimal enzymatic activity is obtained. We believe that by means of deep learning strategies, such as the one mentioned above, these mesophilic and psychrophilic enzymes could be used as templates for mutations to improve the thermostability and thus the activity to levels even higher than those reported for thermophiles at temperatures below the T_g .

The thermophilic polyester hydrolase LCC (PDB: 6EB0), first described by Sulaiman (Sulaiman et al. 2012) found in a compost pile, has been the enzyme with the highest specific activity on PET reported so

far. However, recently, another metagenomic enzyme from a compost sample, PHL7, has outperformed LCC presenting more than 1.6-fold higher catalytic activity (Sonnendecker et al. 2022). In this scenario, the study of the differences in the interactions between PHL7 and LCC residues with PET is of great interest. To identify the binding residues of the catalytic pocket of PHL7 and LCC we performed docking studies with the model substrate 1,2- ethylene-mono-terephthalate-mono (2-hydroxyethyl terephthalate (EMT), MHET and TPA. The 100 docked structures that presented the lowest free energy of binding were selected and grouped in 3 clusters based on structural similarity (RMSD). Every cluster represented a distinctive binding mode. The cluster in which the terephthalic ring of the EMT, MHET or TPA was in the same position as the terephthalic ring of the TPA in *IsPETase* co-crystal structure, was selected. However, the cluster selected (cluster 2) was not the most populated in the case of PHL7 nor LCC. This means that the majority of the most stable structures adopted a conformation which is not the one observed experimentally. This could be related to the number of structures chosen to clusterize (100 structures). A reduced number might have shown a different distribution between clusters.

From the 5 lowest binding energy structures with EMT the total binding free energies ($\Delta\Delta G$) were calculated. Similar values were obtained for PHL7 and LCC, however, when analyzing the binding free energy per residue, significant differences were observed between both enzymes. Of particular interest is the Leu in position 210 in PHL7, which is substituted by a Phe in LCC. This residue has been experimentally demonstrated to be crucial for PHL7 activity. When this residue is mutated to Phe, the enzyme significantly decreased its activity. Moreover, when this Phe is mutated to Leu in the homologous enzyme, PHL3, the activity increases to the level of PHL7 (Sonnendecker et al. 2021). The docking results showed that Leu210 in PHL7 has a negligible contribution to the binding, opposite to Phe243 in LCC that has a significant contribution. A hypothesis to explain this phenomenon, based on the experimental and computational results, could be that the aromatic ring of Phe243 makes π - π interactions with the aromatic ring of the moiety of EMT located in the subsite II hindering the product releasing or making the binding to the

substrate very stable. Therefore, either the EMT or its products could remain longer attached to the binding pocket causing a decrease in the catalytic activity. Experimental studies would be necessary to confirm this hypothesis. A substrate similar to MHET that binds only to the subsite II (because MHET binds to subsite I) could be used as an inhibitor. If this hypothesis is correct, a decrease in the enzymatic activity of LCC in presence of this molecule would be expected but not for PHL7.

Similar results were obtained for *IsPETase*, where the aromatic ring of 2PET showed a higher interaction to residues F243 in LCC and F209 in *TfCut2*, whereas the equivalent Ser residue (S211) in *IsPETase* did not show binding free energy (Fecker et al. 2018). In fact, a substitution of Ser211 for Ala in *IsPETase* did not decrease the BHET and PET hydrolytic activity of the enzyme (Joo et al. 2018), suggesting that this residue is not playing a role in the binding.

To elucidate the binding mode of PET to these enzymes, co-crystallographic structures are necessary. The available co-structures are limited to HEMT (Han et al. 2017) and more recently, to MHET (Zeng et al. 2022), however, there are no structures with longer substrates.

Conclusions

The aim of this thesis was to identify and characterize cold-adapted PET hydrolases and improve their activity through protein engineering. To this end, we studied two protein sequences from Antarctic marine bacteria that were similar in sequence to the mesophilic PET-hydrolase *IsPETase*. We hypothesized that cold-adapted enzymes, having a more flexible active center, could compensate for the rigidity of PET at moderate temperatures and thus show competitive catalytic activity.

For this purpose, in chapter III.I, the enzymes encoded by these Antarctic sequences were functionally characterized against PET and PCL as substrates and their thermostability were determined. Next, the enzyme with the best catalytic activity, Mors1, was structurally studied by creating a three-dimensional model and its flexibility was assessed by MD simulations. Upon confirmation of its PET-degrading activity, we further identified potential new PET hydrolases in Antarctic coastal metagenomes and determine their abundance and taxonomy. In chapter III.II, single point mutations as well as a loop swapping were made in the active site of Mors1 to improve the catalytic activity and to study the role of flexibility in PET catalysis. Additionally, in chapter III.III we characterized the PET binding mode of a recently described new thermophilic PET-hydrolase by docking studies as part of an ongoing collaboration.

The results showed that Mors1 and OaCut are polyester hydrolases capable of degrading the synthetic polyesters PET and PCL at room temperature, being the first cold-adapted PET hydrolases described to date. These enzymes are active at temperatures close to room temperature, and they unfold at temperatures close to 50 °C. Mors1 presents an optimal activity at 25 °C and its catalytic activity against PET is similar to *IsPETase*. Its structure is consistent with an $\alpha\beta$ hydrolase-type fold, consisting of nine β -sheets surrounded by six α -helix, common to the other PET-degrading enzymes described to date.

The presence of a disulfide bridge in the vicinity of the catalytic pocket (DB2), previously observed in *IsPETase* has been shown to be key to the structural integrity of the active site (Fecker et al. 2018). When

this disulfide bridge is removed in Mors1, the enzymatic activity is completely lost, indicating the enormous importance of this bond for catalysis. Moreover, Mors1 presents an additional disulfide bridge in the N-terminus (DB1), absent in the other mesophilic and thermophilic homologues. However, homologous sequences to Mors1 found in marine metagenomes also present Cys in the same positions as Mors1, which could indicate that this disulfide bridge is a thermal adaptation strategy.

The aminoacidic composition of the active site of Mors1 (subsite I, II and extended loop) does not fall into the established categories of PET hydrolases type I and II (Joo et al. 2018) and could therefore constitute a new category, suggesting that the repertoire of PET-hydrolases is more diverse than currently considered. Moreover, Mors1 shows greater structural flexibility than *IsPETase*, especially in the loops that conform the active site where the catalytic residues or residues implied in binding are located, a typical feature of cold-adapted enzymes. Insertion of a loop of a thermophilic enzyme increases its activity at higher temperatures and decreases it at lower temperatures. This seems to be due to a reduction of the flexibility which allowed the enzyme to better withstand higher temperatures without destabilizing the active center.

Analysis of metagenomic samples revealed the presence of homologous sequences to Mors1 belonging to the family Moraxellaceae, with the high abundance of members of the Moraxellaceae family in marine samples in contrast to the low abundance of Mors1 homologous sequences suggesting that these sequences are only present in some members of this family.

Beyond the discovery of Antarctic PET hydrolases, we participated on the characterization of the recently discovered thermophilic enzyme PHL7, with a thermostability of 79.1 °C, which outperformed all previously described PET hydrolases. At 70 °C, its activity was approximately 1.6 times higher than LCC and 50 times better than *IsPETase*. Leu in position 210 appears to be a key residue for catalytic activity: when mutated by Phe its activity is reduced by 60%, and when this residue is incorporated in homologous enzymes that present a Phe its activity increases almost to the level of PHL7 (Sonnendecker et al. 2021).

Computational docking studies performed with the substrate 1,2-ethylene-mono-terephthalate-mono(2-hydroxyethyl terephthalate) (EMT) revealed that Leu 210 in PHL7 has a lower interaction with the substrate than the homologous Phe in LCC (F243) which could indicate that F243 in LCC interacts with the substrate or reaction product hindering its release. However, it would be necessary to contrast this information with functional studies with an aromatic molecule that binds to subunit II of the enzyme to see if activity is inhibited.

In conclusion, the results obtained in this thesis showed that the increased flexibility of the active center of cold-adapted enzymes, although it enhances the degradation activity of PET at low temperatures, it remains lower than the activity of the thermophilic counterparts at elevated temperatures. Therefore, the flexibility of the active site cannot compensate for the rigidity of PET at low temperatures for efficient hydrolysis, which would lead to reject the original hypothesis. On the contrary, it seems that catalytic rate is more conditioned by the mobility of the polymeric chains than by the flexibility of the active site, so it would be essential to use temperatures higher than room temperature to achieve high catalytic activities.

However, the temperature at which these reaction can be performed is not established yet, as recently demonstrated, high catalytic activities can be achieved below the glass transition temperature of PET (Bell et al. 2021). Mutations designed by deep learning techniques seem the most promising strategy for modifying activity and thermostability. We believe that modification of mesophilic or psychrophilic PET degrading enzymes by this technique could result in biocatalysts with high activities below 65 °C.

References

- Alarcón-Schumacher T, Guajardo-Leiva S, Antón J, Díez B (2019) Elucidating Viral Communities During a Phytoplankton Bloom on the West Antarctic Peninsula. *Front Microbiol* 10: . <https://doi.org/10.3389/fmicb.2019.01014>
- Alcamán-Arias ME, Farías L, Verdugo J, Alarcón-Schumacher T, Díez B (2018) Microbial activity during a coastal phytoplankton bloom on the Western Antarctic Peninsula in late summer. *FEMS Microbiol Lett* 365: . <https://doi.org/10.1093/femsle/fny090>
- Alexander NS, Preininger AM, Kaya AI, Stein RA, Hamm HE, Meiler J (2013) Energetic analysis of the rhodopsin–G-protein complex links the $\alpha 5$ helix to GDP release. *Nat Struct Mol Biol* 21:56–63 . <https://doi.org/10.1038/nsmb.2705>
- Almagro Armenteros JJ, Tsirigos KD, Sønderby CK, Petersen TN, Winther O, Brunak S, von Heijne G, Nielsen H (2019) SignalP 5.0 improves signal peptide predictions using deep neural networks. *Nat Biotechnol* 37:420–423 . <https://doi.org/10.1038/s41587-019-0036-z>
- Anandakrishnan R, Aguilar B, Onufriev A V. (2012) H++ 3.0: automating pK prediction and the preparation of biomolecular structures for atomistic molecular modeling and simulations. *Nucleic Acids Res* 40:W537–W541 . <https://doi.org/10.1093/nar/gks375>
- Arnold FH (1996) Directed evolution: Creating biocatalysts for the future. *Chem Eng Sci* 51:5091–5102 . [https://doi.org/10.1016/S0009-2509\(96\)00288-6](https://doi.org/10.1016/S0009-2509(96)00288-6)
- Austin HP, Allen MD, Donohoe BS, Rorrer NA, Kearns FL, Silveira RL, Pollard BC, Dominick G, Duman R, El Omari K, Mykhaylyk V, Wagner A, Michener WE, Amore A, Skaf MS, Crowley MF, Thorne AW, Johnson CW, Woodcock HL, McGeehan JE, Beckham GT (2018) Characterization and engineering of a plastic-degrading aromatic polyesterase. *Proc Natl Acad Sci* 115:E4350–E4357 . <https://doi.org/10.1073/pnas.1718804115>
- Balani K, Verma V, Agarwal A, Narayan R (2015) Physical, Thermal, and Mechanical Properties of Polymers. In: *Biosurfaces*. John Wiley & Sons, Inc, Hoboken, NJ, USA, pp 329–344
- Bankevich A, Nurk S, Antipov D, Gurevich AA, Dvorkin M, Kulikov AS, Lesin VM, Nikolenko SI, Pham S, Prjibelski AD, Pyshkin A V, Sirotkin A V, Vyahhi N, Tesler G, Alekseyev MA, Pevzner PA (2012) SPAdes: A New Genome Assembly Algorithm and Its Applications to Single-Cell Sequencing. *J Comput Biol* 19:455–477 . <https://doi.org/10.1089/cmb.2012.0021>
- Barth M, Oeser T, Wei R, Then J, Schmidt J, Zimmermann W (2015) Effect of hydrolysis products on the enzymatic

- degradation of polyethylene terephthalate nanoparticles by a polyester hydrolase from *Thermobifida fusca*. *Biochem Eng J* 93:222–228 . <https://doi.org/10.1016/j.bej.2014.10.012>
- Bartnikowski M, Dargaville TR, Ivanovski S, Hutmacher DW (2019) Degradation mechanisms of polycaprolactone in the context of chemistry, geometry and environment. *Prog Polym Sci* 96:1–20 . <https://doi.org/10.1016/j.progpolymsci.2019.05.004>
- Belisário-Ferrari MR, Wei R, Schneider T, Honak A, Zimmermann W (2019) Fast Turbidimetric Assay for Analyzing the Enzymatic Hydrolysis of Polyethylene Terephthalate Model Substrates. *Biotechnol J* 14:10–14 . <https://doi.org/10.1002/biot.201800272>
- Belisário-Ferrari MR, Wei R, Schneider T, Honak A, Zimmermann W (2018) Fast turbidimetric assay for analyzing the enzymatic hydrolysis of polyethylene terephthalate model substrates. *Biotechnol J* 1800272 . <https://doi.org/10.1002/biot.201800272>
- Bell EL, Smithson R, Kilbride S, Foster J, Hardy F, Ramachandran S, Tedstone AB, Haigh SJ, Garforth AB, R Day J PJ, Levy C, Shaver MP, Green AP (2021) Directed evolution of an efficient and thermostable PET depolymerase. *ChemRxiv*
- Bell EW, Zhang Y (2019) DockRMSD: An open-source tool for atom mapping and RMSD calculation of symmetric molecules through graph isomorphism. *J Cheminform.* <https://doi.org/10.1186/s13321-019-0362-7>
- Bender BJ, Cisneros A, Duran AM, Finn JA, Fu D, Lokits AD, Mueller BK, Sangha AK, Sauer MF, Sevy AM, Sliwoski G, Sheehan JH, DiMaio F, Meiler J, Moretti R (2016) Protocols for Molecular Modeling with Rosetta3 and RosettaScripts. *Biochemistry* 55:4748–4763 . <https://doi.org/10.1021/acs.biochem.6b00444>
- Bengtsson-Palme J, Hartmann M, Eriksson KM, Pal C, Thorell K, Larsson DGJ, Nilsson RH (2015) metaxa2: improved identification and taxonomic classification of small and large subunit rRNA in metagenomic data. *Mol Ecol Resour* 15:1403–1414 . <https://doi.org/10.1111/1755-0998.12399>
- Berman HM, Westbrook J, Feng Z, Gilliland G, Bhat TN, Weissig H, Shindyalov IN, Bourne PE (2000) The Protein Data Bank. *Nucleic Acids Res.* 28:235–242
- Bollinger A, Thies S, Knieps-Grünhagen E, Kobus S, Höppner A, Smits SH, Ferrer M, Jaeger K (2020) A novel polyester hydrolase from the marine bacterium *Pseudomonas aestusnigri* -structural and functional insights. *Front Microbiol Accepted* . <https://doi.org/10.3389/fmicb.2020.00114>
- Bornscheuer UT, Huisman GW, Kazlauskas RJ, Lutz S, Moore JC, Robins K (2012) Engineering the third wave of biocatalysis. *Nature* 485:185–194 . <https://doi.org/10.1038/nature11117>
- Botterell ZLR, Beaumont N, Dorrington T, Steinke M, Thompson RC, Lindeque PK (2019) Bioavailability and effects of microplastics on marine zooplankton: A review. *Environ Pollut* 245:98–110 . <https://doi.org/10.1016/j.envpol.2018.10.065>

- Boyle NMO, Banck M, James CA, Morley C, Vandermeersch T, Hutchison GR (2011) Open Babel: An open chemical toolbox. 1–14
- Bradford MM (1976) A rapid and sensitive method for the quantitation of microgram quantities of protein utilizing the principle of protein-dye binding. *Anal Biochem* 72:248–254 . [https://doi.org/10.1016/0003-2697\(76\)90527-3](https://doi.org/10.1016/0003-2697(76)90527-3)
- Brott S, Pfaff L, Schuricht J, Schwarz J, Böttcher D, Badenhorst CPS, Wei R, Bornscheuer UT (2021) Engineering and evaluation of thermostable Is PETase variants for PET degradation. *Eng Life Sci* 1–12 . <https://doi.org/10.1002/elsc.202100105>
- Calhoun A (2016) Polypropylene. In: *Multilayer Flexible Packaging*. Elsevier, pp 35–45
- Carniel A, Valoni É, Nicomedes J, Gomes A da C, Castro AM De (2017) Lipase from *Candida antarctica* (CALB) and cutinase from *Humicola insolens* act synergistically for PET hydrolysis to terephthalic acid. *Process Biochem* 59:84–90 . <https://doi.org/10.1016/j.procbio.2016.07.023>
- Carter P (1986) Site-directed mutagenesis. *Biochem J* 237:1–7 . <https://doi.org/10.1042/bj2370001>
- Chen C-C, Han X, Li X, Jiang P, Niu D, Ma L, Liu W, Li S, Qu Y, Hu H, Min J, Yang Y, Zhang L, Zeng W, Huang J-W, Dai L, Guo R-T (2021) General features to enhance enzymatic activity of poly(ethylene terephthalate) hydrolysis. *Nat Catal* 4:425–430 . <https://doi.org/10.1038/s41929-021-00616-y>
- Chen CC, Han X, Ko TP, Liu W, Guo RT (2018) Structural studies reveal the molecular mechanism of PETase. *FEBS J* 285:3717–3723 . <https://doi.org/10.1111/febs.14612>
- Chen JY, Ou CF, Hu YC, Lin CC (1991) Depolymerization of poly(ethylene terephthalate) resin under pressure. *J Appl Polym Sci* 42:1501–1507 . <https://doi.org/10.1002/app.1991.070420603>
- Chen S, Su L, Chen J, Wu J (2013) Cutinase: Characteristics, preparation, and application. *Biotechnol Adv* 31:1754–1767 . <https://doi.org/10.1016/j.biotechadv.2013.09.005>
- Chen S, Tong X, Woodard RW, Du G, Wu J, Chen J (2008) Identification and Characterization of Bacterial Cutinase. *J Biol Chem* 283:25854–25862 . <https://doi.org/10.1074/jbc.M800848200>
- Chica RA, Doucet N, Pelletier JN (2005) Semi-rational approaches to engineering enzyme activity: combining the benefits of directed evolution and rational design. *Curr Opin Biotechnol* 16:378–384 . <https://doi.org/10.1016/j.copbio.2005.06.004>
- Cózar A, Martí E, Duarte CM, García-de-Lomas J, van Sebille E, Ballatore TJ, Eguíluz VM, González-Gordillo JI, Pedrotti ML, Echevarría F, Troublè R, Irigoien X (2017) The Arctic Ocean as a dead end for floating plastics in the North Atlantic branch of the Thermohaline Circulation. *Sci Adv* 3:1–9 . <https://doi.org/10.1126/sciadv.1600582>

- Crawford CB, Quinn B (2017) Physiochemical properties and degradation. In: *Microplastic Pollutants*. Elsevier, pp 57–100
- Cui Y, Chen Y, Liu X, Dong S, Tian Y, Qiao Y, Mitra R, Han J, Li C, Han X, Liu W, Chen Q, Wei W, Wang X, Du W, Tang S, Xiang H, Liu H, Liang Y, Houk KN, Wu B (2021) Computational Redesign of a PETase for Plastic Biodegradation under Ambient Condition by the GRAPE Strategy. *ACS Catal* 11:1340–1350 . <https://doi.org/10.1021/acscatal.0c05126>
- D'Amico S, Marx J-C, Gerday C, Feller G (2003) Activity-Stability Relationships in Extremophilic Enzymes. *J Biol Chem* 278:7891–7896 . <https://doi.org/10.1074/jbc.M212508200>
- Danso D, Schmeisser C, Chow J, Zimmermann W, Wei R, Leggewie C, Li X, Hazen T, Streit WR (2018) New Insights into the Function and Global Distribution of Polyethylene Terephthalate (PET)-Degrading Bacteria and Enzymes in Marine and Terrestrial Metagenomes. *Appl Environ Microbiol* 84:1–13 . <https://doi.org/10.1128/AEM.02773-17>
- Darden T, York D, Pedersen L (1993) Particle mesh Ewald: An $N \cdot \log(N)$ method for Ewald sums in large systems. *J Chem Phys* 98:10089–10092 . <https://doi.org/10.1063/1.464397>
- De Maayer P, Anderson D, Cary C, Cowan DA (2014) Some like it cold: understanding the survival strategies of psychrophiles. *EMBO Rep* 15:508–517 . <https://doi.org/10.1002/embr.201338170>
- Dong X, Xing T, Chen G (2020) Improving the anti-pilling performance of cellulose fiber blended knitted fabrics with 2,4,6-trichloropyrimidine treatment. *Coatings* 10:1–16 . <https://doi.org/10.3390/coatings10100969>
- Doppalapudi S, Jain A, Khan W, Domb AJ (2014) Biodegradable polymers-an overview. *Polym Adv Technol* 25:427–435 . <https://doi.org/10.1002/pat.3305>
- Eftink MR, Ghiron CA (1975) Dynamics of a protein matrix revealed by fluorescence quenching. *Proc Natl Acad Sci U S A* 72:3290–3294 . <https://doi.org/10.1073/pnas.72.9.3290>
- Eisenberg D, Lüthy R, Bowie JU (1997) [20] VERIFY3D: Assessment of protein models with three-dimensional profiles. In: *Methods in enzymology*. pp 396–404
- Fecker T, Galaz-Davison P, Engelberger F, Narui Y, Sotomayor M, Parra LP, Ramírez-Sarmiento CA (2018) Active Site Flexibility as a Hallmark for Efficient PET Degradation by *I. sakaiensis* PETase. *Biophys J* 114:1302–1312 . <https://doi.org/10.1016/j.bpj.2018.02.005>
- Feller G (2013) Psychrophilic Enzymes: From Folding to Function and Biotechnology. *Scientifica (Cairo)* 2013:1–28 . <https://doi.org/10.1155/2013/512840>
- Feller G, Gerday C (2003) Psychrophilic enzymes: hot topics in cold adaptation. *Nat Rev Microbiol* 1:200–208 . <https://doi.org/10.1038/nrmicro773>

- Ford H V., Jones NH, Davies AJ, Godley BJ, Jambeck JR, Napper IE, Suckling CC, Williams GJ, Woodall LC, Koldewey HJ (2022) The fundamental links between climate change and marine plastic pollution. *Sci Total Environ* 806:150392 . <https://doi.org/10.1016/j.scitotenv.2021.150392>
- Fournier SB, D'Errico JN, Adler DS, Kollontzi S, Goedken MJ, Fabris L, Yurkow EJ, Stapleton PA (2020) Nanopolystyrene translocation and fetal deposition after acute lung exposure during late-stage pregnancy. *Part Fibre Toxicol* 17:1–11 . <https://doi.org/10.1186/s12989-020-00385-9>
- Frank R, Krinke D, Sonnendecker C, Zimmermann W, Jahnke H-G (2022) Real-Time Noninvasive Analysis of Biocatalytic PET Degradation. *ACS Catal* 12:25–35 . <https://doi.org/10.1021/acscatal.1c03963>
- Fujisawa M, Hirofumi H, Nishida T (2001) Degradation of polyethylene and nylon-66 by the laccase-mediator system. *J Polym Environ* 9:103–108 . <https://doi.org/10.1023/A:1020472426516>
- Furukawa M, Kawakami N, Oda K, Miyamoto K (2018) Acceleration of Enzymatic Degradation of Poly(ethylene terephthalate) by Surface Coating with Anionic Surfactants. *ChemSusChem* 11:4018–4025 . <https://doi.org/10.1002/cssc.201802096>
- Gad SE (2014) Polymers. In: *Encyclopedia of Toxicology*. Elsevier, pp 1045–1050
- Galeski A (2003) Strength and toughness of crystalline polymer systems. *Prog Polym Sci* 28:1643–1699 . <https://doi.org/10.1016/j.progpolymsci.2003.09.003>
- Garcia JM, Robertson ML (2017) The future of plastics recycling. *Science* (80-) 358:870–872 . <https://doi.org/10.1126/science.aag0324>
- Geyer R, Jambeck JR, Law KL (2017) Production, use, and fate of all plastics ever made. *Sci Adv* 3:25–29 . <https://doi.org/10.1126/sciadv.1700782>
- Ghisaidoobe A, Chung S (2014) Intrinsic Tryptophan Fluorescence in the Detection and Analysis of Proteins: A Focus on Förster Resonance Energy Transfer Techniques. *Int J Mol Sci* 15:22518–22538 . <https://doi.org/10.3390/ijms151222518>
- Grigoriev YN, Ibragimov NH, Kovalev VF, Meleshko S V. (2008) *Computational Many-Particle Physics*. Springer Berlin Heidelberg, Berlin, Heidelberg
- Gu Y, Li DW, Brüschweiler R (2015) Decoding the mobility and time scales of protein loops. *J Chem Theory Comput* 11:1308–1314 . <https://doi.org/10.1021/ct501085y>
- Hadley Wickham (2016) *ggplot2: Elegant Graphics for Data Analysis*, 2nd Editio. Springer-Verlag New York
- Hamilton LA, Feit S, Muffet C, Kelso M, Rubright SM, Bernhardt C, Schaeffer E, Moon D, Morris J, Labbe-Bellas R (2019) Plastic & Climate: The hidden costs of a plastic planet. CIEL, Earthworks, GAIA, HBBF, IPEN, t.e.j.a.s, Upstream, Break 1–108

- Han X, Liu W, Huang J-W, Ma J, Zheng Y, Ko T-P, Xu L, Cheng Y-S, Chen C-C, Guo R-T (2017) Structural insight into catalytic mechanism of PET hydrolase. *Nat Commun* 8:2106 . <https://doi.org/10.1038/s41467-017-02255-z>
- Herrero Acero E, Ribitsch D, Steinkellner G, Gruber K, Greimel K, Eiteljoerg I, Trotscha E, Wei R, Zimmermann W, Zinn M, Cavaco-Paulo A, Freddi G, Schwab H, Guebitz G (2011) Enzymatic Surface Hydrolysis of PET: Effect of Structural Diversity on Kinetic Properties of Cutinases from *Thermobifida*. *Macromolecules* 44:4632–4640 . <https://doi.org/10.1021/ma200949p>
- Hooft RWW, Vriend G, Sander C, Abola EE (1996) Errors in protein structures [3]. *Nature* 381:272
- Hottle TA, Bilec MM, Landis AE (2013) Sustainability assessments of bio-based polymers. *Polym Degrad Stab* 98:1898–1907 . <https://doi.org/10.1016/j.polymdegradstab.2013.06.016>
- Hyatt D, Chen G-L, LoCascio PF, Land ML, Larimer FW, Hauser LJ (2010) Prodigal: prokaryotic gene recognition and translation initiation site identification. *BMC Bioinformatics* 11:119 . <https://doi.org/10.1186/1471-2105-11-119>
- Ishida T, Kinoshita K (2007) PrDOS: prediction of disordered protein regions from amino acid sequence. *Nucleic Acids Res* 35:W460–W464 . <https://doi.org/10.1093/nar/gkm363>
- Jaeger K-E, Dijkstra BW, Reetz MT (1999) Bacterial Biocatalysts: Molecular Biology, Three-Dimensional Structures, and Biotechnological Applications of Lipases. *Annu Rev Microbiol* 53:315–351 . <https://doi.org/10.1146/annurev.micro.53.1.315>
- Jambeck JR, Geyer R, Wilcox C, Siegler TR, Perryman M, Andrady A, Narayan R, Law KL (2015) Plastic waste inputs from land into the ocean. *Science* (80-) 347:768–771 . <https://doi.org/10.1126/science.1260352>
- Jin H, Ma T, Sha X, Liu Z, Zhou Y, Meng X, Chen Y, Han X, Ding J (2021) Polystyrene microplastics induced male reproductive toxicity in mice. *J Hazard Mater* 401:123430 . <https://doi.org/10.1016/j.jhazmat.2020.123430>
- Joo S, Cho IJ, Seo H, Son HF, Sagong H-Y, Shin TJ, Choi SY, Lee SY, Kim K-J (2018) Structural insight into molecular mechanism of poly(ethylene terephthalate) degradation. *Nat Commun* 9:382 . <https://doi.org/10.1038/s41467-018-02881-1>
- Kassambara, A. and Mundt F (2020) Factoextra: Extract and Visualize the Results of Multivariate Data Analyses. R Package Version 1.0.7. <https://cran.r-project.org/package=factoextra>
- Kawai F, Oda M, Tamashiro T, Waku T, Tanaka N, Yamamoto M, Mizushima H, Miyakawa T, Tanokura M (2014) A novel Ca²⁺-activated, thermostabilized polyesterase capable of hydrolyzing polyethylene terephthalate from *Saccharomonospora viridis* AHK190. *Appl Microbiol Biotechnol* 98:10053–10064 . <https://doi.org/10.1007/s00253-014-5860-y>
- Kirley TL (1989) Reduction and fluorescent labeling of cyst(e)ine-containing proteins for subsequent structural

- analyses. *Anal Biochem* 180:231–236 . [https://doi.org/10.1016/0003-2697\(89\)90422-3](https://doi.org/10.1016/0003-2697(89)90422-3)
- Kube M, Chernikova TN, Al-Ramahi Y, Beloqui A, Lopez-Cortez N, Guazzaroni M-E, Heipieper HJ, Klages S, Kotsyurbenko OR, Langer I, Nechitaylo TY, Lünsdorf H, Fernández M, Juárez S, Ciordia S, Singer A, Kagan O, Egorova O, Petit PA, Stogios P, Kim Y, Tchigvintsev A, Flick R, Denaro R, Genovese M, Albar JP, Reva ON, Martínez-Gomariz M, Tran H, Ferrer M, Savchenko A, Yakunin AF, Yakimov MM, Golyshina O V, Reinhardt R, Golyshin PN (2013) Genome sequence and functional genomic analysis of the oil-degrading bacterium *Oleispira antarctica*. *Nat Commun* 4:2156 . <https://doi.org/10.1038/ncomms3156>
- Lacerda AL d. F, Rodrigues L dos S, van Sebille E, Rodrigues FL, Ribeiro L, Secchi ER, Kessler F, Proietti MC (2019) Plastics in sea surface waters around the Antarctic Peninsula. *Sci Rep* 9:3977 . <https://doi.org/10.1038/s41598-019-40311-4>
- Langmead B, Salzberg SL (2012) Fast gapped-read alignment with Bowtie 2. *Nat Methods* 9:357–359 . <https://doi.org/10.1038/nmeth.1923>
- Laskowski RA, MacArthur MW, Moss DS, Thornton JM (1993) PROCHECK: a program to check the stereochemical quality of protein structures. *J Appl Crystallogr* 26:283–291 . <https://doi.org/10.1107/s0021889892009944>
- Leaver-Fay A, Tyka M, Lewis SM, Lange OF, Thompson J, Jacak R, Kaufman K, Renfrew PD, Smith CA, Sheffler W, Davis IW, Cooper S, Treuille A, Mandell DJ, Richter F, Ban YEA, Fleishman SJ, Corn JE, Kim DE, Lyskov S, Berrondo M, Mentzer S, Popović Z, Havranek JJ, Karanicolas J, Das R, Meiler J, Kortemme T, Gray JJ, Kuhlman B, Baker D, Bradley P (2011) Rosetta3: An object-oriented software suite for the simulation and design of macromolecules. *Methods Enzymol* 487:545–574 . <https://doi.org/10.1016/B978-0-12-381270-4.00019-6>
- Lemmon G, Meiler J (2012) Rosetta ligand docking with flexible XML protocols. *Methods Mol Biol* 819:143–155 . https://doi.org/10.1007/978-1-61779-465-0_10
- Lenfant N, Hotelier T, Bourne Y, Marchot P, Chatonnet A (2013) Proteins with an alpha/beta hydrolase fold: Relationships between subfamilies in an ever-growing superfamily. *Chem Biol Interact* 203:266–268 . <https://doi.org/10.1016/j.cbi.2012.09.003>
- Li B, Ding Y, Cheng X, Sheng D, Xu Z, Rong Q, Wu Y, Zhao H, Ji X, Zhang Y (2020) Polyethylene microplastics affect the distribution of gut microbiota and inflammation development in mice. *Chemosphere* 244:125492 . <https://doi.org/10.1016/j.chemosphere.2019.125492>
- Lim X (2021) Microplastics are everywhere — but are they harmful? *Nature* 593:22–25 . <https://doi.org/10.1038/d41586-021-01143-3>
- Lonhienne T, Zoidakis J, Vorgias CE, Feller G, Gerday C, Bouriotis V (2001) Modular structure, local flexibility and cold-activity of a novel chitinase from a psychrophilic antarctic bacterium. *J Mol Biol* 310:291–297 .

<https://doi.org/10.1006/jmbi.2001.4774>

Lu H, Diaz DJ, Czarnecki NJ, Zhu C, Kim W, Shroff R, Acosta DJ, Alexander B, Cole H, Zhang YJ, Lynd N, Ellington AD, Alper HS (2021) Deep learning redesign of PETase for practical PET degrading applications. *bioRxiv* 2021.10.10.463845

Lu H, Diaz DJ, Czarnecki NJ, Zhu C, Kim W, Shroff R, Acosta DJ, Alexander BR, Cole HO, Zhang Y, Lynd NA, Ellington AD, Alper HS (2022) Machine learning-aided engineering of hydrolases for PET depolymerization. *Nature* 604:662–667 . <https://doi.org/10.1038/s41586-022-04599-z>

Lüthy R, Bowie JU, Eisenberg D (1992) Assessment of protein models with three-dimensional profiles. *Nature* 356:83–85 . <https://doi.org/10.1038/356083a0>

Ma Y, Yao M, Li B, Ding M, He B, Chen S, Zhou X, Yuan Y (2018) Enhanced Poly(ethylene terephthalate) Hydrolase Activity by Protein Engineering. *Engineering* 4:888–893 . <https://doi.org/10.1016/j.eng.2018.09.007>

Magrane M, Consortium U (2011) UniProt Knowledgebase: a hub of integrated protein data. *Database* 2011:bar009–bar009 . <https://doi.org/10.1093/database/bar009>

Maier JA, Martinez C, Kasavajhala K, Wickstrom L, Hauser KE, Simmerling C (2015) ff14SB: Improving the Accuracy of Protein Side Chain and Backbone Parameters from ff99SB. *J Chem Theory Comput* 11:3696–3713 . <https://doi.org/10.1021/acs.jctc.5b00255>

Marten E, Müller R-J, Deckwer W-D (2003) Studies on the enzymatic hydrolysis of polyesters I. Low molecular mass model esters and aliphatic polyesters. *Polym Degrad Stab* 80:485–501 . [https://doi.org/10.1016/S0141-3910\(03\)00032-6](https://doi.org/10.1016/S0141-3910(03)00032-6)

Mato Y, Isobe T, Takada H, Kanehiro H, Ohtake C, Kaminuma T (2001) Plastic Resin Pellets as a Transport Medium for Toxic Chemicals in the Marine Environment. *Environ Sci Technol* 35:318–324 . <https://doi.org/10.1021/es0010498>

McRee DE (1999) *Practical Protein Crystallography*. Academic Press

Meiler J, Baker D (2006) ROSETTALIGAND: Protein-small molecule docking with full side-chain flexibility. *Proteins Struct Funct Bioinforma* 65:538–548 . <https://doi.org/10.1002/prot.21086>

Meyer-Cifuentes IE, Werner J, Jehmlich N, Will SE, Neumann-Schaal M, Öztürk B (2020) Synergistic biodegradation of aromatic-aliphatic copolyester plastic by a marine microbial consortium. *Nat Commun* 11:5790 . <https://doi.org/10.1038/s41467-020-19583-2>

Mishra S, Goje A (2003) Kinetic and thermodynamic study of methanolysis of poly(ethylene terephthalate) waste powder. *Polym Int* 52:337–342 . <https://doi.org/10.1002/pi.1147>

Mohamed Nor NH, Kooi M, Diepens NJ, Koelmans AA (2021) Lifetime Accumulation of Microplastic in Children

- and Adults. *Environ Sci Technol* 55:5084–5096 . <https://doi.org/10.1021/acs.est.0c07384>
- Mueller R-J (2006) Biological degradation of synthetic polyesters—Enzymes as potential catalysts for polyester recycling. *Process Biochem* 41:2124–2128 . <https://doi.org/10.1016/j.procbio.2006.05.018>
- Mukai K, Yamada K, Doi Y (1993) Kinetics and mechanism of heterogeneous hydrolysis of poly[(R)-3-hydroxybutyrate] film by PHA depolymerases. *Int J Biol Macromol* 15:361–366 . [https://doi.org/10.1016/0141-8130\(93\)90054-P](https://doi.org/10.1016/0141-8130(93)90054-P)
- Mukherjee S, Kundu PP (2014) Alkaline fungal degradation of oxidized polyethylene in black liquor: Studies on the effect of lignin peroxidases and manganese peroxidases. *J Appl Polym Sci* 131:n/a-n/a . <https://doi.org/10.1002/app.40738>
- Müller R-J, Schrader H, Profe J, Dresler K, Deckwer W-D (2005) Enzymatic Degradation of Poly(ethylene terephthalate): Rapid Hydrolyse using a Hydrolase from *T. fusca*. *Macromol Rapid Commun* 26:1400–1405 . <https://doi.org/10.1002/marc.200500410>
- Nakagawa S, Marubayashi H, Nojima S (2015) Crystallization of polymer chains confined in nanodomains. *Eur Polym J* 70:262–275 . <https://doi.org/10.1016/j.eurpolymj.2015.07.018>
- Nakamiya K, Sakasita G, Ooi T, Kinoshita S (1997) Enzymatic degradation of polystyrene by hydroquinone peroxidase of *Azotobacter beijerinckii* HM121. *J Ferment Bioeng* 84:480–482 . [https://doi.org/10.1016/S0922-338X\(97\)82013-2](https://doi.org/10.1016/S0922-338X(97)82013-2)
- Nakamura A, Kobayashi N, Koga N, Iino R (2021) Positive Charge Introduction on the Surface of Thermostabilized PET Hydrolase Facilitates PET Binding and Degradation. *ACS Catal* 11:8550–8564 . <https://doi.org/10.1021/acscatal.1c01204>
- Narancic T, Verstichel S, Reddy Chaganti S, Morales-Gamez L, Kenny ST, De Wilde B, Babu Padamati R, O’Connor KE (2018) Biodegradable Plastic Blends Create New Possibilities for End-of-Life Management of Plastics but They Are Not a Panacea for Plastic Pollution. *Environ Sci Technol* 52:10441–10452 . <https://doi.org/10.1021/acs.est.8b02963>
- Nestl BM, Hauer B (2014) Engineering of Flexible Loops in Enzymes
- Nikolaivits E, Dimopoulou P, Maslak V, Nikodinovic-Runic J, Topakas E (2020) Discovery and biochemical characterization of a novel polyesterase for the degradation of synthetic plastics. *Chem Proc* 2:33 . <https://doi.org/10.3390/ECCS2020-07572>
- Noel JK, Onuchic JN (2012) The Many Faces of Structure-Based Potentials: From Protein Folding Landscapes to Structural Characterization of Complex Biomolecules. 31–54 . https://doi.org/10.1007/978-1-4614-2146-7_2
- Oliveira J, Belchior A, da Silva VD, Rotter A, Petrovski Ž, Almeida PL, Lourenço ND, Gaudêncio SP (2020) Marine Environmental Plastic Pollution: Mitigation by Microorganism Degradation and Recycling Valorization. *Front*

- Mar Sci 7: . <https://doi.org/10.3389/fmars.2020.567126>
- Ollis DL, Cheah E, Cygler M, Dijkstra B, Frolow F, Franken SM, Harel M, Remington SJ, Silman I, Schrag J, Sussman JL, Verschueren KHG, Goldman A (1992) The α / β hydrolase fold. *Protein Eng Des Sel* 5:197–211 . <https://doi.org/10.1093/protein/5.3.197>
- Ouellette RJ, Rawn JD (2015) Synthetic Polymers. In: Principles of Organic Chemistry. Elsevier, pp 397–419
- Palm GJ, Reisky L, Böttcher D, Müller H, Michels EAP, Walczak MC, Berndt L, Weiss MS, Bornscheuer UT, Weber G (2019) Structure of the plastic-degrading *Ideonella sakaiensis* MHETase bound to a substrate. *Nat Commun* 10:1717 . <https://doi.org/10.1038/s41467-019-09326-3>
- Papaleo E, Tiberti M, Invernizzi G, Pasi M, Ranzani V (2012) Molecular Determinants of Enzyme Cold Adaptation: Comparative Structural and Computational Studies of Cold- and Warm-Adapted Enzymes. *Curr Protein Pept Sci* 12:657–683 . <https://doi.org/10.2174/1389203711109070657>
- Park E-J, Han J-S, Park E-J, Seong E, Lee G-H, Kim D-W, Son H-Y, Han H-Y, Lee B-S (2020) Repeated-oral dose toxicity of polyethylene microplastics and the possible implications on reproduction and development of the next generation. *Toxicol Lett* 324:75–85 . <https://doi.org/10.1016/j.toxlet.2020.01.008>
- Park SH, Kim SH (2014) Poly (ethylene terephthalate) recycling for high value added textiles. *Fash Text* 1:1 . <https://doi.org/10.1186/s40691-014-0001-x>
- Paszun D, Spychaj T (1997) Chemical Recycling of Poly(ethylene terephthalate). *Ind Eng Chem Res* 36:1373–1383 . <https://doi.org/10.1021/ie960563c>
- Pawelec KM, White AA, Best SM (2019) Properties and characterization of bone repair materials. In: Bone Repair Biomaterials, Second Edi. Elsevier, pp 65–102
- Peng G, Xu P, Zhu B, Bai M, Li D (2018) Microplastics in freshwater river sediments in Shanghai, China: A case study of risk assessment in mega-cities. *Environ Pollut* 234:448–456 . <https://doi.org/10.1016/j.envpol.2017.11.034>
- Pérez S, Tvaroška I (2014) Carbohydrate-protein interactions: Molecular modeling insights
- Pirillo V, Pollegioni L, Molla G (2021) Analytical methods for the investigation of enzyme-catalyzed degradation of polyethylene terephthalate. *FEBS J* 288:4730–4745 . <https://doi.org/10.1111/febs.15850>
- Pontius J, Richelle J, Wodak SJ (1996) Deviations from standard atomic volumes as a quality measure for protein crystal structures. *J Mol Biol* 264:121–136 . <https://doi.org/10.1006/jmbi.1996.0628>
- Poppe L, Vértessy BG (2018) The Fourth Wave of Biocatalysis Emerges- The 13 th International Symposium on Biocatalysis and Biotransformations. *ChemBioChem* 19:284–287 . <https://doi.org/10.1002/cbic.201700687>
- Qiao Y, Hu R, Chen D, Wang L, Wang Z, Yu H, Fu Y, Li C, Dong Z, Weng Y-X, Du W (2022) Fluorescence-activated

- droplet sorting of PET degrading microorganisms. *J Hazard Mater* 424:127417 .
<https://doi.org/10.1016/j.jhazmat.2021.127417>
- Qin Y (2016) A brief description of textile fibers. In: *Medical Textile Materials*. Elsevier, pp 23–42
- R Core Team (2020) R: A language and environment for statistical computing. Vienna, Austria: R Foundation for Statistical Computing.
- Rahimi A, García JM (2017) Chemical recycling of waste plastics for new materials production. *Nat Rev Chem* 1:0046 .
<https://doi.org/10.1038/s41570-017-0046>
- Ravindranath K, Mashelkar RA (1986) Polyethylene terephthalate—I. Chemistry, thermodynamics and transport properties. *Chem Eng Sci* 41:2197–2214 . [https://doi.org/10.1016/0009-2509\(86\)85070-9](https://doi.org/10.1016/0009-2509(86)85070-9)
- Ribitsch D, Hromic A, Zitzenbacher S, Zartl B, Gamerith C, Pellis A, Jungbauer A, Łyskowski A, Steinkellner G, Gruber K, Tscheliessnig R, Acero EH, Guebitz GM (2017) Small Cause , Large Effect: Structural Characterization of Cutinases From *Thermobifida cellulositica*. 114:2481–2488 .
<https://doi.org/10.1002/bit.26372>
- Roe DR, Cheatham TE (2013) PTRAJ and CPPTRAJ: Software for processing and analysis of molecular dynamics trajectory data. *J Chem Theory Comput* 9:3084–3095 . <https://doi.org/10.1021/ct400341p>
- Ronkvist ÅM, Xie W, Lu W, Gross RA (2009) Cutinase-Catalyzed Hydrolysis of Poly(ethylene terephthalate). *Macromolecules* 42:5128–5138 . <https://doi.org/10.1021/ma9005318>
- Roth C, Wei R, Oeser T, Then J, Föllner C, Zimmermann W, Sträter N (2014) Structural and functional studies on a thermostable polyethylene terephthalate degrading hydrolase from *Thermobifida fusca*. *Appl Microbiol Biotechnol* 98:7815–7823 . <https://doi.org/10.1007/s00253-014-5672-0>
- Roy K, Kar S, Das RN (2015) Other Related Techniques. In: *Understanding the Basics of QSAR for Applications in Pharmaceutical Sciences and Risk Assessment*. Elsevier, pp 357–425
- Ryckaert JP, Ciccotti G, Berendsen HJC (1977) Numerical integration of the cartesian equations of motion of a system with constraints: molecular dynamics of n-alkanes. *J Comput Phys* 23:327–341 . [https://doi.org/10.1016/0021-9991\(77\)90098-5](https://doi.org/10.1016/0021-9991(77)90098-5)
- Santiago M, Ramírez-Sarmiento CA, Zamora RA, Parra LP, RamÃ-rez-Sarmiento C, Zamora RA, Parra LP (2016) Discovery, Molecular Mechanisms and Industrial Applications of Cold-Active Enzymes. *Front Microbiol* 7:1408 . <https://doi.org/10.3389/fmicb.2016.01408>
- Satsangi S (2017) Polyethylene Terephthalate (PET) Market by Application (Beverages, Sheet & Films, Consumer Goods, Food Packaging, and Others) and End-use Industry (Packaging, Electrical & Electronics, Automotive, Construction, and Others) Global Opportunity Analysis And Industry Forecast, 2017–2023. Big Market Research, Portland, OR, USA.

- Scandola M, Focarete ML, Frisoni G (1998) Simple Kinetic Model for the Heterogeneous Enzymatic Hydrolysis of Natural Poly(3-hydroxybutyrate). *Macromolecules* 31:3846–3851 . <https://doi.org/10.1021/ma980137y>
- Schmidt J, Wei R, Oeser T, Belisário-Ferrari MR, Barth M, Then J, Zimmermann W (2016) Effect of Tris, MOPS, and phosphate buffers on the hydrolysis of polyethylene terephthalate films by polyester hydrolases. *FEBS Open Bio* 6:919–927 . <https://doi.org/10.1002/2211-5463.12097>
- Schyns ZOG, Shaver MP (2021) Mechanical Recycling of Packaging Plastics: A Review. *Macromol Rapid Commun* 42:1–27 . <https://doi.org/10.1002/marc.202000415>
- Sheldon RA, Woodley JM (2018) Role of Biocatalysis in Sustainable Chemistry. *Chem Rev* 118:801–838 . <https://doi.org/10.1021/acs.chemrev.7b00203>
- Shen Q, Xiong B, Zheng M, Luo X, Luo C, Liu X, Du Y, Li J, Zhu W, Shen J, Jiang H (2011) Knowledge-based scoring functions in drug design: 2. can the knowledge base be enriched? *J Chem Inf Model* 51:386–397 . <https://doi.org/10.1021/ci100343j>
- Siddiqui KS (2017) Defying the activity–stability trade-off in enzymes: taking advantage of entropy to enhance activity and thermostability. *Crit Rev Biotechnol* 37:309–322 . <https://doi.org/10.3109/07388551.2016.1144045>
- Son HF, Cho II, Joo S, Seo H, Sagong H-Y, Choi SY, Lee SY, Kim K-J (2019) Rational Protein Engineering of Thermo-Stable PETase from *Ideonella sakaiensis* for Highly Efficient PET Degradation. *ACS Catal* 9:3519–3526 . <https://doi.org/10.1021/acscatal.9b00568>
- Song Y, DiMaio F, Wang RY-R, Kim D, Miles C, Brunette T, Thompson J, Baker D (2013) High-Resolution Comparative Modeling with RosettaCM. *Structure* 21:1735–1742 . <https://doi.org/10.1016/j.str.2013.08.005>
- Sonnendecker C, Oeser J, Richter PK, Hille P, Zhao Z, Fischer C, Lippold H, Blázquez-Sánchez P, Engelberger F, Ramírez-Sarmiento CA, Oeser T, Lihanova Y, Frank R, Jahnke H-G, Billig S, Abel B, Sträter N, Matysik J, Zimmermann W (2021) Low Carbon Footprint Recycling of Post-Consumer PET Plastic with a Metagenomic Polyester Hydrolase. *ChemSusChem* 1–11 . <https://doi.org/10.1002/cssc.202101062>
- Sonnendecker C, Oeser J, Richter PK, Hille P, Zhao Z, Fischer C, Lippold H, Blázquez-Sánchez P, Engelberger F, Ramírez-Sarmiento CA, Oeser T, Lihanova Y, Frank R, Jahnke HG, Billig S, Abel B, Sträter N, Matysik J, Zimmermann W (2022) Low Carbon Footprint Recycling of Post-Consumer PET Plastic with a Metagenomic Polyester Hydrolase. *ChemSusChem* 15: . <https://doi.org/10.1002/cssc.202101062>
- Streit-bianchi M, Cimadevila M, Trettnak W, Pollution CP, Science T (2020) *Mare Plasticum - The Plastic Sea*. Springer International Publishing, Cham
- Sulaiman S, Yamato S, Kanaya E, Kim J-J, Koga Y, Takano K, Kanaya S (2012) Isolation of a Novel Cutinase Homolog with Polyethylene Terephthalate-Degrading Activity from Leaf-Branch Compost by Using a Metagenomic Approach. *Appl Environ Microbiol* 78:1556–1562 . <https://doi.org/10.1128/AEM.06725-11>

- Sun J, Cui Y, Wu B (2021) GRAPE, a greedy accumulated strategy for computational protein engineering. In: *Methods in Enzymology*. pp 207–230
- Taniguchi I, Yoshida S, Hiraga K, Miyamoto K, Kimura Y, Oda K (2019) Biodegradation of PET: Current Status and Application Aspects. *ACS Catal* 9:4089–4105 . <https://doi.org/10.1021/acscatal.8b05171>
- Teuten EL, Saquing JM, Knappe DRU, Barlaz MA, Jonsson S, Björn A, Rowland SJ, Thompson RC, Galloway TS, Yamashita R, Ochi D, Watanuki Y, Moore C, Viet PH, Tana TS, Prudente M, Boonyatumanond R, Zakaria MP, Akkhavong K, Ogata Y, Hirai H, Iwasa S, Mizukawa K, Hagino Y, Imamura A, Saha M, Takada H (2009) Transport and release of chemicals from plastics to the environment and to wildlife. *Philos Trans R Soc B Biol Sci* 364:2027–2045 . <https://doi.org/10.1098/rstb.2008.0284>
- Then J, Wei R, Oeser T, Barth M, Belisário-Ferrari MR, Schmidt J, Zimmermann W (2015) Ca²⁺ and Mg²⁺ binding site engineering increases the degradation of polyethylene terephthalate films by polyester hydrolases from *Thermobifida fusca*. *Biotechnol J* 10:592–598 . <https://doi.org/10.1002/biot.201400620>
- Timmins MR, Lenz RW, Clinton Fuller R (1997) Heterogeneous kinetics of the enzymatic degradation of poly(β -hydroxyalkanoates). *Polymer (Guildf)* 38:551–562 . [https://doi.org/10.1016/S0032-3861\(96\)00530-7](https://doi.org/10.1016/S0032-3861(96)00530-7)
- Tokiwa Y, Suzuki T (1977) Hydrolysis of polyesters by lipases. *Nature* 270:76–78 . <https://doi.org/10.1038/270076a0>
- Tournier V, Topham CM, Gilles A, David B, Folgoas C, Moya-Leclair E, Kamionka E, Desrousseaux ML, Texier H, Gavalda S, Cot M, Guémard E, Dalibey M, Nomme J, Cioci G, Barbe S, Chateau M, André I, Duquesne S, Marty A (2020) An engineered PET depolymerase to break down and recycle plastic bottles. *Nature* 580:216–219 . <https://doi.org/10.1038/s41586-020-2149-4>
- Vertommen MAME, Nierstrasz VA, Veer M Van Der, Warmoeskerken MMCG (2005) Enzymatic surface modification of poly(ethylene terephthalate). *J Biotechnol* 120:376–386 . <https://doi.org/10.1016/j.jbiotec.2005.06.015>
- Wallace NE, Adams MC, Chafin AC, Jones DD, Tsui CL, Gruber TD (2020) The highly crystalline PET found in plastic water bottles does not support the growth of the PETase-producing bacterium *Ideonella sakaiensis*. *Environ Microbiol Rep* 12:578–582 . <https://doi.org/10.1111/1758-2229.12878>
- Weeks JJ (1963) Melting temperature and change of lamellar thickness with time for bulk polyethylene. *J Res Natl Bur Stand Sect A Phys Chem* 67A:441 . <https://doi.org/10.6028/jres.067A.046>
- Wei R, Breite D, Song C, Gräsing D, Ploss T, Hille P, Schwerdtfeger R, Matysik J, Schulze A, Zimmermann W (2019a) Biocatalytic Degradation Efficiency of Postconsumer Polyethylene Terephthalate Packaging Determined by Their Polymer Microstructures. *Adv Sci* 6: . <https://doi.org/10.1002/advs.201900491>
- Wei R, Haugwitz G Von, Pfa L, Mican J, Badenhorst PS, Liu W, Weber G, Austin HP, Bednar D, Damborsky J, Bornscheuer UT (2022) Mechanism-Based Design of Efficient PET Hydrolases. *ACS Catal* 12:3382–3396 .

<https://doi.org/10.1021/acscatal.1c05856>

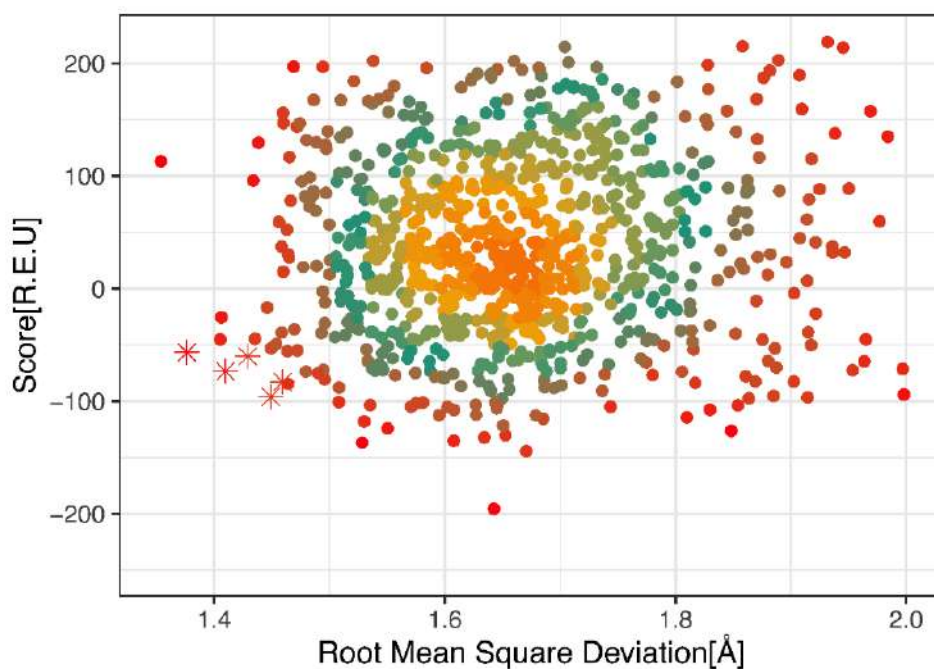
- Wei R, Oeser T, Barth M, Weigl N, Lübs A, Schulz-Siegmund M, Hacker MC, Zimmermann W (2014a) Turbidimetric analysis of the enzymatic hydrolysis of polyethylene terephthalate nanoparticles. *J Mol Catal B Enzym* 103:72–78 . <https://doi.org/10.1016/j.molcatb.2013.08.010>
- Wei R, Oeser T, Billig S, Zimmermann W (2012) A high-throughput assay for enzymatic polyester hydrolysis activity by fluorimetric detection. *Biotechnol J* 7:1517–1521 . <https://doi.org/10.1002/biot.201200119>
- Wei R, Oeser T, Schmidt J, Meier R, Barth M, Then J, Zimmermann W (2016) Engineered bacterial polyester hydrolases efficiently degrade polyethylene terephthalate due to relieved product inhibition. *Biotechnol Bioeng* 113:1658–1665 . <https://doi.org/10.1002/bit.25941>
- Wei R, Oeser T, Then J, Kühn N, Barth M, Schmidt J, Zimmermann W (2014b) Functional characterization and structural modeling of synthetic polyester-degrading hydrolases from *Thermomonospora curvata*. *AMB Express* 4:44 . <https://doi.org/10.1186/s13568-014-0044-9>
- Wei R, Oeser T, Zimmermann W (2014c) Synthetic Polyester-Hydrolyzing Enzymes From Thermophilic Actinomycetes. In: *Advances in Applied Microbiology*. pp 267–305
- Wei R, Song C, Gräsing D, Schneider T, Bielytskyi P, Böttcher D, Matysik J, Bornscheuer UT, Zimmermann W (2019b) Conformational fitting of a flexible oligomeric substrate does not explain the enzymatic PET degradation. *Nat Commun* 10:5581 . <https://doi.org/10.1038/s41467-019-13492-9>
- Wei R, Zimmermann W (2017a) Biocatalysis as a green route for recycling the recalcitrant plastic polyethylene terephthalate. *Microb Biotechnol* 10:1302–1307 . <https://doi.org/10.1111/1751-7915.12714>
- Wei R, Zimmermann W (2017b) Microbial enzymes for the recycling of recalcitrant petroleum-based plastics: how far are we? *Microb Biotechnol* 10:1308–1322 . <https://doi.org/10.1111/1751-7915.12710>
- Yoshida S, Hiraga K, Takehana T, Taniguchi I, Yamaji H, Maeda Y, Toyohara K, Miyamoto K, Kimura Y, Oda K (2016) A bacterium that degrades and assimilates poly(ethylene terephthalate). *Science* (80-) 351:1196–1199 . <https://doi.org/10.1126/science.aad6359>
- Zeng W, Li X, Yang Y, Min J, Huang J, Liu W, Niu D, Yang X, Han X, Zhang L, Dai L, Chen C, Guo R (2022) Substrate-Binding Mode of a Thermophilic PET Hydrolase and Engineering the Enzyme to Enhance the Hydrolytic Efficacy. *ACS Catal* 12:3033–3040 . <https://doi.org/10.1021/acscatal.1c05800>
- Zhang J, Zhang H, Wu T, Wang Q, Van Der Spoel D (2017) Comparison of Implicit and Explicit Solvent Models for the Calculation of Solvation Free Energy in Organic Solvents. *J Chem Theory Comput* 13:1034–1043 . <https://doi.org/10.1021/acs.jctc.7b00169>
- Zhang Z (1998) Protein sequence similarity searches using patterns as seeds. *Nucleic Acids Res* 26:3986–3990 . <https://doi.org/10.1093/nar/26.17.3986>

Zhang Z, Schäffer a a, Miller W, Madden TL, Lipman DJ, Koonin E V, Altschul SF (1998) Protein sequence similarity searches using patterns as seeds. *Nucleic Acids Res* 26:3986–3990 . <https://doi.org/gkb628> [pii]

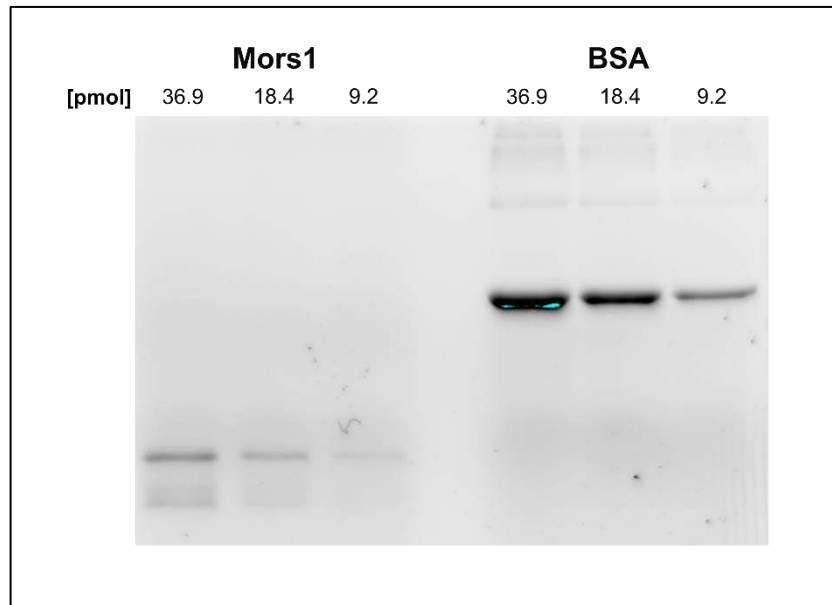
Zhang Z, Smith DL (1993) Determination of amide hydrogen exchange by mass spectrometry: A new tool for protein structure elucidation. *Protein Sci* 2:522–531 . <https://doi.org/10.1002/pro.5560020404>

Zisis T, Freddolino PL, Turunen P, Van Teeseling MCF, Rowan AE, Blank KG (2015) Interfacial Activation of *Candida antarctica* Lipase B: Combined Evidence from Experiment and Simulation. *Biochemistry* 54:5969–5979 . <https://doi.org/10.1021/acs.biochem.5b00586>

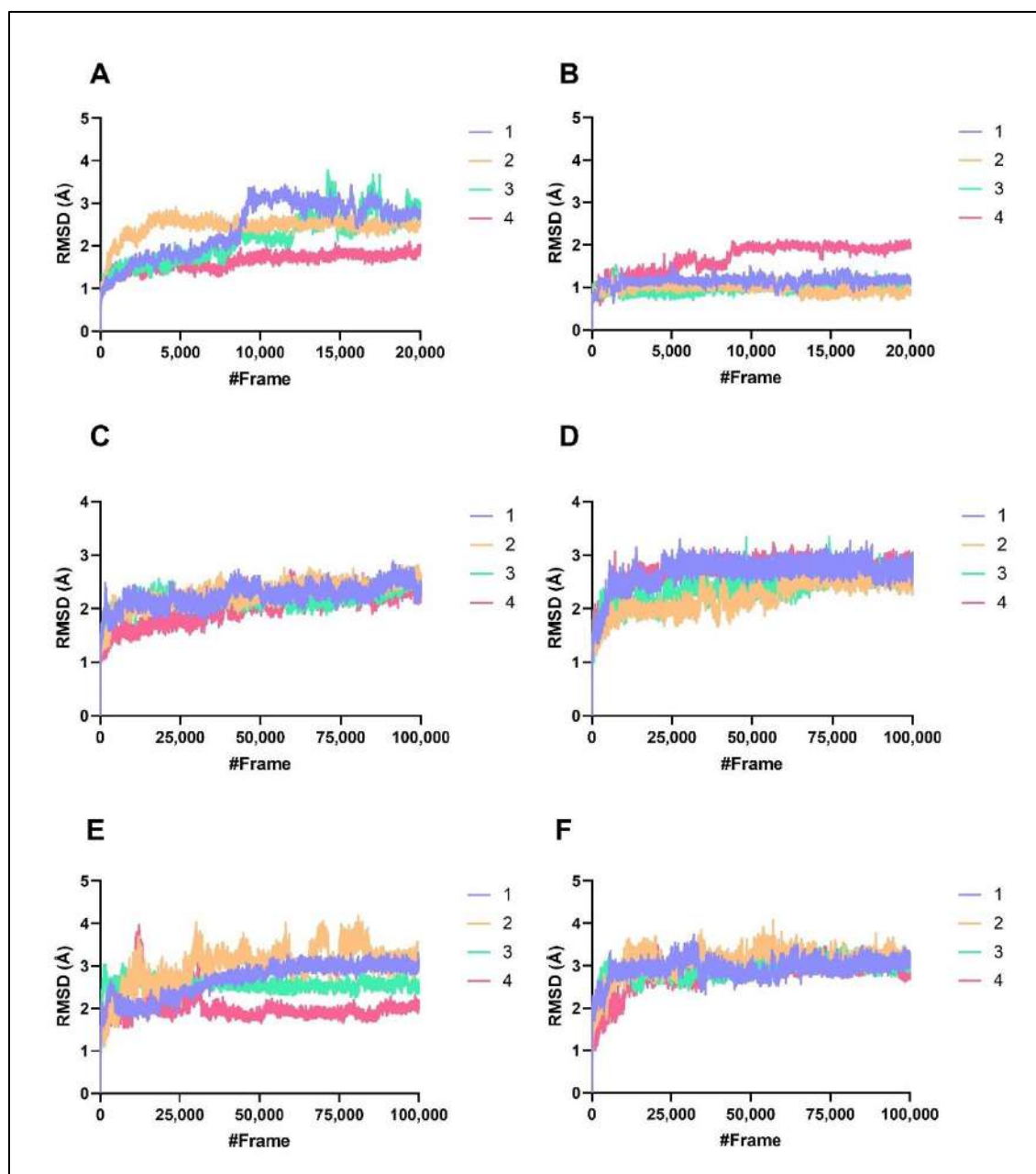
Supplementary figures



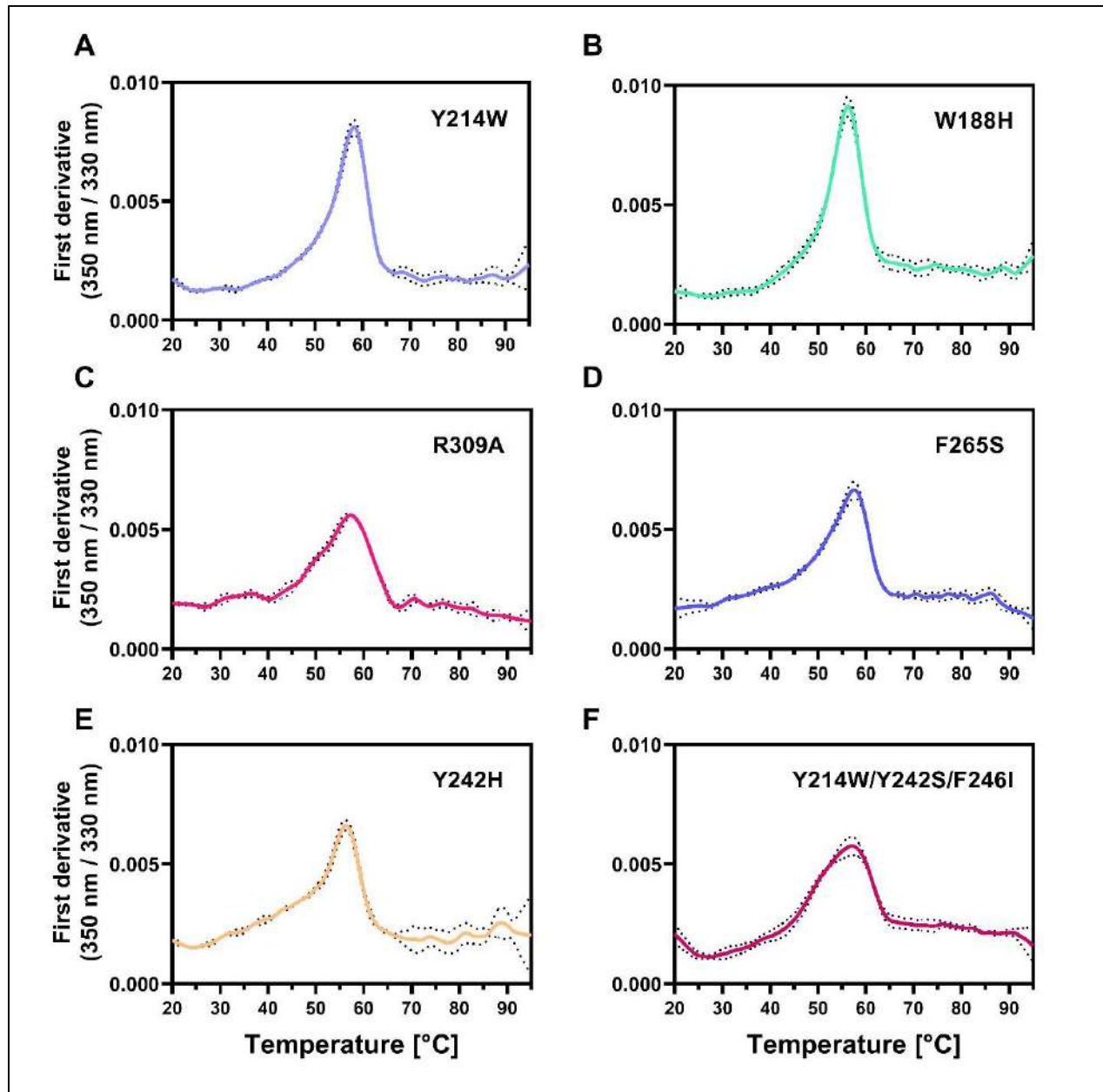
Supplementary Figure 1. Homology models of Mors1 generated using Rosetta3. Every dot represents a model for a total of 1,000 generated models. Five models were selected (red asterisks) based on the lowest score and RMSD against the template structure of *IsPETase* (PDB 6EQE) for further validation.



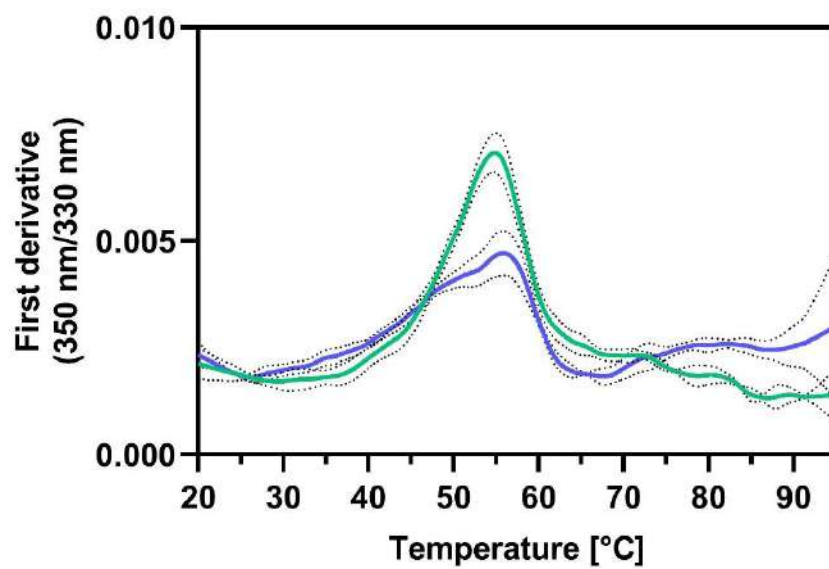
Supplementary Figure 2. SDS-PAGE with fluorescent labelling of free cysteines in Mors1 and BSA. Inverted fluorescence image, where lanes 1-3 correspond to Mors1 and the lanes 4-6 to BSA as a control. Under non-reducing conditions, BSA showed a strong fluorescence corresponding to its free cysteine while Mors1 showed only a weak fluorescence indicating that some cysteines residues in the protein were reduced possibly during protein expression or preparation. However, the fluorescence would be twice as strong as in the BSA sample in the presence of completely reduced cysteine residues which would have resulted in the labeling of two thiol groups with ABD.



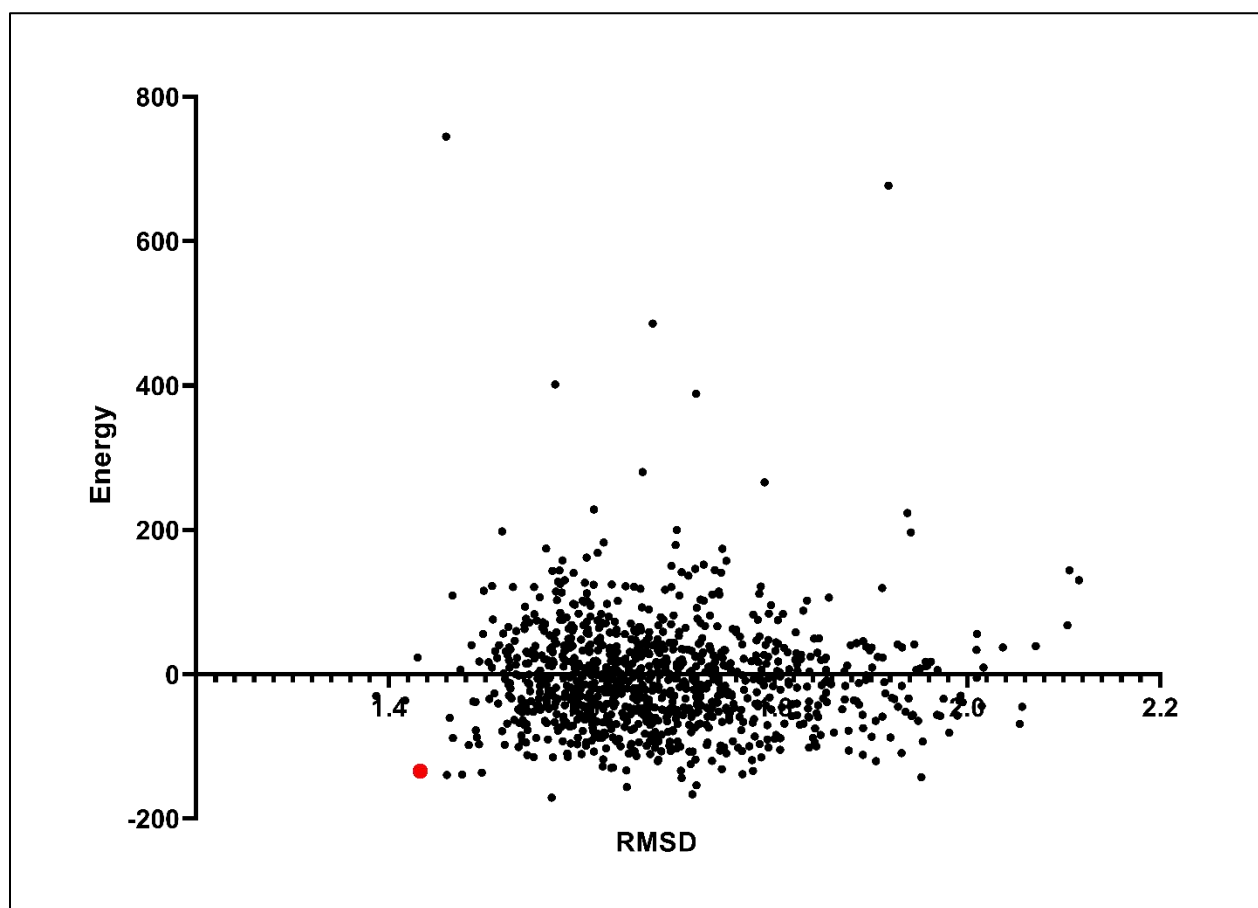
Supplementary Figure 3. RMSD time plots for all MD simulations. $C\alpha$ atom RMSD computed for 20,000 or 100,000 frames during the 0.1 μ s and 1.0 μ s MD simulations respectively. RMSD was computed for the entire protein with respect to the first frame of the MD simulation. Four replicas were performed for each system. **A)** Mors1 at 25 °C for 0.1 μ s. **B)** *Is*PETase at 25 °C for 0.1 μ s. **C)** Mors1 at 25 °C for 1.0 μ s. **D)** Mors1 at 45 °C for 1.0 μ s. **E)** CM^{A266C} at 25 °C for 1.0 μ s. **F)** CM^{A266C} at 45 °C for 1.0 μ s.



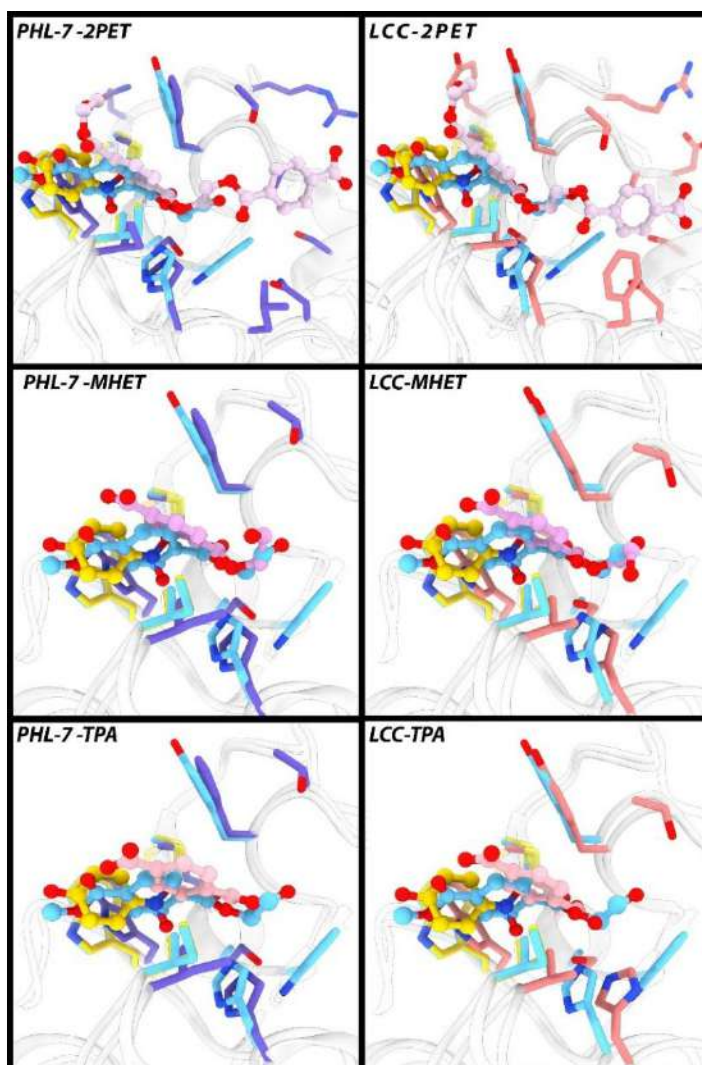
Supplementary Figure 4. First derivative of the ratio of the fluorescence measured at 350 and 330 nm from 20 °C to 90 °C of the variants of Mors1. Experiments were performed in triplicates. Dotted lines represent the standard deviation.



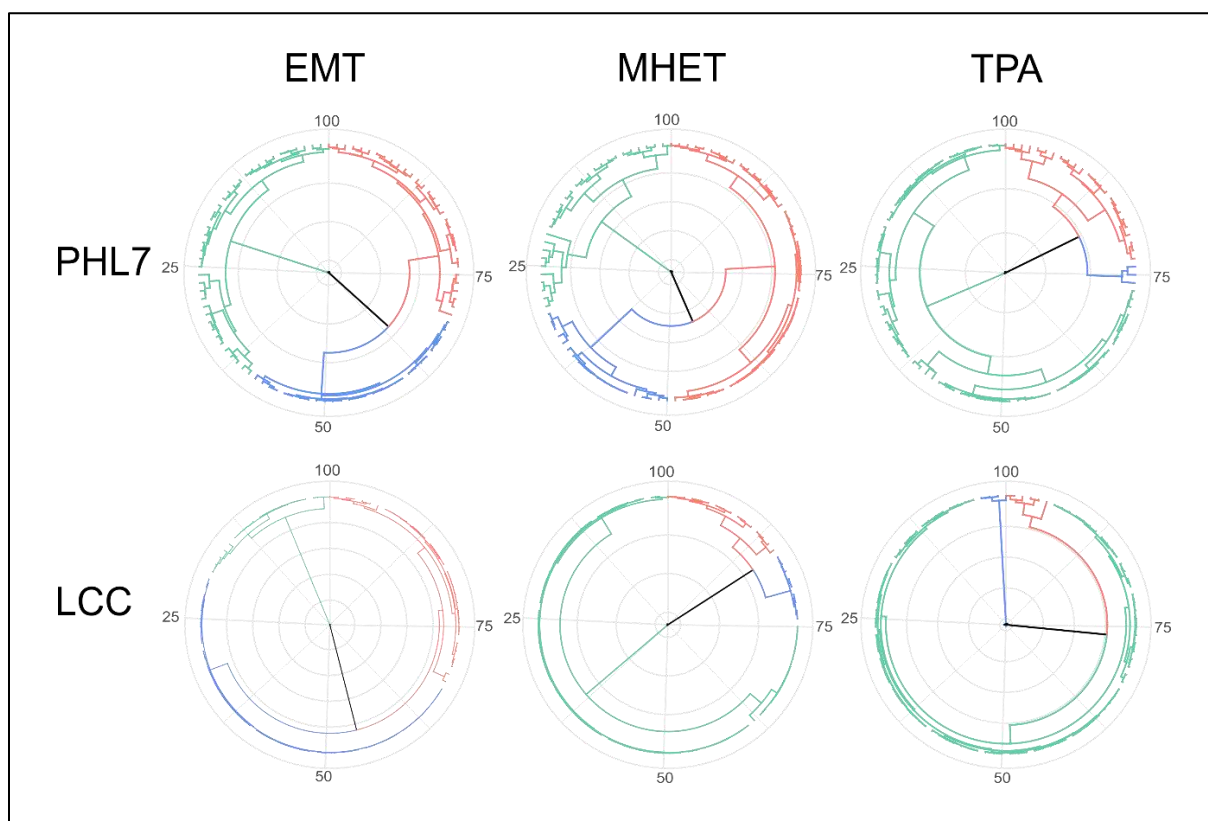
Supplementary Figure 5. First derivative of the ratio of the fluorescence measured at 350 and 330 nm from 20 °C to 90 °C of the variants of Mors1. Green: CM. Blue: CM^{A266C}. Experiments were performed in triplicates. Dotted lines represent the standard deviation.



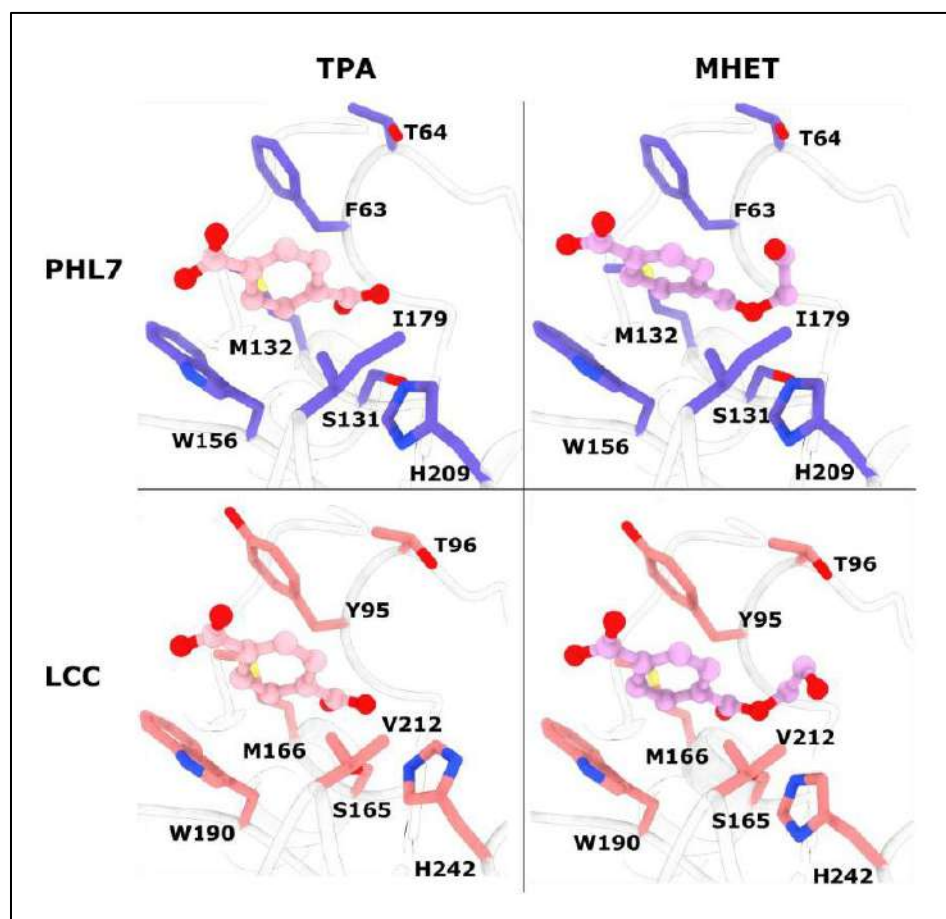
Supplementary Figure 6. Homology models of CM^{A266C} generated using Rosetta3. Every dot represents a model for a total of 1000 models. The red dot shows the model with the lowest energy and RMSD against the template structure of *IsPETase* (PDB 6EQE). This model was selected for further validation.



Supplementary Figure 7. Superimposition of a representative structure of EMT, MHET and TPA clusters with the solved structure of *IsPETase* in complex with HEMT and p-nitrophenol for PHL7 and LCC. The lowest binding energy EMT, MHET and TPA docking poses (balls and sticks, pink) positioned a terephthalic ring in the same groove as seen for p-nitrophenol (balls and sticks, yellow) and HEMT (balls and sticks, cyan) in solved structures of *IsPETase*. Crystal structures of *IsPETase* are represented in sticks in yellow and cyan, PHL7 is represented in sticks in dark blue and LCC is represented in sticks in salmon.



Supplementary Figure 8. Radial dendrogram of the hierarchical clustering distance matrix of the 100 lowest binding energy complexes of LCC and PHL7 and their corresponding ligands (EMT, MHET and TPA). Cluster 1 is marked in green, cluster 2 in red and cluster 3 in blue. Each cluster represents a distinct binding mode. Cluster abundances are indicated in **Supplementary Table 8.**



Supplementary Figure 9. Lowest RMSD pose of the 0.25% best interface binding energy complexes. Top: PHL7 in complex with TPA and MHET. Bottom: LCC in complex with TPA and MHET.

Supplementary tables

Supplementary Table 1. DNA and protein sequences for OaCut, Mors1 and CM in their truncated version and without the signal peptide.

Name	DNA sequence
OaCut	GAATTCACCCGTGGCCCGAACCCGACCCCGAGCAGCCTGGAGGCGAGCACCCGGT CCGTATAGCGTGGCGACCCGTAGCGTGGCGAGCAGCGTTAGCGGCTTTGGTGGC GGTACCCTGCACTATCCGACCAACACCACCCGGTACGATGGGTGCGATTGCGGTG GTTCCGGGTTTCTGCTGCAAGAAAGCAGCATTGATTTTTGGGGCCCGAAACTGG CGAGCCACGGTTTCGTGGTTATCACCATTAGCGCGAACAGCGGTTTTGATCAACC GGCGAGCCGTGCGACCCAACTGGGTCGTGCGCTGGATTACGTGATCAACCAGAG CAACGGCAGCAACAGCCCGATTAGCGGTATGGTTGACACCACCCGTCTGGGCGT GGTTGGTTGGAGCATGGGCGGTGGCGGTGCGCTGCAACTGGCGAGCGGTGATCG TCTGAGCGCGGCGATCCCGATTGCGCCGTGGAACCAGGGCGGTAACCGTTTTGA CCAAATCGAGACCCCGACCCTGGTGATTGCGTGCGAAAACGATGTGGTTGCGAG CGTTAACAGCCACGCGAGCCCGTTCTACAACCGTATCCCGAGCACCACCGACAA GCGTATCTGGAGATTAACGGCGGTAGCCACTTTTGCGCGAACGATGGCGGTAG CATCGGCGGTCTGCTGGGCAAGTACGGTGTGAGCTGGATGAAACGTTTCATTGA CAACGATCTGCGTTATGACGCGTTTCTGTGCGGTCCGGATCATGCGGCGAACCGT AGCGTTAGCGAATAACCGTGACACCTGCAACTATTAA
Mors1	GACTGCATCGCGGATAGCAAAATTACCGCGGTGGCGCTGAGCGACACCCGTGAT AACGGCCCGTTCAGCATCCGTACCAAGCGTATTAGCCGTCAGAGCGCGAAAGGT TTTGGTGGCGGTACCATTCACTACCCGACCAACGCGAGCGGTTGCGGTCTGCTGG GTGCGATTGCGGTGGTTCCGGGTTACGTTAGCTATGAGAACAGCATCAAATGGT GGGGTCCGCGTCTGGCGAGCTGGGGTTTCGTGGTTATCACCATTAACACCAACA GCATTTATGACGATCCGACAGCCGTGCGGCGCAACTGAACGCGGCGCTGGATA ACATGATCGCGGACGATACCGTGGGCAGCATGATTGACCCGAAACGTCTGGGTG CGATTGGTTGGAGCATGGGCGGTGGCGGTGCGCTGAAGCTGGCGACCGAGCGTA GCACCGTTCGTGCGATTATGCCGCTGGCGCCGTACCACGATAAGAGCTATGGTG AAGTGAAAACCCCGACCCTGGTTATCGCGTGCGAGGACGATCGTATTGCGGAAA CCAAGAAATACGCGAACGCGTTTTATAAAAACGCGATCGGCCCGAAGATGAAAG TTGAGGTGAACAACGGTAGCCACTTCTGCCCGAGCTACCGTTTTAACGAAATCCT GCTGAGCAAGCCGGTATTGCGTGGATGCAGCGTTACATCAACAACGACACCCG TTTCGATAAGTTTCTGTGCGCGAACGAAAACACTATAGCAAAAGCCCGCGTATCAG CGCGTACGACTATAAGGATTGCCCGTAA
CM	GACTGCATCGCGGATAGCAAAATTACCGCGGTGGCGCTGAGCGACACCCGTGAT AACGGCCCGTTCAGCATCCGTACCAAGCGTATTAGCCGTCAGAGCGCGAAAGGT TTTGGTGGCGGTACCATTCACTACCCGACCAACGCGAGCGGTTGCGGTCTGCTGG GTGCGATTGCGGTGGTTCCGGGTTACGTTAGCTATGAGAACAGCATCAAATGGT GGGGTCCGCGTCTGGCGAGCTGGGGTTTCGTGGTTATCACCATTAACACCAACA

	GCATTTATGACGATCCGGACAGCCGTGCGGGCGCAACTGAACGCGGGCGCTGGATA ACATGATCGCGGACGATACCGTGGGCAGCATGATTGACCCGAAACGTCTGGGTG CGATTGGTTGGAGCATGGGCGGTGGCGGTGCGCTGAAGCTGGCGACCGAGCGTA GCACCGTTCGTGCGATTATGCCGCTGGCGCCGTACCACGATAAGAGCTATGGTG AAGTGA AAAACCCCGACCCTGGTTATCGCGTGCGAGGACGATCGTATTGCGGAAA CCAAGAAATACGCGAACGCGTTTTATAAAAACGCGATCGGCCCGAAGATGAAAG TTGAGGTGGATAACGCGAGCCATTTTTCGCGCCGAACAGCAACAACATCCTGCTGA GCAAGCCGGGTATTGCGTGGATGCAGCGTTACATCAACAACGACACCCGTTTCG ATAAGTTTCTGTGCGCGAACGAAAACACTATAGCAAAAAGCCCGCGTATCAGCGCGT ACGACTATAAGGATTGCCCGTAA
Name	Protein sequence
OaCut	MNKSILK KLSFGTSVLLVSMNALS WTSP TPNPDPIPDPTPCQDDCEFRGPNPTPSSL EASTGPYSVATR SVASSVSGFGGGTLHYPTNTTGTMGAI AVVPGFLLQESSIDFWGP KLASHGFVVITISANS GFDQPASRATQLGRALDYVINQSNGSNSPISGMVDTRRLGVV GWSMGGGGALQLASGDRLSAAIPIAPWNQGGNRFDQIETPTLVIACENDVVASVNS HASPFYNRIPSTTDKAYLEINGGSHFCANDGGSIGLLGKYGVSWMKRFIDNDLRYD AFLCGPDHAANRSVSEYRDCNY
Mors1	MDCIADSKITAVALS DTRDNGPFSIRT KRISRQSAKGFGGGTHIYPTNASGCGLLGAI AVVPGYVSYENSIKWWGPRLASWGFVVITINTNSIYDDPDSRAAQLNAALDNMIAD DTVGS MIDPKRLGAIGWSMGGGGALKLATERSTVRAIMPLAPYHDKSYGEVKTPTL VIACEDDRIAETKKYANAFYKNAIGPKMKVEVNNGSHFCPSYRFNEILLSKPGIAWM QRYINNDTRFDKFLCANENYSKSPRISAYDYKDCP
CM	DCIADSKITAVALS DTRDNGPFSIRT KRISRQSAKGFGGGTHIYPTNASGCGLLGAI AV VPGYVSYENSIKWWGPRLASWGFVVITINTNSIYDDPDSRAAQLNAALDNMIADDT VGS MIDPKRLGAIGWSMGGGGALKLATERSTVRAIMPLAPYHDKSYGEVKTPTLVI ACEDDRIAETKKYANAFYKNAIGPKMKVEVDNASHFAPNSNALLSKPGIAWMQR YINNDTRFDKFLCANENYSKSPRISAYDYKDCP

Supplementary Table 2. DNA sequence of primers used. R: reverse primer. F: forward primer.**CM_A266C**

5'-tgttcgggcaaaaatggctcgcgttatcc-3' R

5'-ccattttgcccgaacagcaacaacatcc-3' F

Mors1_Y242S/F246I

5'-ttataaatcgcgttcgcgcttttcttggttccgcaatacg-3' R

5'-aaaagcgcgaacgcgattataaaaacgcgatcggc-3' F

Mors1_Y214W

5'-tatcgtgccacggcgccagcg-3' R

5'-gcgccgtggcacgataagagctatggtgaag-3' F

Mors1_R309A

5'-gctgatagccgggcttttgctatagttttcg-3' R

5'-aagccccgctatcagcgcgtacgactataag-3' F

Mors1_I236F

5'-tccgaaaacgatcgtcctcgcac-3' R

5'-acgatcgtttgcgaaaccaagaatacg-3' F

Mors1_W188H

5'-ccatgctgaaaccaatcgacccaga-3' R

5'-gattggttcagcatggcggtgg-3' F

Mors1_F265S

5'-gcagctgtggctaccgtttcac-3' R

5'-ccacagctgcccagctaccg-3' F

Mors1_Y242S

5'-gcgcttttcttggttccgcaatacg-3' R

5'-caagaaaagcgcgaacgcgtttataaaaa-3

F

Mors1_Y242H

5'-gcgtgttcttggttccgcaatacg-3'

R

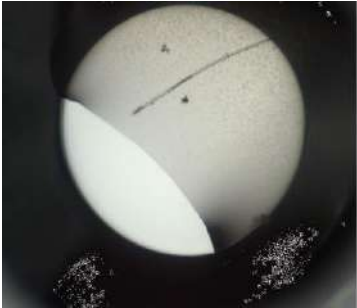
5'-caagaaacacgcgaacgcgtttataa-3'

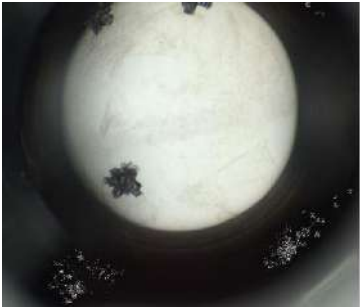
F

Supplementary Table 3. PCR steps for mutagenesis.

Step	Temperature (°C)	Time	Cycles
Initial denaturation	98	30 s	1
Denaturation	98	5 s	
Annealing	63	15 s	22
Elongation	72	5 min	
Final elongation	72	2 min	1

Supplementary Table 4. Crystals obtained under different conditions (buffer, salt, and polymers) for OaCut and its variants.

Protein	Condition	Crystal image
OaCut	0.6 M Trisodium citrate 0.1 M MES pH 6.5	
OaCut	0.01 M ZnCl ₂ 20% (w/v) PEG 6000 0.1 M MES pH 6.0	
OaCut	0.01 M ZnCl ₂ 0.1 M HEPES pH 7.0 20% (w/v) PEG 6000	

OaCut	0.2 CdCl ₂ 40% v/v MPD	
OaCut	0.01 M MgCl ₂ 0.5 NaCl 0.01 mM CTAB	
OaCut	0.1 M MES pH 6.5 0.01 M ZnSO ₄ 22.85 % (v/v) PEG MME 50	
OaCut	0.01 M MgCl ₂ 0.5 M NaCl 0.01 mM CTAB	

OaCut S148A NSP	0.2 MgCl ₂ 3.4 % (v/v) 16 Hexanediol 0.1 M TRIS pH 8.5	
OaCut S148A NSP	0.1 M MES pH 6.5 0.01 M ZnSO ₄ 22.85% (v/v) PEG MME 550	
OaCut S148A NSP	3 M NaCl 0.1 M TRIS pH 8.5	
OaCut S148A NSP	40% (v/v) MPD 0.2 M NH ₄ H ₂ PO ₄	

OaCut S148A	0.2 MgCl ₂ 3.4 % (v/v) 1,6-Hexanediol 0.1 M TRIS pH 8.5	
OaCut S148A	0.3 M MgCl ₂ 25% (w/v) PEG 3350 0.1 M TRIS pH 8.5	
OaCut S148A	40% (v/v) MPD 0.1 M MES pH 6.0	

Supplementary Table 5. Rosetta energy of the 10 selected models of Chimeric Mors1 (CM^{A266C}) after relaxation.

Model number	Energy (REU)
4549	-878.471
4668	-878.412
4593	-878.037
201	-877.087
2228	-876.142
1607	-875.911
1227	-875.731
4590	-875.675
2253	-875.425
424	-875.214

Supplementary Table 6. Structural evaluation of Mors1 models in comparison to the crystal structure of *IsPETase* (PDB 6EQE, chain A).

Model	PROCHECK: Ramachandran plot				Verify3D (%) (score ≥ 0.2)	PROVE
	Core %	Allow %	Generally Allowed (%)	Disallowed (%)		
<i>IsPETase</i>	91.4	7.2	1.4	0.0	98.2%	2.7%
952	85.3	12.4	1.3	0.9	96.18%	3.6%
119	87.1	10.2	0.9	1.8	99.24%	5.0%
650	87.1	11.6	0.0	1.3	100.00%	5.0%
620	84.9	12.4	1.8	0.9	90.46%	4.2%
803	88.0	10.2	0.9	0.9	87.79%	5.0%

Supplementary Table 7. S-H: Distance between γ hydrogen of S160 and ϵ nitrogen of H237. D-H: Distance between δ oxygen of D206 and δ hydrogen of H237.

	Mors1				CM ^{A266C}			
	25 °C		45 °C		25 °C		45 °C	
	S-H	D-H	S-H	D-H	S-H	D-H	S-H	D-H
1	6.1 ± 1.5	4.7 ± 1.4	14.3 ± 2.2	8.0 ± 1.9	10.5 ± 6.6	4.5 ± 2.9	13.3 ± 2.9	11.6 ± 2.9
2	4.1 ± 0.9	3.2 ± 1.0	6.3 ± 2.8	7.7 ± 3.5	4.1 ± 0.8	2.8 ± 0.4	15.2 ± 4.0	8.5 ± 3.3
3	5.6 ± 2	4.3 ± 2.6	4.5 ± 1.5	2.4 ± 0.9	5.3 ± 1	2.6 ± 0.4	4.8 ± 1.8	3.2 ± 1.2
4	3.5 ± 0.8	1.9 ± 0.2	5.2 ± 1	2.9 ± 1.1	3.7 ± 0.7	1.9 ± 0.1	6.0 ± 1.9	3.2 ± 1.3

Supplementary Table 8. Sequences homologous to Mors1 identified in Low and High Chla Antarctic marine metagenomes.

Name	Length	Metagenome	Read recruitment	
			Low Chla	High Chla
mtgnm1	178	High Chla	15	7
mtgnm2	255	High Chla	7	15
mtgnm3	180	High Chla	0	4
mtgnm4	311	Low Chla	53	25
mtgnm5	264	Low Chla	39	2
mtgnm6	295	Low Chla	14	18

Supplementary Table 9. Best-hit BLASTP of the candidate enzymes identified in Chile Bay metagenomes.

Best hit BLASTP (refseq_prot database)

Name	Accession ID	e-value	Per. Ident	Query cover	Genus	Family
mtgnm1	WP_025650659.1	5e-118	96.07%	98%	<i>Psychrobacter</i>	Moraxellaceae
mtgnm2	WP_010201091.1	0.0	98.03%	100%	<i>Psychrobacter</i>	Moraxellaceae
mtgnm3	WP_025650659.1	8e-95	82.18%	96%	<i>Psychrobacter</i>	Moraxellaceae
mtgnm4	WP_025650659.1	0.0	97.42%	98%	<i>Psychrobacter</i>	Moraxellaceae
mtgnm5	WP_087815883.1	0.0	96.09%	96%	<i>Psychrobacter</i>	Moraxellaceae
mtgnm6	WP_010201091.1	0.0	96.64%	100%	<i>Psychrobacter</i>	Moraxellaceae

Supplementary Table 10. Number of enzyme-ligand complexes in each cluster obtained from a hierarchical clustering distance matrix. Each cluster represents a distinct binding mode.

	Cluster		
	1	2	3
Enzyme-ligand complex name			
PHL7-EMT	31	29	40
PHL7-MHET	50	30	20
PHL7-TPA	73	24	3
LCC-EMT	33	19	48
LCC-MHET	75	16	9
LCC-TPA	90	6	4

